An Investigation of Phase Change Material (PCM)-Based Ocean Thermal Energy Harvesting

Guangyao Wang

Dissertation submitted to the Faculty of the

Virginia Polytechnic Institute and State University

in partial fulfillment of the requirements for the degree of

Doctor of Philosophy

in

Aerospace Engineering

Kevin G. Wang, Chair

Christine M. Gilbert

Michael K. Philen

Dong S. Ha

Yi Chao

May 3, 2019

Blacksburg, Virginia

Keywords: Renewable Energy, Energy Harvesting, Phase Change Materials,

Thermodynamics, Model Validation

An Investigation of Phase Change Material (PCM)-Based Ocean Thermal Energy Harvesting

Guangyao Wang

ABSTRACT

Phase change material (PCM)-based ocean thermal energy harvesting is a relatively new method, which extracts the thermal energy from the temperature gradient in the ocean thermocline. Its basic idea is to utilize the temperature variation along the ocean water depth to cyclically freeze and melt a specific kind of PCM. The volume expansion, which happens in the melting process, is used to do useful work (e.g., drive a turbine generator), thereby converting a fraction of the absorbed thermal energy into mechanical energy or electrical energy. Compared to other ocean energy technologies (e.g., wave energy converters, tidal current turbines, and ocean thermal energy conversion), the proposed PCM-based approach can be easily implemented at a small scale with a relatively simple structural system, which makes it a promising method to extend the range and service life of battery-powered devices, e.g, autonomous underwater vehicles (AUVs). This dissertation presents a combined theoretical and experimental study of the PCM-based ocean thermal energy harvesting approach, which aims at demonstrating the feasibility of the proposed approach and

investigating possible methods to improve the overall performance of prototypical systems. First, a solid/liquid phase change thermodynamic model is developed, based on which a specific upperbound of the thermal efficiency is derived for the PCM-based approach. Next, a prototypical PCM-based ocean thermal energy harvesting system is designed, fabricated, and tested. To predict the performance of specific systems, a thermo-mechanical model, which couples the thermodynamic behaviors of the fluid materials and the elastic behavior of the structural system, is developed and validated based on the comparison with the experimental measurement. For the purpose of design optimization, the validated thermo-mechanical model is employed to conduct a parametric study. Based on the results of the parametric study, a new scalable and portable PCM-based ocean thermal energy harvesting system is developed and tested. In addition, the thermo-mechanical model is modified to account for the design changes. However, a combined analysis of the results from both the prototypical system and the model reveals that achieving a good performance requires maintaining a high internal pressure, which will complicate the structural design. To mitigate this issue, the idea of using a hydraulic accumulator to regulate the internal pressure is proposed, and experimentally and theoretically examined. Finally, a spatial-varying Robin transmission condition for fluid-structure coupled problems with strong added-mass effect is proposed and investigated using fluid structure interaction (FSI) model problems. This can be a potential method for the future research on the fluid-structure coupled numerical analysis of AUVs, which are integrated with and powered by the PCM-based thermal energy harvesting devices.

An Investigation of Phase Change Material (PCM)-Based Ocean Thermal Energy Harvesting

Guangyao Wang

GENERAL AUDIENCE ABSTRACT

The global ocean, which covers about 71% of the Earth's surface, absorbs a great amount of heat from the sunshine everyday, making it a reliable and renewable source of thermal energy. Also, the temperature of the ocean water varies with depth, which provides a necessary condition (i.e, a temperature gradient) to extract the thermal energy. If harvested and converted into electrical energy using small scale portable devices, the ocean thermal energy can be a potential energy resource to provide power for autonomous underwater vehicles (AUVs), which are conventionally powered by on-board rechargeable batteries. To this end, this dissertation presents a study of using solid/liquid phase change materials (PCMs) to extract thermal energy from the temperature gradient in the ocean. The basic idea is to use the warm surface water and deep cold water to melt and freeze the PCM cyclically. In the meantime, the volume of PCM will expand and contract accordingly. Therefore, a turbine generator can be driven by the volume expansion in the melting process, thereby converting a fraction of the absorbed thermal energy into electrical energy. This study includes four

key aspects. First, to evaluate the theoretical full potential of the PCM-based approach, a solid/liquid phase change thermodynamic model – which represents an idealized energy harvester – is developed. Based on the thermodynamic model, an upperbound of the thermal efficiency is derived. Secondly, two prototypical systems, as well as a thermo-mechanical model which can predict the performance of specific designs, are developed. Third, for the purposes of performance improvement and pressure regulation, the latter of which is associated with the structural safety, a hydraulic accumulator is added to the existing system and its effects are examined using both experimental and theoretical methods. Finally, a computational method is proposed and demonstrated, which can be a potential tool for the design of PCM-based ocean thermal energy harvesting systems when they are integrated with exiting AUVs.

Acknowledgments

I would like to thank my advisor, Dr. Kevin Wang, for the patient guidance, encouragement and advice he has provided throughout my time as his student. I have been extremely lucky to have a advisor who cared so much about my work, and who responded to my questions and queries so promptly.

I wish to express my warm and sincere thanks to all other members of my dissertation committee, Dr. Christine Gilbert, Dr. Michael Philen. Dr. Dong Ha and Dr. Yi Chao, for giving my professional and helpful suggestions, and reviewing this dissertation.

I would like to express thanks to my labmates and friends, Dr. Xingsheng Sun, Mr. Shunxiang Cao, Mr. Ning Liu, Mr. Zhaokuan Lu, Mr. Nan Si, Mr. Zhongshu Ren, Mr Yuchen Zhou, Ms. Shanlin Xu, Ms. Jiahui Li, Ms. Gen Liu, Ms. Yuting Feng, Mr Yang Zeng, Mr. Hongyu Wang and Mr. Weicheng Xue. Thanks for your help and encouragement, especially when I was facing difficulties in the research and daily life. It is also an unforgettable and unique memory to discuss research work with you both in the office and while barbecuing at Claytor Lake State Park.

Finally, but by no means least, thanks go to my parents, wife, daughter and sister for their almost unbelievable support. They are the most important people in my world and I dedicate this dissertation to them.

Contents

List of Figures

List of Tables

Chapter 1

Introduction

Energy has been playing a crucial role in the development of modern society, promoting the scientific and economic progress all over the world. Without energy, the functioning of the whole society would be paralyzed [1]. Today most of the energy that the world consumes comes from fossil fuels, e.g., crude oil, coal and, natural gas [2]. It takes several hundred millions of years for the fossil fuels to form from carcasses of dead plants and animals, and hence scientists consider them nonrenewable. At the same time, the supply and use of energy coming from the fossil fuels have caused various issues – including global warming, environmental concerns, and energy security – which have threatened the long-term sustainability of the whole society. A lot of evidence has suggested that the future will be negatively impacted if humans take no actions to resolve these issues [3].

As one solution to the critical issues people are facing, the development of renewable energy

resources and technologies has been a key research area in the past a few decades. Renewable energy resources are usually abundant and widely available in the natural environment, e.g, solar energy, wind energy, and geothermal energy. Furthermore, the cost of renewable energy resources is much less than that of the conventional fossil fuels, given the free power source and lower cost of the installation and operation of related devices [4]. However, the renewable energy resources also have environmental impacts, although most of them are less significant than those caused by fossil fuels [5]. For example, wind turbines may result in unnatural deaths of birds and bats, and the solar cell manufacturing process includes a number of hazardous materials [6]. Therefore, it is necessary to take actions to effectively minimize or avoid the potential impacts, as the renewable energy resources are becoming a larger portion of the power supply.

The global ocean, which covers about 71% of the Earth's surface, holds a tremendous amount of energy, including mechanical energy and thermal energy [7]. Also, almost all of the ocean energy resources (e.g., wave energy, tidal energy, and thermal energy) are renewable and have the potential of providing a greater amount of energy than the global annual demand [8, 9]. However, the utilization of ocean energy resources is still very limited, mainly because of the economic, technical, and environmental problems that scientists are facing and trying to solve [10].

This dissertation focuses on the combined theoretical and experimental study of harvesting ocean thermal energy using solid/liquid phase change materials (PCMs), to demonstrate the feasibility of the proposed approach and investigate possible methods to improve the

performance of specific prototypical PCM-based thermal energy harvesters. A distinguishing feature of this study is that, it not only aims at the exploitation of renewable energy, but also provides a novel method to extend the service life and range of devices which are usually limited by their conventional fuel resource. The remainder of this chapter is organized as follows. The wide application of autonomous underwater vehicles (AUVs) and the limitation imposed by the power resource, both of which motivate the work in this dissertation, are discussed in Section 1.1. Literature reviews on the existing ocean energy technologies and the PCM-based ocean thermal energy harvesting approach are presented in Sections 1.2 and 1.3, respectively. Finally, the contributions and outline of this dissertation are presented in Section 1.4.

1.1 Motivation

The interior ocean has been mainly explored with devices carried by research ships or attached to mooring platforms [11]. Most of these devices require an interaction with a human operator while carrying out a mission, which imposes a significant limitation on the operability in regions with extreme natural conditions [12]. For example, operations under Arctic and Antarctic ice are either difficult or impossible for the conventional ocean exploration devices [13]. Beside, the high cost involved in the building and operation of a research ship or mooring platform is another factor impeding the development and wide application of these human-controlled devices.

As an emerging technology for the ocean exploration, an autonomous underwater vehicle (AUV) is a marine robot, that travels underwater and fulfills a wide range of tasks without requiring input from an operator [14]. AUVs are usually computer-controlled, self-guiding and self-powered. More importantly, AUVs are more cost-effective, compared with research ships and mooring platforms. Sensors and custom payload modules can be easily integrated with an AUV, which makes it suitable for tasks where autonomy, cost and ease of deployment matter [15]. In recent years, AUVs have been commonly used in commercial, military, and scientific areas, e.g, temperature and salinity measurement, submarine cable inspection, and detecting and mapping rocks and wrecks that are hazardous to navigation for vessels.

However, despite appealing features and growing popularity of AUVs, one significant and nonnegligible limitation still exists. An AUV has to carry an on-board fuel source, which is a lithium-ion battery in most cases, in order to operate underwater without any tether. It is notable that the capacity of the fuel source is key factor impacting the mission effectiveness of an AUV. Currently, the ranges of most AUVs are limited to 200 km or 24 hours, depending on the capacity of the fuel source and load demands [16]. For example, the REMUS 100 AUV, which carries a 1 kWh rechargeable lithium-ion battery and weighs 36 kg in the full load condition, can only continuously operate up to 12 hours at 1.5 m/s [17]. Therefore, most existing AUVs require a regular intervention to charge or replace batteries. Surface vessels have been commonly used to deploy and retrieve AUVs for the purpose of replenishing its energy source. However, the process are often time-consuming, risky and highly impacted by the environmental conditions. Consequently, it is desirable to reduce

the deployment/retrieval frequency or even charge batteries without recovering AUVs to the host platforms.

Researchers have proposed the concept of offshore AUV docking and recharge systems to overcome the limitation imposed by the fuel source. The most commonly used strategy is to build a floating or moored docking system, which can navigate, capture, charge and deploy AUVs automatically [18, 19, 20, 21, 22, 23]. With the proposed systems, AUVs can be recharged without being retrieved to the surface vessels and deployed again, which can greatly reduce the efforts to replenish the energy source. Also, it is notable that, the AUV docking and recharge systems can be powered by ocean energy resources if it is integrated with existing ocean energy harvesting devices, e.g., wave energy converters (WECs). For example, Frye *et al.* designd the Autonomous Ocean Sampling Network (AOSN) docking system, specifically for the MIT Odyssey II AUV [21]. The system is featured with functions of inductive charging and data transfer. However, as shown in Figure 1.1, the functioning of AOSN docking system replies heavily on the mooring and latching systems, which makes the costs of installation and maintenance quite high. Also, the proposed AUV docking and charging systems may have potential negative impacts on the local marine environment and ecosystem. For example, a lot of habitats and species in the Marlborough regions have been impacted by the physical disturbance from the mooring systems [24]. Therefore, it is meaningful to investigate possible methods to provide power to AUVs with ocean energy resources, which require simpler structural systems and have minimal impacts on the marine environment and ecosystem.

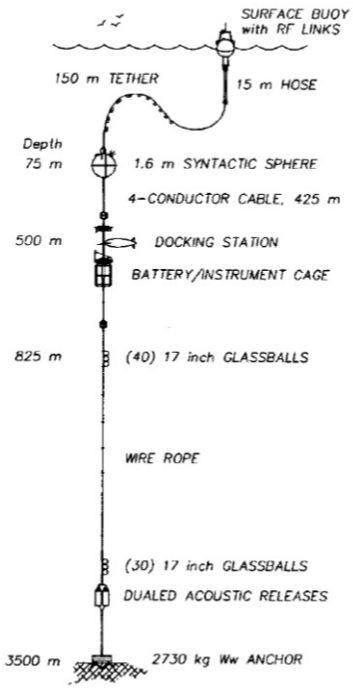

Figure 1.1: AOSN Docking System [21]

1.2 Ocean Energy Resources and Technologies

1.2.1 Ocean Wave Energy

Ocean wave energy, which comes from the energy transfer from the wind passing over the sea surface, represents an enormous and reliable source of energy [25]. The total wave power on the ocean-facing coastlines of the world is estimated to be 2.11 ± 0.05 TW [8]. Also, it's energy density ($2 - 3$ kW/m^2) is greater than that of other renewable energy resources, e.g., wind energy ($0.4 - 0.6$ kW/m^2) and solar energy ($0.1 - 0.2$ kW/m^2) [26].

In the past a few decades, various wave energy converters (WECs) have been proposed, developed and tested. According to the working principles, WECs can be primarily classified

into the following three types:

- Floating structures. The main component of this type of WECs is a floating body, which oscillates under the force of waves. Energy is converted through the relative motion, which can be vertical, horizontal or pitch, between the floating body and an external fixed reference body.

- Overtopping devices. Overtopping devices use the wave velocity to increase the water head in a reservoir and then release it to drive a turbine. Most of the overtopping devices require a long structure to force the sea water into the reservoir.

- Pressure differential. This type of WECs extracts energy from the pressure differential between the wave crests and troughs. The pressure differential is used to compress or push air, and the resulting air flow drives a turbine to produce electricity.

It is notable that these types of WECs mentioned above are usually at a large scale and appropriate for base-load power supply. Recently, researcher have also proposed and developed technologies for small-scale WECs, which can be easily integrated with AUVs and convert the wave energy into electricity [27].

- Piezo-ceramic device. The main component is a newly-developed ruggedized laminated piezo (RLP) chip, which can covert the wave motion to electrical energy. More importantly, RLP is featured with a simple mechanical design and small dimensions.

- Rotary magnetic generator. It is designed basing on a traditional rotary geometry micro-generator with an innovative mechanism, which is able to utilize the low frequency waves to drive the generator continuously.

- Linear magnetic generator. It is a novel magnet/coil device, which extracts energy from the oscillatory motion of waves and has been used to a power a sonobuoy (AN/SSQ-101) [27].

Although it has been shown that wave energy can be a potential energy resource for AUVs, the power output from WECs are quite irregular and unsteady, which is sensitive to the local wave conditions. Therefore, there is a possibility that WECs cannot provide enough power for AUVs when operating in regions with relatively weak wave motions.

1.2.2 Tidal Energy

Tidal energy is the energy dissipated by the periodic tidal movements, in response to the gravitational and centrifugal forces between the earth, moon and sun [28]. The global tidal energy capacity is estimated to be greater than 120 GW [9]. Compared with other renewable energy resources, the forecasting of tides is easier and more accurate in terms of time and magnitude [29]. Tidal energy consists of two main components, potential energy and kinetic energy. Correspondingly, there are two primary methods to extract energy from tides.

- Tidal barrages. The basic mechanism is to build a dam-like structure across a bay or estuary, which allows water to flow into a tidal basin during high tide [30]. As a result,

the water potential energy will accumulate within the tidal basin and can be released to drive turbines built in the barrage to produce electricity during low tide.

- Tidal current turbines. This type of devices captures the kinetic energy in moving water to generate electricity, which is similar to wind energy technologies [31]. Besides, tidal current turbines are featured with the capacity of generating power during both flood and ebb tides. Currently, there are two primary categorizations of tidal current turbines, horizontal axis and vertical axis tidal current tidal turbines, both of which need to be fixed or moored.

Similar to wave energy, most of the existing tidal energy harvesting technologies are at a large scale, the structure of which are quite complex [32]. Despite this, tidal energy could still be a potential energy resource for AUVs, if tidal current turbines in smaller scales can be manufactured and integrated with AUVs. A crucial challenge is that the tidal current turbines integrated with AUVs should be able to operate under different current flow directions, because the relative current flow direction with respect to the turbines keeps changing as AUVs travels underwater.

1.2.3 Ocean Thermal Energy

It is well known that a great amount of heat from sunshine is deposited and accumulated in ocean water almost everyday. The temperature of ocean water varies a lot in different depths [25], basing on which the ocean thermal energy is generated. In tropical or semi-

tropical areas, the temperature difference between the shallow region ($0 - 50$ m) and deep region ($500 - 100$ m) remains about 20 °C [33, 34]. The original source of ocean thermal energy is solar energy, but it is more reliable and stable due to its weak dependence on seasons and day-night cycles.

One approach to harvest ocean thermal energy is ocean thermal energy conversion (OTEC), which utilizes temperature difference along the ocean depth to run a Rankin-cycle-based heat engine [35, 36]. The key technical point is to use the shallow warm water to vaporize a working fluid, which is used to spin the a turbine to produce electricity. Then the deep cold water is pumped to condense the vapor and the working fluid is cycled. In the past a few decades, OTEC has been applied to build power plants in a few places, which contribute to the local base-load power supply [37]. The world's largest OTEC plant with power of 100 kW was built in Hawaii in 2015 [38]. However, as shown in Figure 1.2, the operation of a OTEC plant replies heavily on the complex structural system, e.g., the floating platform and piping system. Hence, it is quite challenging to implement OTEC at a small scale and integrate it with existing AUVs.

Another possible approach to extract energy from the temperature gradient is thermo-electric generators (TEGs), which can directly convert heat flux into electrical energy [39]. However, TEGs usually need a greater temperature gradient (> 50°C) to produce reasonable electric power [40]. For example, TEGs have been used to supply power to subsea control electronics for oil wellheads [41]. However, in order to achieve enough power output, the energy source in this application comes from the temperature between the sea floor water and oil wellheads($\approx$

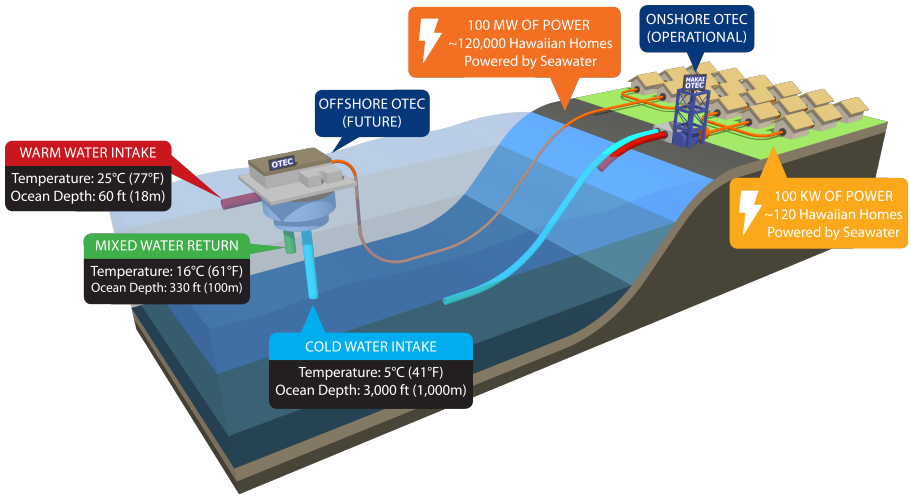

Figure 1.2: Diagram of the OTEC plant with power of 100 kW [38]

50°C), instead of that induced by the depth variation.

1.2.4 Summary

As mentioned in Section 1.1, the limited capacity of the on-board energy sources (e.g., batteries) and existing recharging strategies are imposing a significant limitation on the mission efficiency of AUVs. Although the aforementioned existing ocean energy technologies have the potential to provide power for AUVs, almost none of them can meet the requirements of scalability, minimal negative impacts, and steady energy output at the same time. Therefore, a new ocean energy technology needs to be developed in order to meet the power requirements of AUVs, which can help further promote their application in various fields.

1.3 Phase change material (PCM)-based Ocean Thermal Energy Harvesting

PCMs are substances which absorb and release large amounts of energy (i.e., latent heat), while keeping a nearly constant temperature, during the melting and freezing processes. Because of this salient feature, PCMs have been widely used in latent heat thermal energy storage systems for solar engineering, building thermal management, and transpiration of temperature-sensitive products [42]. PCM-based ocean thermal energy harvesting is a relatively new method, which has demonstrated potential to extract energy from the temperature gradient existing in the ocean thermocline. The basic idea is to select a specific PCM with melting temperature within the range of the temperature variation of the ocean theromocline. As the PCM moves vertically in the ocean, the ambient temperature keeps varying and the PCM undergoes solid/liquid phase changes cyclically, which is accompanied with volume changes. Specifically, the volume of PCM expands and contracts in the melting and freezing processes, respectively. The volume expansion in the melting process can utilized to do work (e.g., spinning a turbine generator), thereby converting a fraction of the absorbed thermal energy into mechanical energy or electrical energy.

The general concept of PCM-based ocean thermal energy harvesting was first proposed and patented by Jones *et al.* [43, 44]. Following the concept, Chao developed a compact PCM-based ocean thermal energy harvesting and storage system, which was integrated with an existing float, i.e., Sounding Oceanographic Lagrangian Observer (SOLO) [11]. The

system was programmed to dive between the surface (20°C) and 500 meters(7°C), with an interval of 8 hours. The energy output within one cycle was shown to be 6100 J (1.7 kWh), approximately 110% the energy required to power the entire float. Yang *et al.* developed a PCM-based thermal engine, which was designed to drive the buoyancy-driven system of an underwater glider [45]. The underwater glider, integrated with the thermal engine, completed 113 diving profiles within 27 days. Kim *et al.* used computational fluid dynamics (CFD) methods to conducted a numerical analysis of the nonlinear correlation between energy harvesting and consumption of floats, which were integrated with and powered by PCM-based thermal engines [46]. The designs with different shapes and orientations of the float were investigated in order to achieved an optimal energy allocation.

As introduced above, researchers have made significant efforts to demonstrate the feasibility of harvesting ocean thermal energy with PCMs. However, the existing researches still have two limitations. Firstly, there is lack of theoretical analysis of the energy conversion mechanism underlying the proposed approach. Most of the past researches have focused on the experimental implementation of using PCMs to extract energy from the ocean thermocline [11, 45, 47]. The theoretical full potential of the PCM-based approach has never been investigated. Beside, for the purpose of performance improvement, only a simple analysis of the relationship between the initial system pressure and the energy output has been conducted [45, 47]. Secondly, the analysis of the integrated system, consisting of an AUV and PCM-based ocean thermal energy harvesting modulus, is limited to the hydrodynamic characteristics. When traveling underwater, the structure of the integrated system has been

assumed to be rigid [46] and the dynamic structural response has not been considered. However, it is quite necessary to investigate the fluid-structure interaction characteristics of an integrated system in operation, which are associated with the overall mission profile and reliability of the whole system.

1.4 Dissertation contributions and outline

1.4.1 Dissertation contributions

The contributions of this work can be summarized as follows:

1. A solid/liquid phase change thermodynamic model has been developed for the PCM-based ocean thermal energy harvesting approach, in which the experimentally validated Tait equation of state (EOS) is used to model the thermodynamic behavior of PCM. Using the thermodynamic model, a more specific and tighter thermal efficiency upper-bound for the PCM-based thermal energy harvesting approach has been derived, which can help better assess the theoretical full potential of the proposed energy harvesting approach.

2. To demonstrate the feasibility of the PCM-based ocean thermal energy harvesting approach experimentally, a prototypical thermal energy harvesting system has been designed, fabricated and tested in the laboratory environment. Moreover, to predict the performance of specific designs of the prototypical system, a thermo-mechanical

model, which couples the thermodynamic behaviors of fluid materials and the elastic behavior of the structural system, has been developed and validated basing on the comparison with the experimental measurement. The validated thermo-mechanical model is used to conduct a parametric study, which provides some preliminary design guidance towards the performance improvement of the prototypical system.

3. Basing on the design guidance provided by the parametric study, the design of a new, scalable and portable PCM-based ocean thermal energy harvester is proposed. As an implementation of this new design, a lab-scale prototypical system is fabricated and tested. Furthermore, the aforementioned thermo-mechanical model is modified accordingly, in order to predict the performance of systems with the new design. A parametric study is also conducted for the new design with the modified thermo-mechanical model. Basing on the combined analysis of the fabricated prototype and the parametric study, a critical issue in the design of PCM-based thermal energy harvesting systems is revealed and discussed, that is, it is typically necessary to maintain a very high pressure (e.g., above 100 MPa) within the device to achieve a good performance in terms of both thermal efficiency and specific energy output. This will definitely bring about a serious challenge to the structural design. To mitigate the issue, the idea of using a hydraulic accumulator to regulate the internal pressure is proposed and investigated.

4. A spatial-varying Robin transmission condition for fluid-structure coupled problems with strong added-mass effect has been proposed and investigated using FSI model

problems. This can be a potential method for the future researches about the fluid-structure interaction characteristics of the AUVs, which are integrated with and powered by PCM-based ocean energy harvesting modulus, while traveling underwater.

1.4.2 Outline

This document is organized in the manuscript (multi-paper) format, in which each of the main chapters is in the format of a peer-reviewed article. The remainder of this document is organized as follows. Chapter 2 presents the development of a solid/liquid thermodynamic model and a thermo-mechanical model, as well as the design, fabrication and experimental testing of a specific energy harvester. In Chapter 3, a new scalable and portable design of the PCM-based thermal energy harvester is presented. In addition, a combined experimental and theoretical analysis of the application of a hydraulic accumulator is presented, which is aimed at regulating the peak pressure within the device and improving the performance of PCM-based thermal energy harvesting systems. Chapter 4 presents a spatially-varying Robin transmission condition for fluid-structure coupled problems with strong added-mass effect. The effects of the proposed method on both the accuracy and stability of solutions are investigated in detail. Finally, conclusions and future work are summarized in Chapter 5.

Bibliography

[1] M. A. Eltawil, Z. Zhengming, L. Yuan, A review of renewable energy technologies integrated with desalination systems, Renewable and Sustainable Energy Reviews 13 (9) (2009) 2245–2262.

[2] J. Chow, R. J. Kopp, P. R. Portney, Energy resources and global development, Science 302 (5650) (2003) 1528–1531.

[3] I. Dincer, Renewable energy and sustainable development: a crucial review, Renewable and sustainable energy reviews 4 (2) (2000) 157–175.

[4] N. Panwar, S. Kaushik, S. Kothari, Role of renewable energy sources in environmental protection: A review, Renewable and Sustainable Energy Reviews 15 (3) (2011) 1513–1524.

[5] G. Boyle, Renewable energy, Renewable Energy, by Edited by Godfrey Boyle, pp. 456. Oxford University Press, May 2004. ISBN-10: 0199261784. ISBN-13: 9780199261789 (2004) 456.

[6] J. M. Northrup, G. Wittemyer, Characterising the impacts of emerging energy development on wildlife, with an eye towards mitigation, Ecology letters 16 (1) (2013) 112–125.

[7] R. Pelc, R. M. Fujita, Renewable energy from the ocean, Marine Policy 26 (6) (2002) 471–479.

[8] K. Gunn, C. Stock-Williams, Quantifying the global wave power resource, Renewable Energy 44 (2012) 296–304.

[9] Q. Schiermeier, J. Tollefson, T. Scully, A. Witze, O. Morton, Energy alternatives: Electricity without carbon, Nature News 454 (7206) (2008) 816–823.

[10] M. Melikoglu, Current status and future of ocean energy sources: A global review, Ocean Engineering 148 (2018) 563–573.

[11] Y. Chao, Autonomous underwater vehicles and sensors powered by ocean thermal energy, in: OCEANS 2016-Shanghai, IEEE, 2016, pp. 1–4.

[12] P. G. Fernandes, P. Stevenson, A. S. Brierley, F. Armstrong, E. J. Simmonds, Autonomous underwater vehicles: future platforms for fisheries acoustics, ICES Journal of Marine Science 60 (3) (2003) 684–691.

[13] J. Bellingham, Platforms: autonomous underwater vehicles.

[14] R. B. Wynn, V. A. Huvenne, T. P. Le Bas, B. J. Murton, D. P. Connelly, B. J. Bett, H. A. Ruhl, K. J. Morris, J. Peakall, D. R. Parsons, et al., Autonomous underwater vehicles (auvs): Their past, present and future contributions to the advancement of marine geoscience, Marine Geology 352 (2014) 451–468.

[15] T. B. Curtin, D. M. Crimmins, J. Curcio, M. Benjamin, C. Roper, Autonomous underwater vehicles: trends and transformations, Marine Technology Society Journal 39 (3) (2005) 65–75.

[16] T. Hardy, G. Barlow, Unmanned underwater vehicle (uuv) deployment and retrieval considerations for submarines, in: International Naval Engineering Conference and Exhibition 2008, 2008.

[17] KONGSBERG, Autonomous underwater vehicle, remus 100.
URL https://www.km.kongsberg.com/ks/web/nokbg0240.nsf/AllWeb/D241A2C835DF40B0C12574AB003EA6AB?OpenDocument

[18] L. A. Gish, Design of an auv recharging system, Tech. rep., MASSACHUSETTS INST OF TECH CAMBRIDGE (2004).

[19] K. Vestgård, R. Hansen, B. Jalving, O. Pedersen, The hugin 3000 survey auv–design and field results, Proceeding from Underwater Intervention.

[20] G. Schubak, D. Scott, A techno-economic comparison of power systems for autonomous underwater vehicles, IEEE journal of oceanic engineering 20 (1) (1995) 94–100.

[21] D. E. Frye, J. Kemp, W. Paul, D. Peters, Mooring developments for autonomous ocean-sampling networks, IEEE journal of oceanic engineering 26 (4) (2001) 477–486.

[22] G. MacKerron, Financial considerations of exploiting fuel cell technology, Journal of power sources 86 (1-2) (2000) 28–33.

[23] G. Sattler, Fuel cells going on-board, Journal of power sources 86 (1-2) (2000) 61–67.

[24] D. Morrisey, M. Cameron, E. Newcombe, Effects on moorings on different types of marine habitat (2018).

[25] X. Wang, J. Shang, Z. Luo, L. Tang, X. Zhang, J. Li, Reviews of power systems and environmental energy conversion for unmanned underwater vehicles, Renewable and Sustainable Energy Reviews 16 (4) (2012) 1958–1970.

[26] I. López, J. Andreu, S. Ceballos, I. M. de Alegría, I. Kortabarria, Review of wave energy technologies and the necessary power-equipment, Renewable and sustainable energy reviews 27 (2013) 413–434.

[27] M. Krawczewicz, E. Greene, Micro ocean renewable energy (2010).
URL http://www.ericgreeneassociates.com/images/Micro_Ocean_Renewable_Energy.pdf

[28] F. O. Rourke, F. Boyle, A. Reynolds, Tidal energy update 2009, Applied Energy 87 (2) (2010) 398–409.

[29] P. A. Lynn, Electricity from wave and tide: an introduction to marine energy, John Wiley & Sons, 2013.

[30] T. A. Adcock, S. Draper, T. Nishino, Tidal power generation–a review of hydrodynamic modelling, Proceedings of the Institution of Mechanical Engineers, Part A: Journal of Power and Energy 229 (7) (2015) 755–771.

[31] F. O. Rourke, F. Boyle, A. Reynolds, Renewable energy resources and technologies applicable to ireland, Renewable and Sustainable Energy Reviews 13 (8) (2009) 1975–1984.

[32] P. L. Fraenkel, Tidal current energy technologies, Ibis 148 (2006) 145–151.

[33] U. N. D. of International Economic, S. Affairs, A guide to ocean thermal energy conversion for developing cuontries (1984).

[34] X. Wang, H. Li, L. Gu, Economic and environmental benefits of ocean thermal energy conversion, Marine Sciences 32 (11) (2008) 84–87.

[35] D. Lennard, The viability and best locations for ocean thermal energy conversion systems around the world, Renewable Energy 6 (3) (1995) 359–365.

[36] D. Tanner, Ocean thermal energy conversion: current overview and future outlook, Renewable energy 6 (3) (1995) 367–373.

[37] L. A. Vega, Ocean thermal energy conversion primer, Marine Technology Society Journal 36 (4) (2002) 25–35.

[38] Makai Ocean Engineering, Makai connects world's largest ocean thermal plant to u.s. grid, [Online; accessed 13-April-2017] (2015).
URL https://www.makai.com/makai-news/2015_08_29_makai_connects_otec/

[39] M. Bohn, D. Benson, T. Jayadev, Thermoelectric ocean thermal energy conversion, Journal of Solar Energy Engineering 102 (2) (1980) 119–127.

[40] N. Khan, A. Kalair, N. Abas, A. Haider, Review of ocean tidal, wave and thermal energy technologies, Renewable and Sustainable Energy Reviews 72 (2017) 590–604.

[41] J. Von der Weid, J. Da Silva, A. Gama, A. Sant'Anna, Subsea electric generator, in: Proceedings of OCEANS'93, IEEE, 1993, pp. II–172.

[42] A. Sharma, V. V. Tyagi, C. Chen, D. Buddhi, Review on thermal energy storage with phase change materials and applications, Renewable and Sustainable energy reviews 13 (2) (2009) 318–345.

[43] J. A. Jones, Y. Chao, T. I. Valdez, Phase change material thermal power generator, uS Patent 7,987,674 (Aug. 2 2011).

[44] J. A. Jones, Y. Chao, T. I. Valdez, Phase change material thermal power generator, uS Patent 8,689,556 (Apr. 8 2014).

[45] Y. Yang, Y. Wang, Z. Ma, S. Wang, A thermal engine for underwater glider driven by ocean thermal energy, Applied Thermal Engineering 99 (2016) 455–464.

[46] H. Kim, J.-Y. Choi, J. Park, M. Ruda, R. Prasad, Y. Chao, T. Curtin, S. Choi, Towards the optimal operation of a thermal-recharging float in the ocean, Ocean Engineering 156 (2018) 381–395.

[47] Z. Ma, Y. Wang, S. Wang, Y. Yang, Ocean thermal energy harvesting with phase change material for underwater glider, Applied energy 178 (2016) 557–566.

Chapter 2

Harvesting Environmental Thermal Energy Using Solid/Liquid Phase Change Materials

(Published in *Journal of Intelligent Material Systems and Structures*, 29(8), 1632-1648, 2018.)

G. Wang [a], D. S. Ha [b], K. G. Wang [a]

[a] Department of Aerospace and Ocean Engineering, Virginia Polytechnic Institute and State University, Blacksburg, VA 24061, United States

[b] Department of Electrical and Computer Engineering, Virginia Polytechnic Institute and State University, Blacksburg, VA 24061, United States

Under Dr. Kevin Wang's supervision, I contributed all the contents in this chapter.

Abstract

This paper investigates the feasibility of using solid/liquid phase change materials (PCMs) to harvest the renewable thermal energy in various natural environments, which is often associated with a low temperature differential. The basic idea is to move the PCM cyclically through the temperature differential, and convert a fraction of the energy absorbed by the PCM in its melting process into mechanical or electrical energy. In this work, we first develop a thermodynamic model for an idealized setting, thereby deriving a theoretical upper limit of the thermal efficiency. Next, we couple the thermodynamic model with a structural mechanics model based on Kirchhoff-Love plate theory, in order to predict the performance of specific devices. To validate the thermomechanical model and demonstrate the feasibility of the underlying approach, we develop a prototype that uses pentadecane ($C_{15}H_{32}$) as the PCM. The measured specific energy agrees favorably with the model prediction. Finally, we employ the validated model to conduct a parameter study. The result implies that stiffer structures and PCMs with high solid/liquid density ratio are preferred. The study also suggests that, compared to bismutch telluride (Bi_2Te_3) based thermoelectric generators (TEGs), the PCM-based approach may yield significantly higher efficiency when the temperature differential is less than 100 °C.

Keywords

Renewable energy, Energy harvesting, Phase change materials, Prototyping, Thermo-mechanical analysis, Model validation

2.1 Introduction

Technologies for harvesting renewable energy has been a focal area of research in the past few decades [1, 2]. On one hand, the rapidly growing energy demand and worldwide environmental concerns have motivated the development of large-scale devices for renewable electricity generation, which may help reduce the use of fossil fuels [3, 4]. On the other hand, the need of self-sustained and autonomous engineering systems has also motivated the development of small-scale, portable renewable energy harvesters [5, 6, 7].

In this work, we consider thermal energy resources in natural environments, which are often renewable, abundant, yet associated with a relatively low temperature differential. A case in point is the thermal energy stored in the ocean thermocline, associated with the vertical temperature variation from ocean surface to several hundred meters in depth. It is estimated that every year, 1.09×10^{19} MJ of solar energy is deposited in the ocean thermocline [8, 9]. However, the temperature differential is only between 10 and 20°C. Other examples include geothermal resources, the energy associated with diurnal temperature variation, as well as the temperature variation induced by the altitude change [10, 11, 12].

Various approaches have been proposed and implemented in the past to harvest thermal energy with small temperature variation [6, 13, 14, 15, 16]. One approach is to run a heat engine through a Rankine cycle, and use the vaporized working fluid to generate electricity. This approach has been employed to build power plants up to 100 kW [17] that harvest the ocean thermal energy. The main idea is to use the ocean's warm surface water to vaporize a working fluid (e.g., ammonia) and drive a turbine, while cold water is pumped up from deep ocean (e.g., 500 – 1000 m below surface) to recondense the vapor [18, 19, 13]. However, due to the need of complex piping system, this approach is difficult to implement at small scales. Another approach that has been effectively used in small, portable devices is thermoelectric generators (TEGs) [15]. For example, Brogan *et al.* developed a wearable energy harvesting jacket with Bi_2Te_3 thermoelectric generators (TEGs), which harvests the thermal energy from the temperature difference between the human body and environment [6]. The maximum power achieved by the energy harvesting jacket was 1.25 μW with the temperatures of human body and environment at 37°C and 25°C, respectively. Chen *et al.* developed a Bi_2Te_3 thermoelectric energy harvester to power sensors on heating/cooling, steam, or exhaust pipes [16]. The energy source is the temperature difference between heat pipes and the environment. This device generates 2.25 W $\pm$ 0.13 W power output with a temperature difference of 128°C $\pm$ 1.12°C.

Recently, a new approach has been developed for harvesting thermal energy from small temperature differentials, which utilizes the volume change of phase change materials (PCMs, e.g., $C_{15}H_{32}$) in the solid/liquid phase transition process [20, 21]. In the context of energy

harvesting and storage, PCM refers to a class of materials that have high latent heat and tunable melting temperatures [22]. As the PCM moves between two thermal reservoirs below and above the melting temperature, the PCM freezes and melts cyclically (Fig. 2.1). In the meantime, the volume of PCM will contract and expand accordingly. For example, pentadecane ($C_{15}H_{32}$), which has a melting temperature of 10°C, expands by 12% at atmospheric pressure in the melting process [23]. The volume change can be utilized to do useful work, e.g. driving an electromagnetic generator (EMG), thereby generating electricity. This approach can be implemented at small scales, as it does not require a complex structural system. For example, a prototype system has been developed by Chao *et al.* [24], which can provide $6,100$ J of energy per dive to an autonomous underwater vehicle (Fig. 2.2). However, the efficiency of existing PCM-based systems is low, which limits their application. For example, the thermal efficiency of the aforementioned PCM-based thermal charging engine is approximately 1% when operating between 0 and 20°C. This is significantly lower than the Carnot efficiency, which is approximately 6.8% for this temperature range.

The overall objective of this study is to investigate the possibility of improving the thermal efficiency of the PCM-based approach for harvesting thermal energy from small temperature variations. First, we note that the Carnot efficiency mentioned above represents a loose upperbound for all heat engines, not only PCM-based systems. To better assess the potential of PCM-based systems, a more specific and tighter upperbound is desirable. To this end, we propose a liquid/solid phase change thermodynamic model based on an experimentally validated Tait equation of state, which may represent an idealized PCM-based energy harvester.

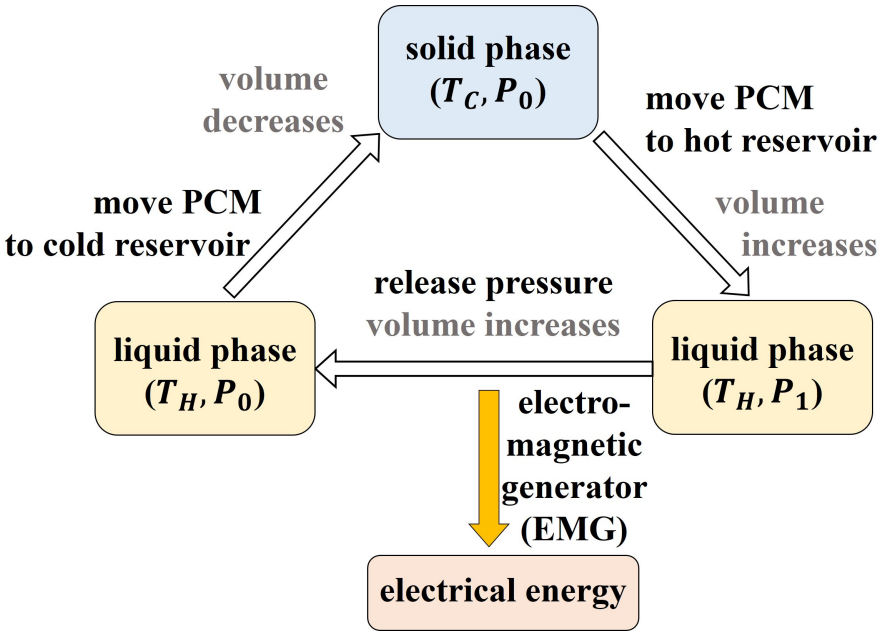

Figure 2.1: Mechanism of PCM-based energy harvesting. T_C and T_H refer to the temperature of the cold and hot thermal reservoirs, respectively. P_0 denotes the ambient pressure. P_1 ($> P_0$) represents the high pressure inside melted PCM.

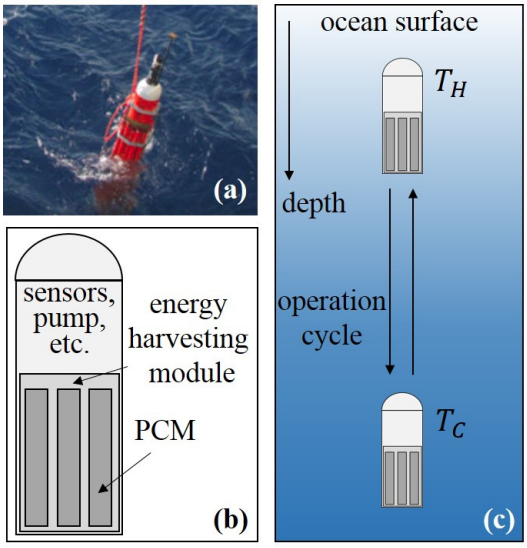

Figure 2.2: An underwater vehicle powered by a PCM-based thermal charging engine [24]. (a) a photograph of the vehicle taken during an ocean endurance test near the coast of Hawaii. (b) A schematic drawing of the vehicle. (c) the energy harvesting mechanism

Using this thermodynamic model, we derive an efficiency upperbound for PCM-based energy harvesters, and compare it with the Carnot efficiency, and the efficiency of state-of-the-art TEGs. Second, we propose that a physical model capable of predicting the performance of specific harvesters is useful for design and optimization purposes. Therefore, we develop a thermomechanical model that accounts for the thermodynamic behaviors of the fluid materials — including both PCM and working fluid — and the elastic behavior of the structural system of the harvester. To validate the model, we develop and characterize a prototypical harvester that uses pentadecane as the PCM. The prototype features a metal container that stores the harvested thermal energy as its strain energy. It uses a hydraulic working fluid to drive an electromagnetic generator (EMG), thereby converting the stored strain energy into electrical energy. To assess the fidelity of the thermomechanical model, we compare the predicted energy output with the corresponding experimental measurement. Finally, we apply the model to conduct a parameter analysis, thereby providing some preliminary guidance towards improving the performance of PCM-based energy harvesting systems.

In the following sections, we first present the idealized thermodynamic cycle underlying the energy conversion from thermal energy to mechanical energy, the derivation of an efficiency upper limit and the development of the thermomechanic model. Then, the details of the prototype systems for thermal energy harvesting and experimental results are shown. Furthermore, the validation of the thermomechanic model and a series of parameter studies are presented. Finally, several concluding remarks are provided.

2.2 Physical model of PCM-based energy harvesters

Figure 2.1 presents the general approach of PCM-based energy harvesting. Specifically, when the PCM is moved from the cold thermal reservoir to the hot one, it absorbs thermal energy from the environment, and converts it into the internal energy of the PCM — including the latent heat associated with its solid/liquid phase change — and the elastic energy of both the PCM and a structural system (e.g., a piston). Next, the elastic energy can be released to drive an electromagnetic generator (EMG), thereby converting a fraction of the harvested energy to electricity. The efficiency of state-of-the-art EMGs can reach 50% to 70% [25]. However, the thermal efficiency of current PCM-based harvesters is found to be only a few percents (or less) when operating with a temperature differential less than 100°C. To rigorously investigate the energy harvesting process, we first present a thermodynamic model for an idealized setting in which the structural system is assumed to be rigid, then extend it into a multi-material thermomechanical model for practical PCM-based energy harvesters.

2.2.1 An idealized phase-change thermodynamic model

In an idealized setting, the structural system of the harvester is assumed to be completely rigid. Therefore its volume does not change during the melting process, and it does not store elastic energy. Moreover, it is assumed that the PCM is the only material involved in the thermodynamic cycle, despite the fact that existing devices often use a hydraulic fluid (e.g.,

mineral oil) to drive the EMG. In other words, the model involves a given amount of PCM enclosed in a rigid container that transfers heat.

The Tait equation [26] is used as the equation of state (EOS) to model the thermodynamic behavior of the PCM in liquid phase. It can be expressed as

$$v_0(T) - v(P,T) = C(T) \log\left(1 + \frac{P - P_0}{B(T)}\right), \tag{2.1}$$

where v denotes the specific volume of the PCM. v_0 is the specific volume under the ambient pressure P_0, which is set to be the atmospheric pressure (101 kPa) throughout this study. B and C are empirical coefficients of Tait equation, which depend on temperature T. log represents the base-10 logarithm function. Tait equation is widely used to model the thermodynamic behavior of liquid materials, including liquid water [27] and a number of PCMs in their liquid phase, such as decane ($C_{10}H_{32}$), pentadecane ($C_{15}H_{32}$) and heptadecane ($C_{17}H_{36}$) [28]. Without loss of generality, $C_{15}H_{32}$ is taken as an example to formulate the thermodynamic model. [29] derived the values of B and C for $C_{15}H_{32}$, which is applicable for $10°C < T < 135°C$, using compression experiments. These values are given by

$$B(T) = 762.8 - 4.805 \times (T - 79.4) + 0.0116 \times (T - 79.4)^2 \tag{2.2}$$

$$C(T) = 0.2058 \times v_0(T) \tag{2.3}$$

where T, B, and C has the unit of °C, MPa, and m^3/kg, respectively. [30] presented an

expression for $v_0(T)$ in the form of a third-order polynomial, given by

$$\begin{aligned} v_0(T) &= [(1.0307 \times 10^3 - 1.2596 \times (T + 273.15) + 1.8186 \times 10^{-3} \times (T + 273.15)^2 \\ &\quad -1.9555 \times 10^{-6} \times (T + 273.15)^3]^{-1}. \end{aligned} \tag{2.4}$$

Figure 2.3 presents the $P - v$ curves predicted by the Tait EOS for a range of temperatures relevant to the present study, which are in close agreement with experimental measurements.

As will be discussed later, the thermodynamic processes in the solid region and solid-liquid mixture region are isochoric or isobaric, which can be represented as vertical or horizontal straight lines in the $P - V$ diagram. Therefore, these processes can be analyzed only with the start and end states, and the EOS for the PCM in the solid phase is not required.

The melting temperature (denoted by T_m) of $C_{15}H_{32}$ is 10°C at the atmospheric pressure (P_0) [31]. Given that the container is assumed to be rigid, the volume of PCM remains constant through the melting process. Therefore, the pressure of PCM will dramatically change. Hence, the dependence of melting temperature on pressure must be taken into consideration. In this regard, Daridon *et al.* [30] and Milhet *et al.* [32] have measured the melting temperature of $C_{15}H_{32}$ between 0.1 and 150 MPa. Their results are presented in Fig. 2.4, together with a least-square linear regression, which extends to $P = 450$ MPa. This regression function is given by

$$T_m(P) = kP + n, \tag{2.5}$$

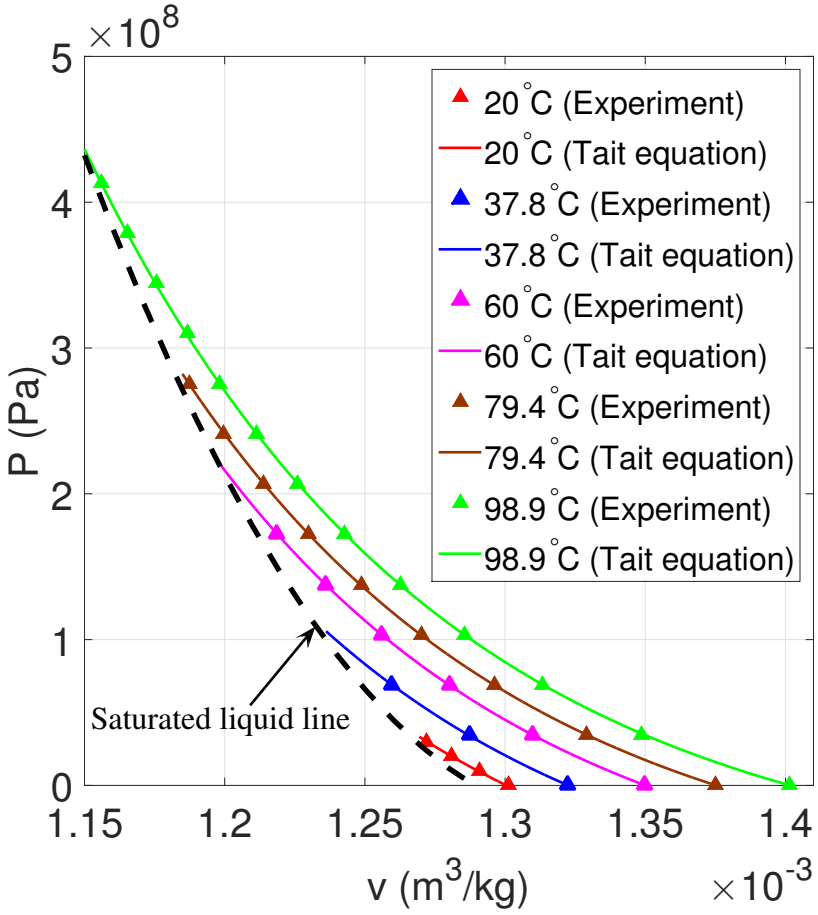

Figure 2.3: $P-v$ curves for $C_{15}H_{32}$ (liquid phase) at different temperatures: comparison between experimental measurement and the prediction of the Tait EOS. (Experimental results at $T = 20°C$ are obtained from Daridon *et al.* [30]. Other experimental results presented in this figure are from Cutler *et al.* [29].)

where $k = 0.2022$ K/MPa and $n = 283.15$ K. The coefficient of determination (denoted by R^2) is 0.99. Therefore, Eq. (2.5) is a good representation of the experimental data.

Clearly, T_m increases as pressure increases. Therefore, there exists a critical temperature T_{cm}, greater than 10°C, such that the PCM ($C_{15}H_{32}$) completely melts if and only if the temperature of the hot reservoir (T_H) is greater than T_{cm}. More specifically, T_{cm} — and the corresponding pressure P_{cm} — is the root of Eqs. (2.5) and (2.1), with fixed specific volume

$$v(P, T) = \frac{1}{\rho_s}, \tag{2.6}$$

where ρ_s is the density of the PCM in solid phase. In this work, $\rho_s = 861$ kg/m^3, measured at temperature $T = 1$°C (i.e. T_C) and pressure $P = 0.1$ MPa (i.e. P_0). A straightforward calculation gives

$$T_{cm} = 84.5°\text{C}, \tag{2.7}$$

which is also shown in Fig. 2.4, as the intersection of the isochore of liquid PCM — obtained from the Tait EOS (Eq. 2.1) with $v = \frac{1}{\rho_s}$ — with the melting temperature T_m formulated in Eq. (5) and fitted to experimental data [30, 32].

In the scenario of $T_H > T_{cm}$, the thermodynamic cycle underlying PCM-based energy harvesting is presented in Fig. 2.5(a). It consists of three processes as follows.

- **Proc. 1: Isochoric phase change** (State 0 to State 1 in Fig. 2.5(a)). At State 0, PCM is in the solid phase (or in the extreme case, on the saturated solid line), with temperature

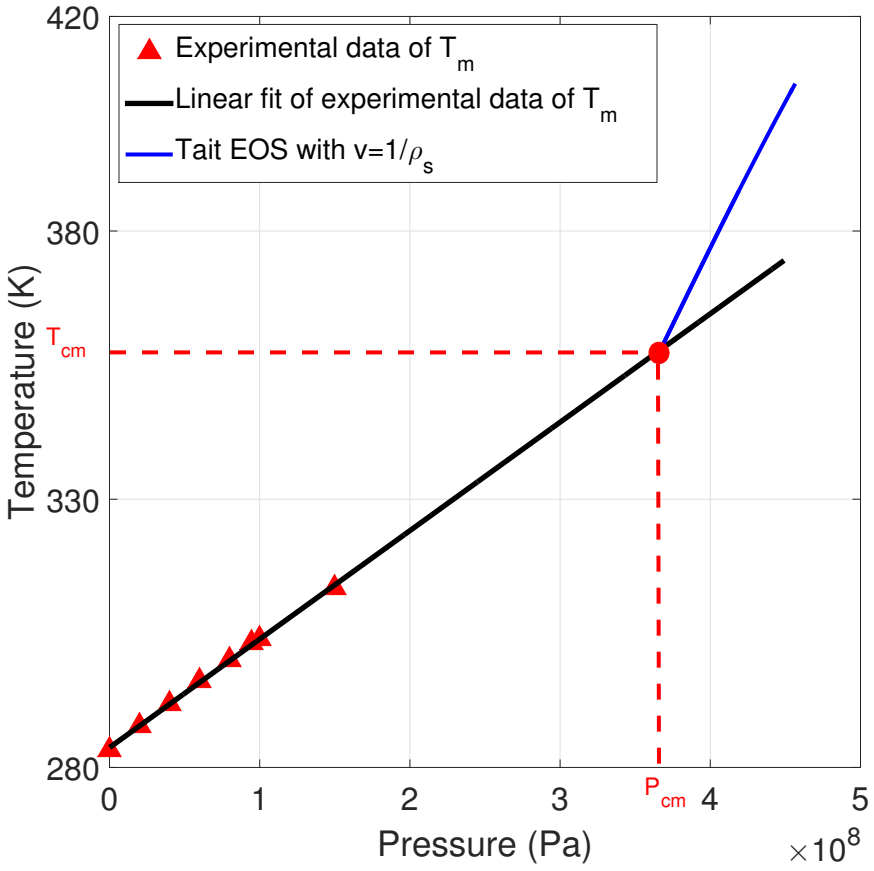

Figure 2.4: Identification of T_{cm}, the minimum temperature for complete melting of pentadecane at fixed specific volume $v = \dfrac{1}{\rho_s}$

T_C, pressure P_0, and volume

$$V_0 = \frac{m^{PCM}}{\rho_s}, \tag{2.8}$$

where m^{PCM} is the mass of PCM. During this process, PCM absorbs heat from the hot thermal reservoir with T_H and melts. Both the temperature and the pressure increase, whereas the volume remains constant. At State 1, PCM has completely melted. Its temperature reaches T_H, and its pressure increases to

$$P_1 = B(T_H)(10^{\frac{v_0(T_H)-\frac{1}{\rho_s}}{C(T_H)}} - 1) + P_0, \tag{2.9}$$

according to Eq. (2.1).

- **Proc. 2: Isothermal expansion** (State 1 to State 2 in Fig. 2.5(a)). The pressure is released in an isothermal process, in which the volume of PCM is allowed to expand slowly and PCM does work to the surroundings. In this process, the relation between pressure and volume is

$$P(V) = B(T_H)(10^{\frac{v_0(T_H)-\frac{V}{m^{PCM}}}{C(T_H)}} - 1) + P_0, \tag{2.10}$$

while the temperature retains the constant value of T_H. After the pressure reaches P_0, the system reaches State 2, with volume

$$V_2 = \frac{m^{PCM}}{\rho_l}, \tag{2.11}$$

where ρ_l is the density of liquid PCM at pressure P_0 and temperature T_H.

- **Proc. 3: Isobaric phase change** (State 2 to State 0 in Fig. 2.5(a)). The system is moved to the cold thermal reservoir at T_C. The PCM freezes, with pressure maintained at P_0. Both the temperature and the volume decrease. After PCM solidifies and the temperature of the system reaches T_C, the system goes back to State 0.

In the scenario of $T_H \leq T_{cm}$, the thermodynamic cycle underlying PCM-based energy harvesting is presented in Fig. 2.5(b). It consists of four processes as follows.

- **Proc. 1: Isochoric phase change** (State 0 to State 1' in Fig. 2.5(b)). State 0 is the same as that of the thermodynamic cycle for $T_H > T_{cm}$. Similar to Proc. 1 for $T_H > T_{cm}$, PCM absorbs heat from the hot thermal reservoir with T_H and melts. Both the temperature and the pressure increase, whereas the volume remains constant. As the pressure increases, the melting temperature of PCM also increases. State 1' characterizes the state in which the melting temperature reaches T_H. Here, the melting process stops; and the liquid and solid phases of PCM co-exist. The pressure in State 1' is determined by Eq. (2.5) as

$$P_{1'} = \frac{T_H - n}{k}. \tag{2.12}$$

- **Proc. 2: Isobaric expansion** (State 1' to State 1 in Fig. 2.5(b)). The volume of PCM is allowed to expand slowly in an isobaric process and PCM does work to the surround-

ings. PCM continues absorbing heat from the hot thermal reservoir with T_H and the melting process proceeds. After PCM completely melts, the system reaches State 1. This process is isobaric, and the pressure in State 1 is $P_1 = P_{1'}$. The volume of PCM in State 1 is

$$V_1 = m^{PCM}(v_0(T_H) - C(T_H)\log(1 + \frac{P_1 - P_0}{B(T_H)})). \tag{2.13}$$

- **Proc. 3: Isothermal expansion** (State 1 to State 2 in Fig. 2.5(b)). This process is the same as Proc. 2 in the scenario of $T_H > T_{cm}$, except that the volume of PCM starts at V_1.

- **Proc. 4: Isobaric phase change** (State 2 to State 0 in Fig. 2.5(b)). This process is the same as Proc. 3 in the scenario of $T_H > T_{cm}$.

The total thermal energy absorbed by PCM in one melting-freezing cycle is

$$Q = \Big(\int_{T_C}^{T_H} c_p(T)dT \Big) m^{PCM} + \Delta H_m m^{PCM} + W, \tag{2.14}$$

where $c_p(T)$ is the specific heat capacity of the PCM at pressure P_0. ΔH_m is its latent heat capacity. W is the work done by the PCM to the environment, which is equal to the area enclosed by the P-V curve in the thermodynamic cycle (Fig. 2.5). The specific heat capacity of $C_{15}H_{32}$ can be approximated as a piecewise linear function of temperature with

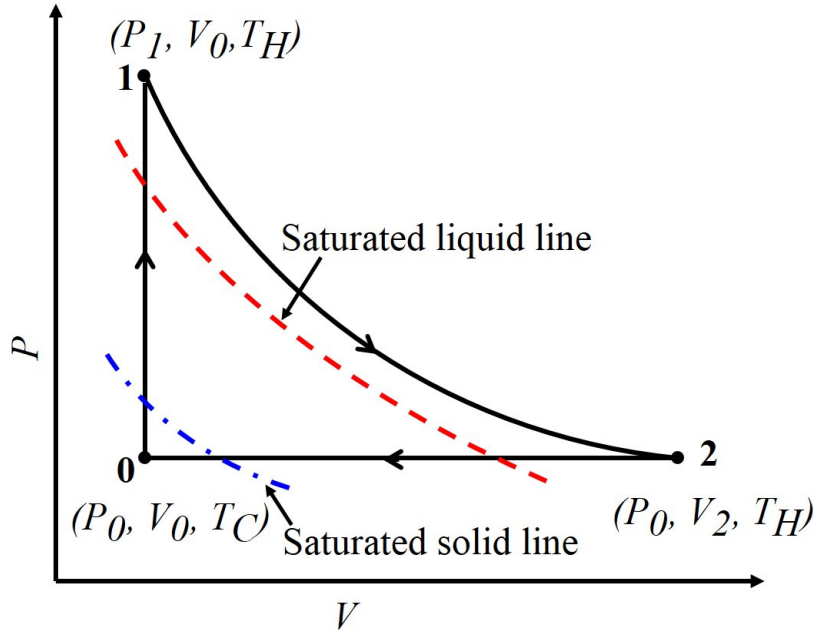

(a) $T_H > T_{cm}$

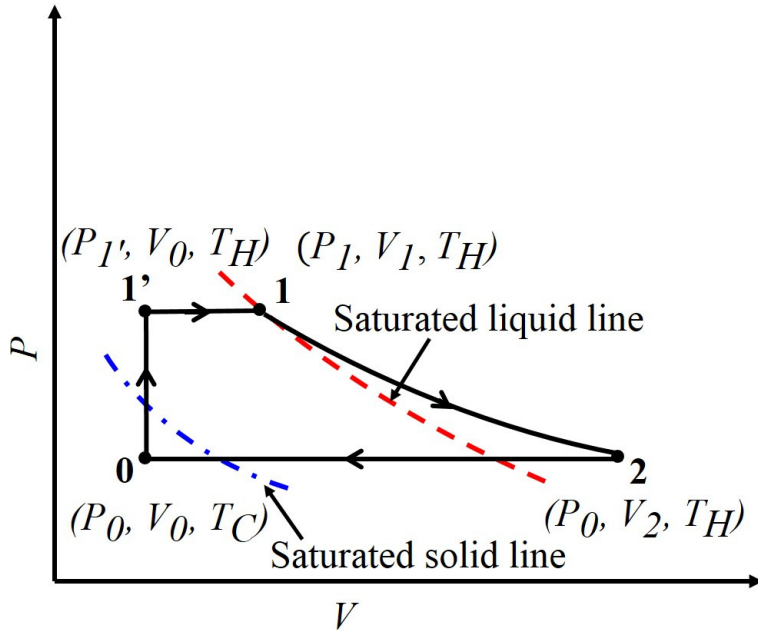

(b) $T_H \leq T_{cm}$

Figure 2.5: Illustration of the idealized thermodynamic cycle underlying PCM-based energy harvesting

a discontinuity at $T = 283.15$ K(10°C), i.e. the melting temperature at pressure P_0 [31], i.e.

$$c_p(T) = \begin{cases} 1880 \text{ J/kgK}, & \text{if } T < 283.15\text{K} \\ 2.57 \times T + 1454.73 \text{ J/kgK}, & \text{if } T > 283.15\text{K} \end{cases} \tag{2.15}$$

The latent heat capacity of $C_{15}H_{32}$ is $\Delta H_m = 205$ J/g at pressure P_0 [33]. In the scenario of $T_H > T_{cm}$, the work done by the PCM to the environment is expressed as

$$\begin{aligned} W &= \int_{V_0}^{V_2} (P(V) - P_0)dV \\ &= \int_{V_0}^{V_2} B(T_H)(10^{\frac{\frac{1}{\rho_l} - \frac{V}{m^{PCM}}}{C(T_H)}} - 1)dV \\ &= m^{PCM} B(T_H)(\frac{1}{\rho_s} - \frac{1}{\rho_l} + \frac{C(T_H)}{\ln 10} 10^{\frac{1}{\rho_l C(T_H)} - \frac{1}{\rho_s C(T_H)}} - \frac{C(T_H)}{\ln 10}) \end{aligned} \tag{2.16}$$

When $T_H \leq T_{cm}$, the work done by PCM to the environment is expressed as

$$\begin{aligned} W &= \int_{V_0}^{V_1} (P(V) - P_0)dV + \int_{V_1}^{V_2} (P(V) - P_0)dV \\ &= (P_1 - P_0)(V_1 - V_0) + \int_{V_1}^{V_2} B(T_H)(10^{\frac{\frac{1}{\rho_l} - \frac{V}{m^{PCM}}}{C(T_H)}} - 1)dV \\ &= (P_1 - P_0)(V_1 - V_0) \\ &\quad + B(T_H)(V_1 - \frac{m^{PCM}}{\rho_l} + m^{PCM} \frac{C(T_H)}{\ln 10} 10^{\frac{1}{\rho_l C(T_H)} - \frac{V_1}{m^{PCM} C(T_H)}} \\ &\quad - m^{PCM} \frac{C(T_H)}{\ln 10}) \end{aligned} \tag{2.17}$$

Therefore, the thermal efficiency is given by

$$\begin{aligned}
\eta_{PCM} &= \frac{W}{Q} \\
&= \frac{W}{\Big(\int_{T_C}^{T_H} c_p(T)dT\Big)m^{PCM} + \Delta H_m m^{PCM} + W} \\
&= \begin{cases} \dfrac{w_l}{\int_{T_C}^{T_H} c_p(T)dT + \Delta H_m + w_l}, & \text{if } T_H > T_{cm} \\ \dfrac{w_s}{\int_{T_C}^{T_H} c_p(T)dT + \Delta H_m + w_s}, & \text{if } T_H \leq T_{cm} \end{cases}
\end{aligned} \tag{2.18}$$

where

$$w_l = B(T_H)\left(\frac{1}{\rho_s} - \frac{1}{\rho_l} + \frac{C(T_H)}{\ln 10} 10^{\frac{1}{\rho_l C(T_H)} - \frac{1}{\rho_s C(T_H)}} - \frac{C(T_H)}{\ln 10}\right), \tag{2.19}$$

$$\begin{aligned}
w_s &= B(T_H)\left(v_1 - \frac{1}{\rho_l} + \frac{C(T_H)}{\ln 10} 10^{\frac{1}{\rho_l C(T_H)} - \frac{v_1}{C(T_H)}} - \frac{C(T_H)}{\ln 10}\right) \\
&+ \left(\frac{T_H - n}{k} - P_0\right)\left(v_1 - \frac{1}{\rho_s}\right),
\end{aligned} \tag{2.20}$$

and

$$v_1 = v(P_0, T_H) - C(T_H)\log\left(1 + \frac{\frac{T_H - n}{k} - P_0}{B(T_H)}\right) \tag{2.21}$$

As mentioned in the previous section, thermoelectric generators (TEGs) have also been used to harvest energy from small temperature variations. Following the work of Snyder [34], an

upper limit of the efficiency of TEGs is given by

$$\eta_{TEG} = \eta_C \frac{\sqrt{ZT_{avg}+1}-1}{\sqrt{ZT_{avg}+1}+T_C/T_H}, \tag{2.22}$$

where,η_C is Carnot efficiency, defined as

$$\eta_C = 1 - \frac{T_C}{T_H}, \tag{2.23}$$

and

$$ZT_{avg} = \frac{\sigma S^2}{\kappa}\frac{T_C+T_H}{2} \tag{2.24}$$

is a widely-used figure of merit of TEG. Specifically, σ denotes the electric conductivity of the thermoelectric material, κ is the thermal conductivity of the thermoelectric material. S is the Seebeck coefficient. For state-of-the-art TEGs based on bismuth telluride (Bi_2Te_3), $Z \approx 3 \times 10^{-3}$ K^{-1}.

Figure 2.6 presents the comparison of η_{TEG}, η_{PCM} and η_C as functions of the temperature difference between the two thermal reservoirs ($\Delta T = T_H - T_C$). In this plot, T_C is set to 10°C, and the PCM is assumed to be $C_{15}H_{32}$. As ΔT increases, all the three plotted variables increase. Notably, for 0°C $< \Delta T <$ 100°C, the gradient of η_{PCM} is always greater than that of η_{TEG}, yet smaller than that of η_C. At $\Delta T = 0$, the gradient of η_{PCM} is 3.0×10^{-3} K^{-1}, which is 16 times larger than the gradient of η_{TEG}, and only 14% smaller than that of η_C. In addition, when $\Delta T = 10$°C, η_{PCM} is 4 times larger than η_{TEG} and is only 20% smaller

than η_C. Putting all together, the PCM-based approach may provide better performance than TEGs and other heat engines when operating over small temperature variations.

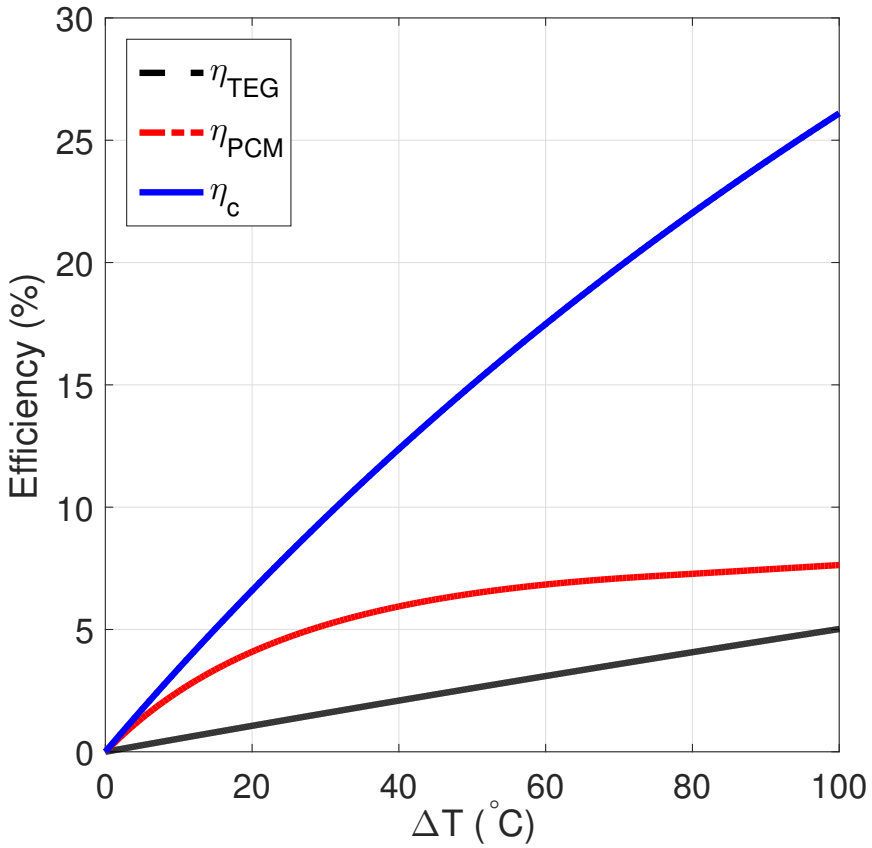

Figure 2.6: Dependence of thermal efficiency on ΔT: Comparison of the PCM-based approach and (Bi_2Te_3) TEG

2.2.2 Thermomechanical model for a prototypical PCM-based energy harvester

Here we model an elastic rectangular box that serves as both the container of the PCM and an energy storage medium. We assume that the PCM is submerged in a hydraulic fluid,

which can be used to drive an EMG. We also account for the fact that there can be a certain amount of residual air in both the PCM and the hydraulic fluid. Therefore, three fluid materials are modeled. Specifically, the PCM and the hydraulic fluid are modeled using Tait EOS (Eq. (2.1)) with different model parameters, i.e.

$$v_0^{PCM}(T) - v^{PCM}(P,T) = C^{PCM}(T)\log\Big(1 + \frac{P - P_0}{B^{PCM}(T)}\Big), \tag{2.25}$$

$$v_0^{H}(T) - v^{H}(P,T) = C^{H}(T)\log\Big(1 + \frac{P - P_0}{B^{H}(T)}\Big), \tag{2.26}$$

where the superscripts PCM and H refer to the phase change material and the hydraulic fluid, respectively. The ideal gas law is applied to model the residual air, which can be expressed as

$$\frac{Pv^{air}}{T} = \text{const.}, \tag{2.27}$$

where v^{air} denotes the specific volume of the residual air.

The deformation of the container under pressure loading is modeled through a linear elasticity theory. Specifically, the six faces of the container are analyzed as plates with clamped boundaries. The deflection of each plate is calculated basing on Kirchhoff-Love plate theory, which assumes small thickness-to-width ratio and small deformation [35]. In this case, the strain energy of a homogeneous rectangular plate is given by

$$U = \frac{D}{2}\int_0^a \int_0^b \left(\frac{\partial^2 \omega}{\partial x^2} + \frac{\partial^2 \omega}{\partial y^2}\right)^2 dx\, dy \tag{2.28}$$

where $\omega(x, y)$ is the displacement of the plate in the normal direction. $D = \dfrac{Et^3}{12(1-\nu^2)}$ is the flexural rigidity of the plate. a, b , and t denote the length, width, and thickness of the plate, respectively. E is the Young's modulus of the plate material. ν denotes its Poisson's ratio.

The work done by the internal pressure to the plate is

$$W_P = \int_0^a \int_0^b (P - P_0)\omega \, dx \, dy \tag{2.29}$$

The total potential energy of the plate is

$$\Pi = U - W_P = \int_0^a \int_0^b \Big[\frac{D}{2} \left(\frac{\partial^2 \omega}{\partial x^2} + \frac{\partial^2 \omega}{\partial y^2} \right)^2 - (P - P_0)\omega \Big] dx \, dy \tag{2.30}$$

Following the Ritz Method [36], a linear combination of basis functions

$$\phi_{mn}(x, y) = \frac{1}{4}(1 - \cos\frac{2m\pi x}{a})(1 - \cos\frac{2n\pi y}{b}), \quad m, n = 1, 2, \ldots, \tag{2.31}$$

parametrized by coefficients $C_{mn},\ m, n = 1, 2, \ldots$, is used to describe plate deflection, i.e.

$$\omega(x, y) = \sum_{m=1}^{\infty} \sum_{n=1}^{\infty} C_{mn} \phi_{mn}(x, y). \tag{2.32}$$

In the present application, the pressure load on the structure is uniform, therefore the infinite

summation in Eq. (2.32) is dominated by the first term, i.e.

$$\omega(x,y) \approx \frac{C_{11}}{4}(1-\cos\frac{2\pi x}{a})(1-\cos\frac{2\pi y}{b}) \tag{2.33}$$

Substituting Eq. (2.33) into Eq. (2.30), the expression of potential energy becomes

$$\Pi = U - W_P = \frac{DC_{11}^2\pi^4}{2ab}(\frac{3b^2}{4a^2}+\frac{3a^2}{4b^2}+\frac{1}{2}) - \frac{1}{4}(P-P_0)C_{11}ab \tag{2.34}$$

Minimization of the total potential energy yields

$$\frac{\partial\Pi}{\partial C_{11}} = \frac{DC_{11}\pi^4}{ab}(\frac{3b^2}{4a^2}+\frac{3a^2}{4b^2}+\frac{1}{2}) - \frac{1}{4}Pab = 0. \tag{2.35}$$

Therefore,

$$C_{11} = \frac{(P-P_0)}{D\pi^4}\frac{a^4b^4}{3a^4+2a^2b^2+3b^4}, \tag{2.36}$$

and the displacement of the plate is given by

$$\omega(x,y) = \frac{(P-P_0)}{4D\pi^4}\frac{a^4b^4}{3a^4+2a^2b^2+3b^4}(1-\cos\frac{2\pi x}{a})(1-\cos\frac{2\pi y}{b}) \tag{2.37}$$

Hence, volume increase of the rectangular container under internal pressure P is given by

$$\begin{aligned}\Delta V^{total} &= \sum_{i=1}^{6}\Big(\int_{\Gamma_i}\omega d\Gamma\Big)\\ &= \sum_{i=1}^{6}\Big(\int_0^{a_i}\int_0^{b_i}\frac{(P-P_0)}{4D\pi^4}\frac{a_i^4b_i^4}{3a_i^4+2a_i^2b_i^2+3b_i^4}(1-\cos\frac{2\pi x}{a_i})(1-\cos\frac{2\pi y}{b_i})\,dx\,dy\Big)\\ &= \frac{P-P_0}{4D\pi^4}\sum_{i=1}^{6}\frac{a_i^5b_i^5}{3a_i^4+2a_i^2b_i^2+3b_i^4},\end{aligned} \tag{2.38}$$

where Γ_i, $i=1,2,...,6$ denote the six faces of the container. a_i and b_i denote the length and width of each rectangular face. The thickness t is assumed to constant, leading to the same D for all the six faces.

Next, we extend the thermodynamic model to account for the thermodynamic behaviors of the hydraulic fluid and the air, as well as the elastic deformation of the container. Fig. 2.7[1] shows the thermodynamic cycle in this case, which can be compared with the idealized setting shown in Fig. 2.5.

It is first assumed that T_H is sufficiently high to completely melt the PCM enclosed in the elastic container, which corresponds to Fig. 2.7(a). As the PCM melts, its volume increases. As a result, the hydraulic fluid and the residual air are compressed, and the container is pressurized. Let V_1^{PCM}, V_1^H and V_1^{air} be the volume of PCM, hydraulic oil, and air at the end of the melting process (i.e. State 1), while P_1^* denotes their pressure and and the superscript $*$ denotes the prototypical energy harvester. Substituting these four unknown variables into Eqs. (3.6), (3.7), (3.8) and (2.38), we obtain the following system of nonlinear

[1]An error was found in the original figure, which has been fixed in the current version.

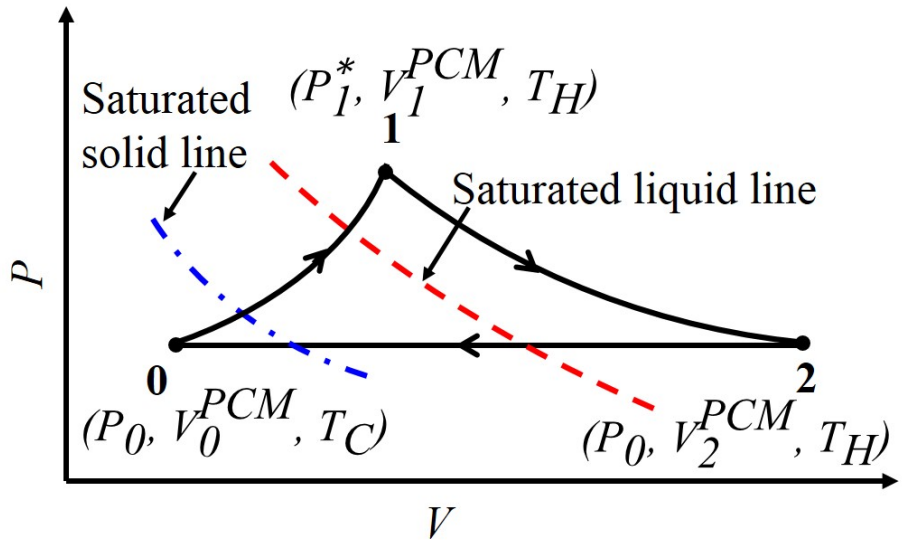

(a) $T_H > T_{cm}$

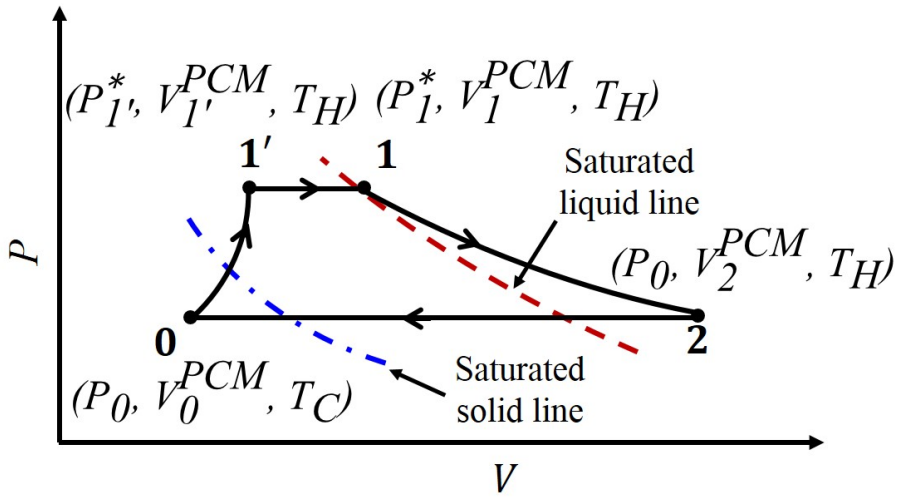

(b) $T_H \leq T_{cm}$

Figure 2.7: The thermodynamic cycle underlying the developed prototype system.

equations

$$v_0^{PCM}(T_H) - \frac{V_1^{PCM}}{m^{PCM}} = C^{PCM}(T_H)\log(1 + \frac{P_1^* - P_0}{B^{PCM}(T_H)}), \tag{2.39}$$

$$v_0^{H}(T_H) - \frac{V_1^{H}}{m^{H}} = C^{H}(T_H)\log(1 + \frac{P_1^* - P_0}{B^{H}(T_H)}), \tag{2.40}$$

$$\frac{P_1^* V_1^{air}}{T_H} = \frac{P_0 V_0^{air}}{T_C}, \tag{2.41}$$

$$(V_1^{PCM} - V_0^{PCM}) + (V_1^{H} - V_0^{H}) + (V_1^{air} - V_0^{air}) = \frac{P_1^* - P_0}{4D\pi^4}\sum_{i=1}^{6}\frac{a_i^5 b_i^5}{3a_i^4 + 2a_i^2 b_i^2 + 3b_i^4}. \tag{2.42}$$

where V_0^{PCM} and V_1^{PCM} denote the volume of the PCM at States 0 and 1, respectively. V_0^{H} and V_1^{H} denote the volume of the hydraulic fluid at States 0 and 1, respectively. V_0^{air} and V_1^{air} denote the volume of the residual air at States 0 and 1, respectively.

The above equations can be solved numerically through Newton–Raphson method. With the solution of P_1^*, the value of T_{cm}^* — that is, the minimum temperature allowing the PCM to fully melt in the deformable prototypical energy harvester — can be calculated according to Eq. (2.5), i.e.

$$T_{cm}^* = kP_1^* + n. \tag{2.43}$$

It can be expected that T_{cm}^* will be smaller than T_{cm}, and its values will increase as the container becomes stiffer.

If $T_H > T_{cm}^*$, the aforementioned assumption that PCM can completely melt is verified, and

the thermodynamic cycle is shown in Fig. 2.7(a). The work done by the PCM is given by

$$\begin{aligned} W^* &= \int_{V_0^{PCM}}^{V_1^{PCM}} (P^*(V) - P_0)dV + \int_{V_1^{PCM}}^{V_2^{PCM}} (P^*(V) - P_0)dV. \\ &= U + W^H + \int_{V_1^{PCM}}^{V_2^{PCM}} (P^*(V) - P_0)dV \\ &= U + W^H + B^{PCM}(T_H)(V_1^{PCM} - \frac{m^{PCM}}{\rho_l^{PCM}} + m^{PCM}\frac{C^{PCM}(T_H)}{\ln 10}10^{\frac{1}{\rho_l^{PCM}C^{PCM}(T_H)} - \frac{V_1^{PCM}}{m^{PCM}(T_H)}} \\ &\quad -m^{PCM}\frac{C^{PCM}(T_H)}{\ln 10}) \end{aligned} \tag{2.44}$$

where ρ_l^{PCM} is the density of liquid PCM at P_0 and T_H. U denotes the strain energy of the elastic container, and is formulated in Eq.(2.34). W^H is the work done by the PCM to the hydraulic fluid, given by

$$\begin{aligned} W^H &= \int_{V_1^H}^{V_2^H} (P^*(V) - P_0)dV \\ &= B^H(T_H)(V_1^H - V_0^H + m^H\frac{C^H(T_H)}{\ln 10}10^{\frac{1}{\rho_l^H C^H(T_H)} - \frac{V_1^H}{m^H C^H(T_H)}} \\ &\quad -m^H\frac{C^H(T_H)}{\ln 10}), \end{aligned} \tag{2.45}$$

where V_2^H is the volume of hydraulic fluid at State 2. ρ_l^H is the density of liquid PCM at P_0 and T_H.

On the other hand, if $T_H \leq T_{cm}^*$, PCM cannot completely melt without an additional isobaric expansion, similar to Proc. 2 in Fig. 2.5(b) for the idealized setting. The thermodynamic

cycle for this scenario is shown in Fig. 2.7(b). In particularly, the pressures at States 1' and 1 are determined according to Eq. (2.5), i.e.

$$P^*_{1'} = P^*_1 = \frac{T_H - n}{k}. \tag{2.46}$$

The work done by the PCM is given as

$$\begin{aligned} W^* &= \int_{V_0^{PCM}}^{V_{1'}^{PCM}} (P^*(V) - P_0)dV + \int_{V_{1'}^{PCM}}^{V_1^{PCM}} (P^*(V) - P_0)dV + \int_{V_1^{PCM}}^{V_2^{PCM}} (P^*(V) - P_0)dV \\ &= U + W^H + (P^*_1 - P_0)(V_1^{PCM} - V_{1'}^{PCM}) \\ &\quad + B^{PCM}(T_H)(V_1^{PCM} - \frac{m^{PCM}}{\rho_l^{PCM}} + m^{PCM}\frac{C^{PCM}(T_H)}{\ln 10}10^{\frac{1}{\rho_l^{PCM}C^{PCM}(T_H)} - \frac{V_1^{PCM}}{m^{PCM}C^{PCM}(T_H)}} \\ &\quad - m^{PCM}\frac{C^{PCM}(T_H)}{\ln 10}) \end{aligned} \tag{2.47}$$

where V_1^{PCM} can be derived using Eq. (3.6), yielding

$$V_1^{PCM} = m^{PCM}\Big(v_0^{PCM} - C^{PCM}(T_H)\log(1 + \frac{P^*_1 - P_0}{B^{PCM}(T_H)})\Big). \tag{2.48}$$

$V_{1'}^{PCM}$ is the volume of PCM at State 1'. It can be derived using Eq. (2.42), which gives

$$\begin{aligned} V_{1'}^{PCM} &= V_0^{PCM} + \Delta V^{Total} - (V_{1'}^H - V_0^H) - (V_{1'}^{air} - V_0^{air}) \\ &= V_0^{PCM} + \sum_{i=1}^{6} \Big(\frac{(P_{1'}^* - P_0)}{4D\pi^4} \frac{a_i^5 b_i^5}{3a_i^4 + 2a_i^2 b_i^2 + 3b_i^4} \Big) \\ &\quad - \Big(m^H \big(v_0^H - C^H(T_H) \log(1 + \frac{P_{1'}^* - P_0}{B^H(T_H)}) \big) - V_0^H \Big) \\ &\quad - (\frac{P_0 V_0^{air} T_H}{P_{1'}^* T_C} - V_0^{air}) \end{aligned} \tag{2.49}$$

Similar to the thermal efficiency in the idealized setting, the thermal efficiency of this prototype can be expressed as

$$\eta_{PCM}^* = \frac{W^*}{\Big(\int_{T_C}^{T_H} c_p(T) dT \Big) m^{PCM} + \Delta H_m m^{PCM} + W^*}. \tag{2.50}$$

Theorem 1. *$\eta_{PCM}^* < \eta_{PCM}$. In other words, the idealized setting proposed in the previous section is indeed more efficient than the developed prototype.*

Proof. We first consider the scenario of $T_H > T_{cm}^*$. For prescribed values of T_C, T_H and m^{PCM}, Eq. (2.50) can be simplified as

$$\eta_{PCM}^*(W^*) = \frac{W^*}{E + W^*}, \tag{2.51}$$

where

$$E = \Big(\int_{T_C}^{T_H} c_p(T) dT \Big) m^{PCM} + \Delta H_m m^{PCM} \tag{2.52}$$

is a constant. In other words, η^*_{PCM} is a monotonically increasing function of W^*. Moreover,

$$\begin{aligned} W^* &= \int_{V_0^{PCM}}^{V_1^{PCM}} (P^*(V) - P_0)dV + \int_{V_1^{PCM}}^{V_2^{PCM}} (P^*(V) - P_0)dV \\ &< \int_{V_0^{PCM}}^{V_1^{PCM}} (P_1^* - P_0)dV + \int_{V_1^{PCM}}^{V_2^{PCM}} (P^*(V) - P_0)dV \\ &< \int_{V_0^{PCM}}^{V_1^{PCM}} (P(V) - P_0)dV + \int_{V_1^{PCM}}^{V_2^{PCM}} (P^*(V) - P_0)dV \\ &= \int_{V_0^{PCM}}^{V_2^{PCM}} (P(V) - P_0)dV \\ &= W. \end{aligned} \tag{2.53}$$

In particular, the second inequality in (2.53) is obtained based on the fact that for any $V \in (V_0^{PCM},\ V_1^{PCM})$, $P(V)$ is greater than $P_1^*(V)$, i.e. the pressure inside the prototype system at State 1 (Fig. 2.7(a)).

Substituting Eq. (2.53) into Eq. (2.51) yields

$$\eta^*_{PCM} < \frac{W}{E+W} = \eta_{PCM}. \tag{2.54}$$

In the scenario of $T_H \leq T^*_{cm}$,

$$\begin{aligned} W^* &= \int_{V_0^{PCM}}^{V_{1'}^{PCM}} (P^*(V) - P_0)dV + \int_{V_{1'}^{PCM}}^{V_1^{PCM}} (P^*(V) - P_0)dV + \int_{V_1^{PCM}}^{V_2^{PCM}} (P^*(V) - P_0)dV \\ &< \int_{V_0^{PCM}}^{V_{1'}^{PCM}} (P^*_{1'} - P_0)dV + \int_{V_{1'}^{PCM}}^{V_1^{PCM}} (P^*(V) - P_0)dV + \int_{V_1^{PCM}}^{V_2^{PCM}} (P^*(V) - P_0)dV \\ &= \int_{V_0^{PCM}}^{V_1^{PCM}} (P(V) - P_0)dV + \int_{V_1^{PCM}}^{V_2^{PCM}} (P(V) - P_0)dV \\ &= W. \end{aligned} \tag{2.55}$$

Substituting Eq. (2.55) into Eq. (2.51) yields

$$\eta^*_{PCM} < \frac{W}{E + W} = \eta_{PCM}. \tag{2.56}$$

2.3 Prototype development and characterization

To validate the thermomechanical model, we fabricate and experimentally characterize a benchtop prototype of the energy harvesting system proposed in the previous section.

Materials and methods

Figure 2.8 shows the PCM and the prototype. The prototype consists of two major components: a pressure vessel and an electromagnetic generator (EMG). The pressure vessel serves as a container for the PCM and a surrounding hydraulic fluid medium. In this experimental

study, water is used as the hydraulic fluid for the ease of operation and cleaning. The vessel is designed to be in the shape of a rectangular box. Its length, width, and height are set to 30 cm, 25 cm, and 10 cm, respectively. All the six faces are made using 5 mm thick 6061-T6 Aluminum plates with Young's modulus $E = 69$ GPa and Poisson's ratio $\nu = 0.33$. They are welded together with silicon aluminum solder powder, with an estimated strength of 51 GPa . A circular window with a diameter of 14 cm is created on the top surface of the vessel. It is mainly designed for inserting and removing PCM, as well as observing the phase change process. A transparent, watertight lid is fabricated using a polycarbonate resin sheet (Lexan 9034) [37]. To make it watertight, an O-ring is used between the lid and vessel. Two steel pipes are connected to the pressure vessel, which are controlled by valves. Pipe A (as shown in Fig. 2.8) is used for adding hydraulic fluid to the vessel. It has a diameter of 19.05 mm (0.75 in.). The other one, pipe B, connects the vessel to the EMG. It has a diameter of 12.7 mm (0.5 in.)— in order to match the diameter of the EMG. In the present work, an off-the-shelf EMG with 12.7 mm PT thread connector,maximum 12 V DC output, and working temperature range $5°\text{C} - 85°\text{C}$ [38] is used. As valve B opens, the pressurized fluid flow goes through the EMG, which allows the generation of electricity.

The PCM used in this work is pentadecane ($C_{15}H_{32}$) [31]. Its melting temperature is $T_m = 10°\text{C}$ at atmospheric pressure. The density of the PCM in the liquid phase (20°C, 1 atm) is $\rho_l^{PCM} = 769$ kg/m^3, and the density in the solid phase (1°C, 1 atm) is $\rho_s^{PCM} = 861$ kg/m^3 . In order to separate the PCM from the working fluid (e.g. hydraulic fluid) and prevent PCM from flowing out of the pressure vessel, the PCM is sealed in vacuumed plastic bags. Two

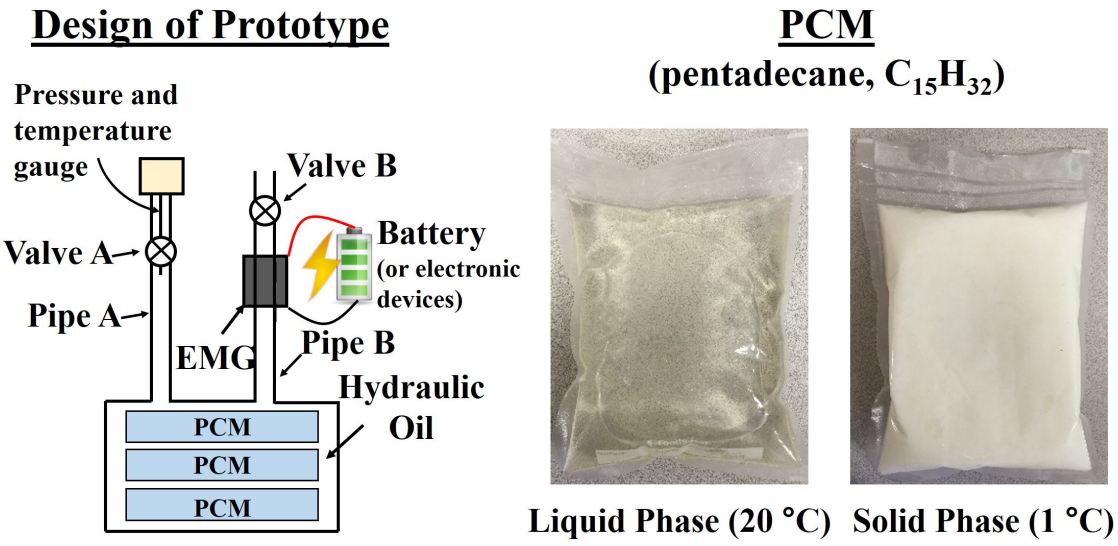

(a) A schematic drawing of the design, and two photos of the PCM.

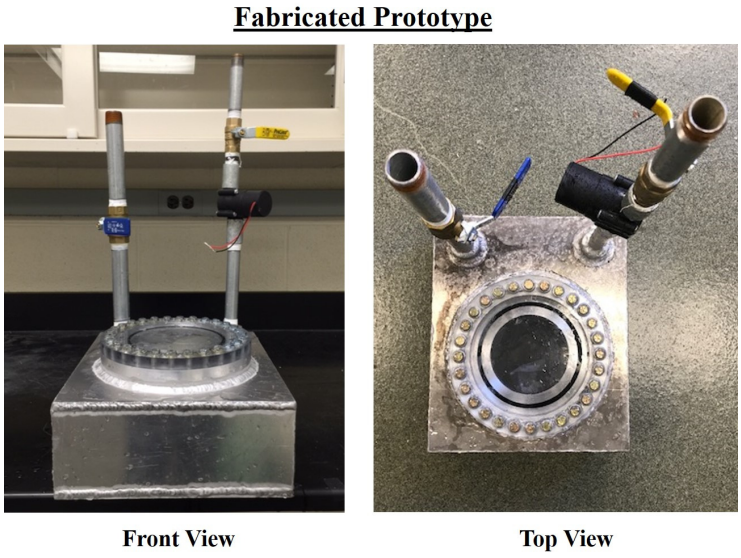

(b) Photos of the fabricated prototype.

Figure 2.8: The proposed prototype system.

heat reservoirs at $T_C = 1°C$ and $T_H = 20°C$ are created using a Midea freezer and a water tank, respectively. The experiment process is as follows.

First, encapsulated liquid PCM (4.5L, 20°C) is inserted in the pressure vessel. The lid is installed and sealed with an O-ring. Then the prototype is placed in the heat reservoir at 1°C for 12 hours to freeze the PCM. After the PCM is completely frozen, the system is moved to the other heat reservoir (20°C) for 12 hours to make the PCM melt and expand. After the melting process, the pressure inside the vessel is measured with a pressure gauge connected to pipe A. Then, valve B is opened to let the pressurized hydraulic fluid drive the EMG and generate electric energy.

To measure the electric energy generated, a load resistor is connected to the EMG through pipe B. A data acquisition (DAQ) board measures the voltage across the load resistor. A LabVIEW program is developed and applied to control the measurement and record the data. The measurement setup is shown in Fig. 2.9. As an example, Fig. 2.10 shows the

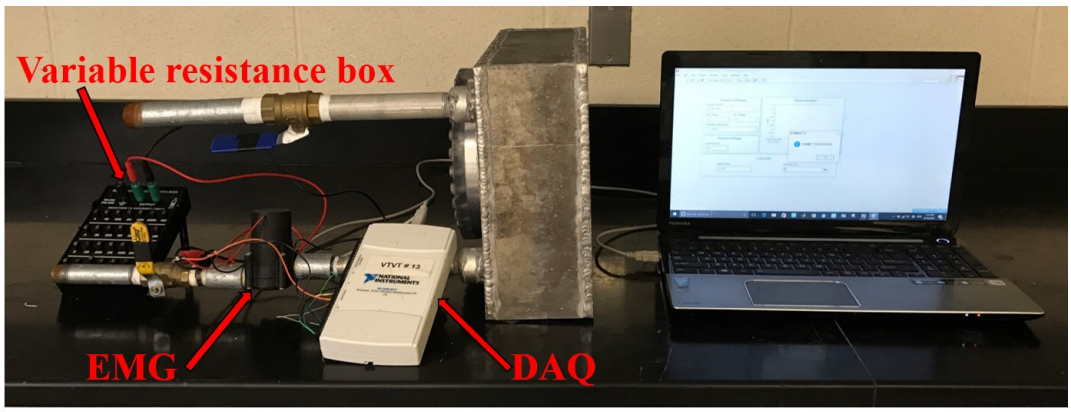

Figure 2.9: Setup of the energy measurement experiment

measured EMG voltage and the instantaneous power with load resistance of 100 Ohm. The

voltage and hence power last for approximately 3 s. Their profiles are of the shape of a parabola, with a peak voltage of 8.85 V and a peak power of 0.79 W.

Experimental result

Right before opening valve B, the pressure inside the vessel is measured with a pressure gauge connected to pipe A. The measurement is repeated three times in three freezing-melting cycles, and the measured pressure value is $P_{exp} = 501 \pm 6$ kPa (total pressure).

It is notable that the voltage and the amount of energy generated are sensitive to the load resistance. To investigate the effect of the load resistance and to increase the amount of energy delivered to the load, adifferent load resistances, including 10 Ohm, 25 Ohm, 50 Ohm, 100 Ohm, 150 Ohm, 200 Ohm, 250 Ohm and 400 Ohm, are tested, while other experiment parameters remain unchanged. Figure 2.11 shows the relationship between the amount of energy generated versus the load resistance. It is observed that the maximum energy of 0.36 J is achieved with the load resistance of 100 Ohm. The amount energy generated under the load resistance of 100 Ohm increases by 250%, compared with that of the load resistance 10 Ohm.

It is observed the wake flow downstream of the EMG still has high velocity, hence high kinetic energy. This suggests that the amount of energy generated could be increased by either applying a customized EMG with multiple gears, which can harvest more kinetic

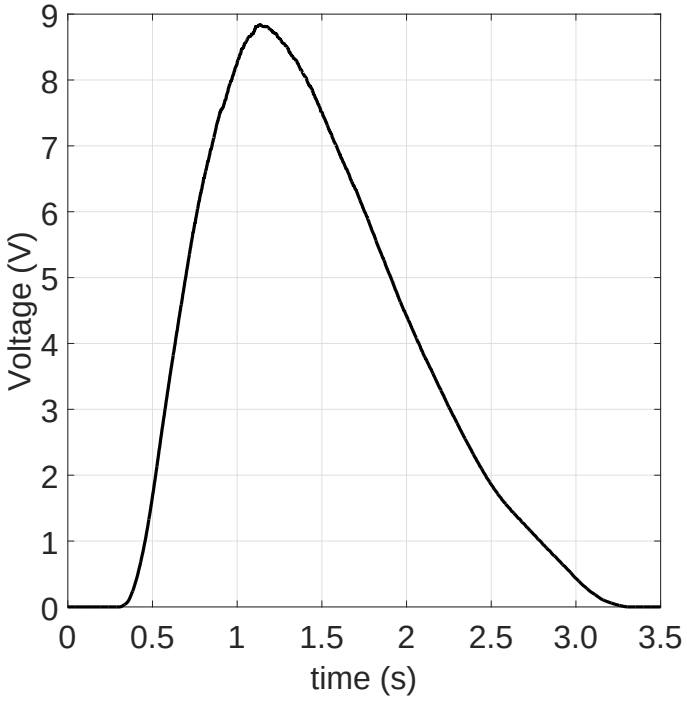

(a) EMG voltage with the load resistance of 100 Ohm

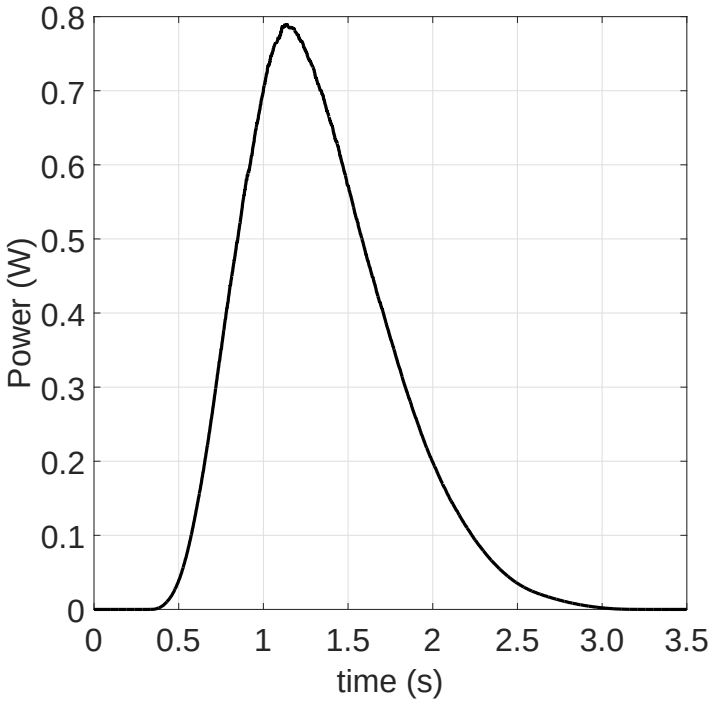

(b) Output power with the load resistance of 100 Ohm

Figure 2.10: EMG voltage and power with the load resistance of 100 Ohm

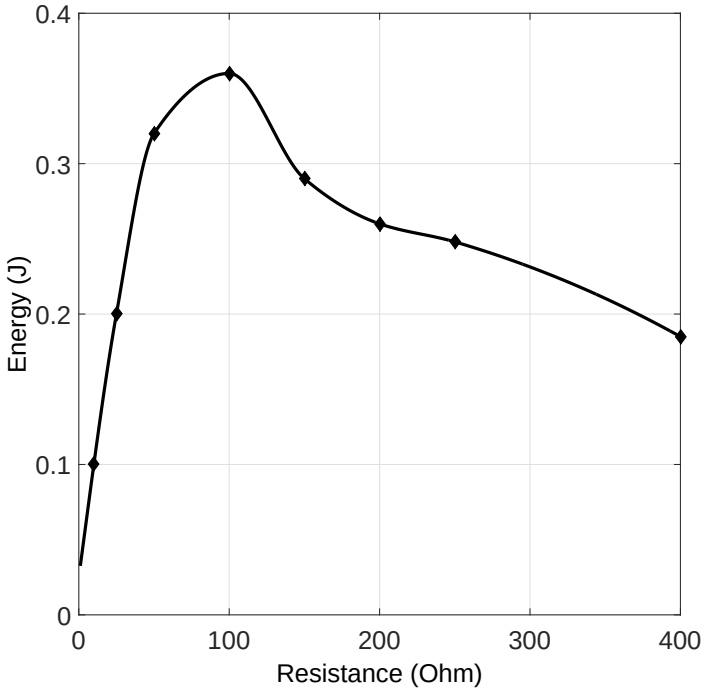

Figure 2.11: Energy generated versus load resistance (Piecewise cubic hermite interpolating polynomials are used to fit the experimental measurements)

energy of the fluid flow, or applying multiple EMGs in series. In this work, three EMGs with the load resistance 100 Ohm for each EMG are connected in series to increase the total amount of energy generated (Fig. 2.12). The experimental result of three series EMGs is shown in Fig. 2.13. The energy generated for individual EMGs is 0.31 J, 0.27 J and 0.16 J. The total amount of energy generated with three series EMGs is 0.74J, which is larger than that for a single EMG by a factor of 106%.

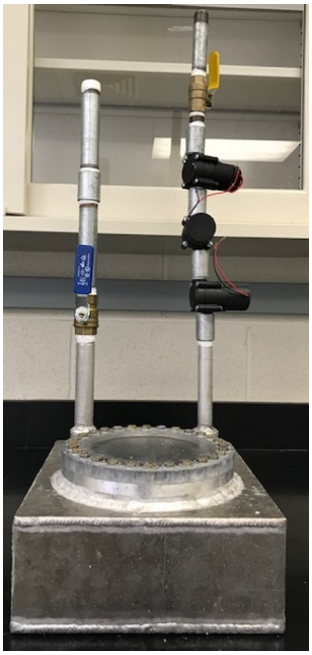

Figure 2.12: Measurement setup for three EMGs connected sequentially

To evaluate the repeatability of the energy harvesting process, measurement is repeated for five times with the load resistance of 100 Ohm. For all the measurements, the experiment conditions remain the same. The individual energy generated for the five measurements are 0.36 J, 0.34 J, 0.35 J, 0.37 J, and 0.35 J. The maximum deviation from the average value is only 4.5%.

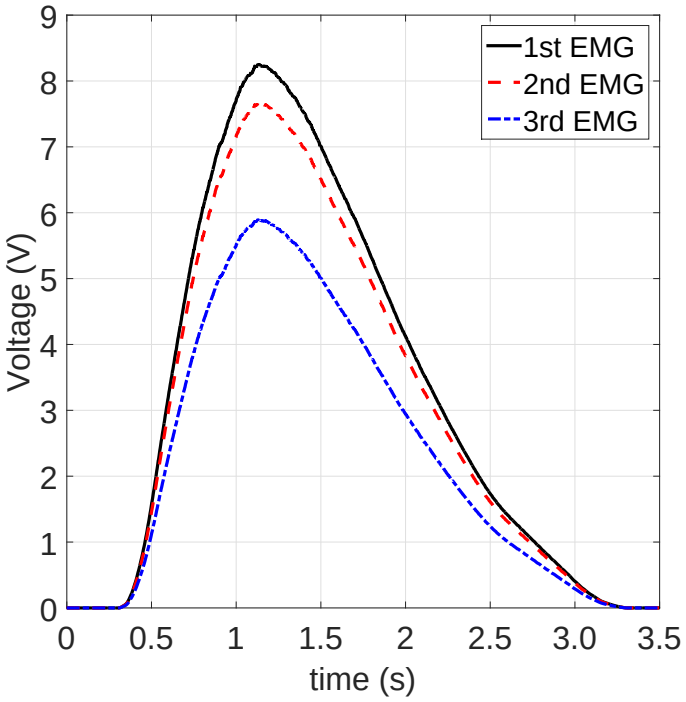

(a) Voltages of the three serial EMGs

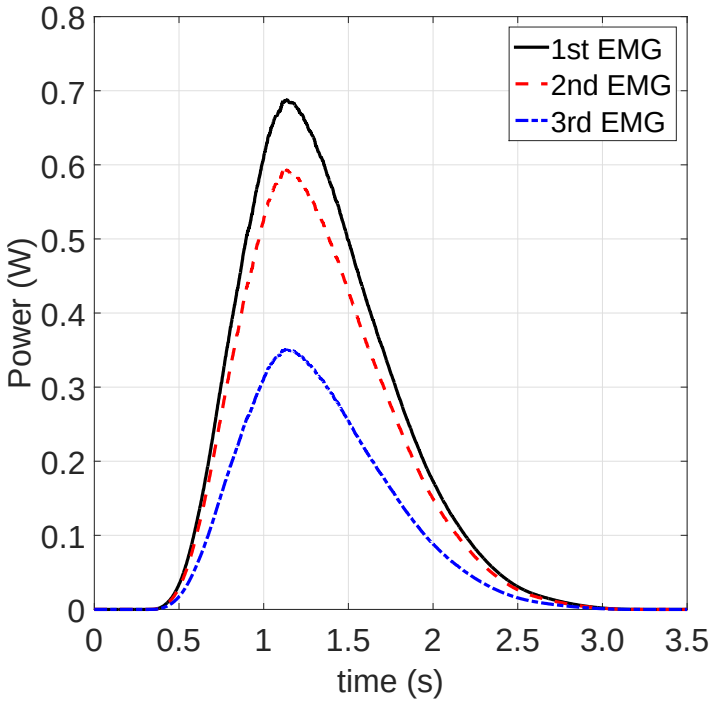

(b) Power of the three serial EMGs

Figure 2.13: Voltage and power of three serial EMGs with the load resistance of 100 Ohm for each EMG

2.4 Model validation and parameter studies

Model validation

We validate the thermomechanical model using the developed benchtop prototype system. The parameters of the thermomechanical model are set to be identical to those in the experiment, in order to predict the performance of the developed prototype and validate the thermomechanical model. The values of the input parameters are shown in Tab. 3.2.

Table 2.1: Input parameters

Parameters	Values
v_0^{PCM}	0.0013 m^3/kg
V_0^{PCM}	4.0178×10^{-3} m^3
m^{PCM}	3.4605 kg
v_0^H	0.0010 m^3/kg
V_0^H	3.4743×10^{-3} m^3
m^H	3.4743 kg
P_0	101 kPa
V_0^{air}	3.7363×10^{-4} m^3
D	696 $N \cdot m$
ρ_l^{PCM}	769 kg/m^3
ρ_s^{PCM}	861 kg/m^3

The results corresponding to State 1 of Fig. 2.7(a) are provided in Tab. 2.2. Based on the model, the pressure inside the prototype after the melting process is $P_1^* = 523.14$ kPa. The measured pressure in the experiment is $P_{exp} = 501$ kPa. The pressure difference between the physical model and experiment measurement is 4.42%, which is an acceptable discrepancy.

In addition, the corresponding T_{cm}^* under P_1^* is 10.08°C and $T_H > T_{cm}^*$. Therefore, the total

Table 2.2: Solution of State 1

Parameters	Values
V_1^{PCM}	$4.4984 \times 10^{-3}\text{m}^3$
V_1^{H}	$3.4736 \times 10^{-3}\text{m}^3$
V_1^{Air}	$7.1940 \times 10^{-5}\text{m}^3$
P_1^*	523.14 kPa

work done by PCM can be calculated according to Eq.(2.44), i.e.

$$\begin{aligned} W^* &= U + W^H + \int_{V_1^{PCM}}^{V_2^{PCM}} (P - P_0) dV \\ &= 34.12 \text{ J} \end{aligned} \tag{2.57}$$

Parameter study

The thermomechanical model can be used as a design tool to predict the performance of energy harvesting systems with different PCMs and structural designs. In addition to the thermal efficiency (η_{PCM}^*), the specific mechanical energy output is also an important metric of merit, which can be defined as

$$w^* = \frac{W^*}{m^{PCM} + m^H + m^S}, \tag{2.58}$$

where m^S is the mass of the structure of the energy harvesting system.

Tait EOS has been applied to model a large number of PCMs in their liquid phase [29, 28]. Therefore, we use its model parameters, i.e. B and C, together with the solid-liquid density

ratio

$$r = \frac{\rho_{\mathrm{s}}^{\mathrm{PCM}}}{\rho_{\mathrm{l}}^{\mathrm{PCM}}} \tag{2.59}$$

to characterize each PCM.

Figure 2.14 shows the effect of r on η^*_{PCM} and w^*. Evidently, both η^*_{PCM} and w^* increase superlinearly with r. This suggests that a small increase in r may lead to a significant performance improvement in terms of both η^*_{PCM} and w^*. Specifically, for the PCM in our prototype (i.e. $C_{15}H_{32}$), $r = 1.12$. Figure 2.14 suggests that if r can be increased by 25% to 1.4, both η^*_{PCM} and w^* will increase by 10 times.

Figure 2.15 presents the dependence of η^*_{PCM} and w^* on the parameters B and C in Tait EOS (at $T_H = 20°\mathrm{C}$) , where $B_0 = 108.91$ MPa and $C_0 = 2.68 \times 10^{-4}$ m^3/kg correspond to $C_{15}H_{32}$. Evidently, both η^*_{PCM} and w^* are monotonically increasing functions of B/B_0, and monotonically decreasing functions of C/C_0. Moreover, the figure also identifies $\{0 < B/B_0 < 1,\ C/C_0 > 1\}$ as a subspace of the design space where the effects of B and C are significant. For example, when B/B_0 is increased from 0.15 to 0.2 and C/C_0 is decreased from 5 to 4, both η^*_{PCM} and w^* will increase by 40%.

Table 2.3: Comparison of different phase change materials (PCM)

PCMs	T_m(°C)	ρ_s(kg/m^3)	ρ_l(kg/m^3)	B(MPa)	C(m^3/kg)	η_{PCM}(%)
Dodecane ($C_{12}H_{26}$)	−5.5	863	736	106.12	2.79×10^{-4}	4.36
Tetradecane ($C_{14}H_{30}$)	5.5	884	758	104.68	2.72×10^{-4}	3.25
Pentadecane ($C_{15}H_{32}$)	10	861	769	108.91	2.68×10^{-4}	2.45
Hexadecane ($C_{16}H_{34}$)	18	864	773	102.12	2.66×10^{-4}	2.05
Octadecane ($C_{18}H_{38}$)	28	855	777	101.25	2.65×10^{-4}	1.35

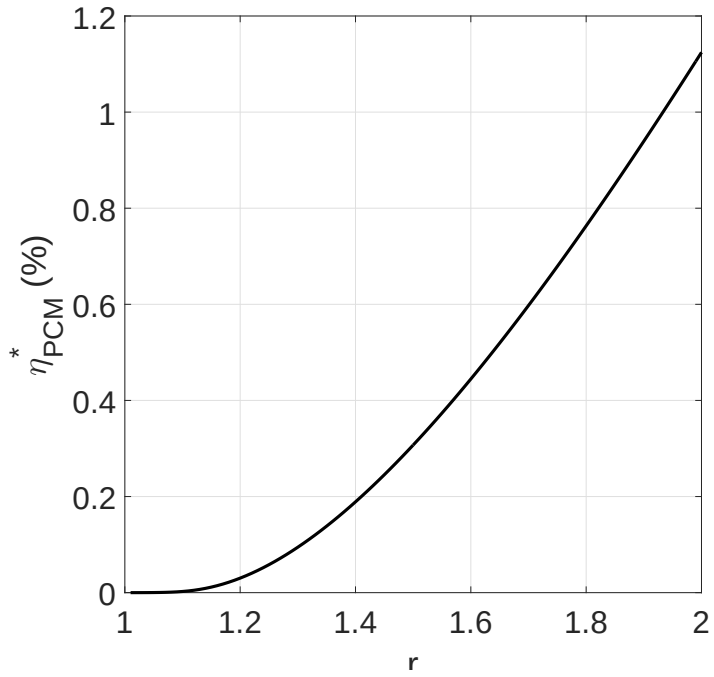

(a) Effect of r on the thermal efficiency (η^*_{PCM})

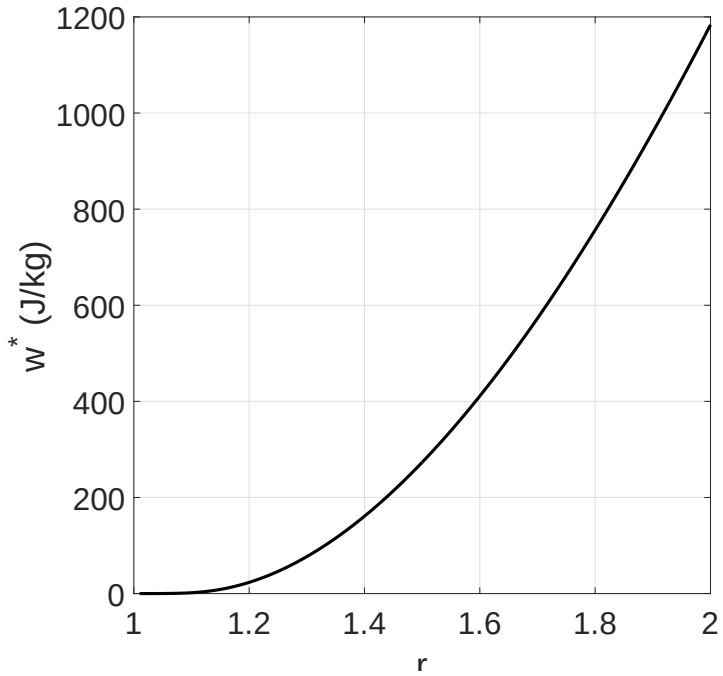

(b) Effect of r on the specific mechanical energy (w^*)

Figure 2.14: Effects of the solid-liquid density ratio (r) of the PCM on the thermal efficiency (η^*_{PCM}) and the specific mechanical energy (w^*).

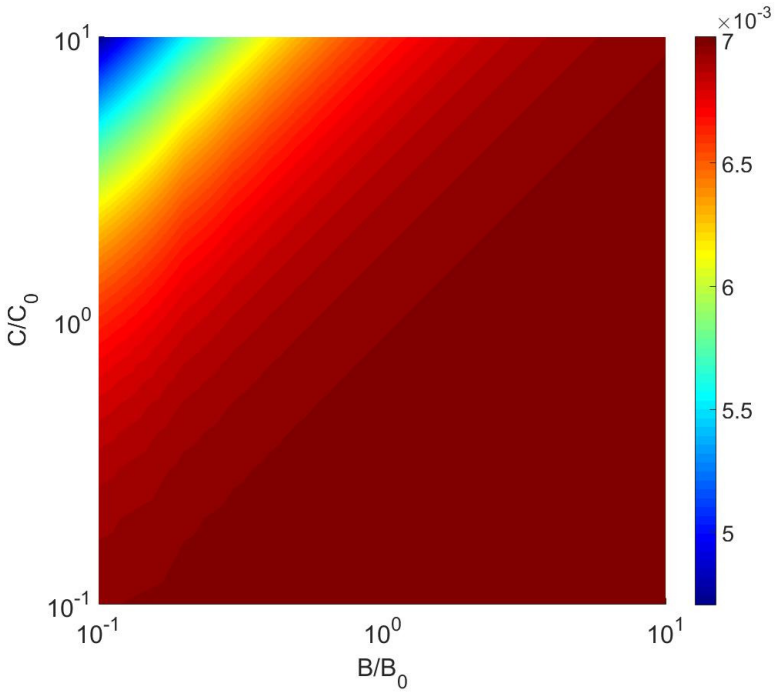

(a) Effect of B and C on η^*_{PCM}

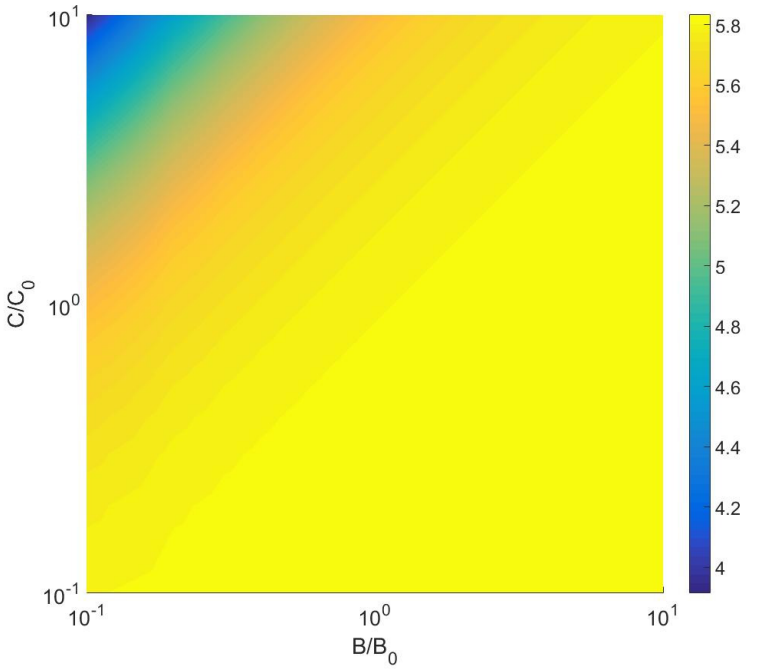

(b) Effect of B and C on w^*

Figure 2.15: Effects of model parameters B and C on the thermal efficiency (η^*_{PCM}) and the specific mechanical energy (w^*).

In addition, Tab. 2.3 compares the thermal efficiency of several specific PCMs using the thermodynamic model developed in this work. These materials have a melting temperature between $-10°$C and $30°$C, therefore can potentially be applied to harvest environmental thermal energy in various scenarios. The Tait EOS parameters for these materials are obtained from Cutler *et al.* [29], Wang *et al.* [39] and Kumano *et al.* [40]. T_H and T_C are set to be $T_m + 10°$C and $T_m - 9°$C, respectively, where T_m denotes the melting temperature of the material. The result shows that the thermal efficiency of different PCMs vary significantly. Among the compared PCM, dodecane ($C_{12}H_{26}$) has the highest efficiency, which is 4.36%.

The structural design of the proposed prototype can be characterized by two parameters, namely the flexural rigidity of the rectangular container (D) and the volume of PCM inside the container (V_0^{PCM}).

Figure 2.16 presents the dependence of η^*_{PCM} and w^* on D and V_0^{PCM}. Both parameters are nondimensionalized, using the flexural rigidity of the fabricated prototype (D_0) and the total inner volume of the container (V^{Total}), respectively. Clearly, both η^*_{PCM} and w^* increase with V_0^{PCM}, especially when $D/D_0 > 50$. When $V_0^{PCM}/V^{Total} < 0.45$, the effect of D on the performance of the system is not very significant. However, when $V_0^{PCM}/V^{Total} > 0.45$, both η^*_{PCM} and w^* increase with D and tend to be constant when D/D_0 exceeds 600. For example, when $D/D_0 = 1000$ and $V_0^{PCM}/V^{Total} = 0.9$ (i.e., the system approaches the idealized setting), η^*_{PCM} increases to 1.2%, which is much closer to η_{PCM} than the current setting.

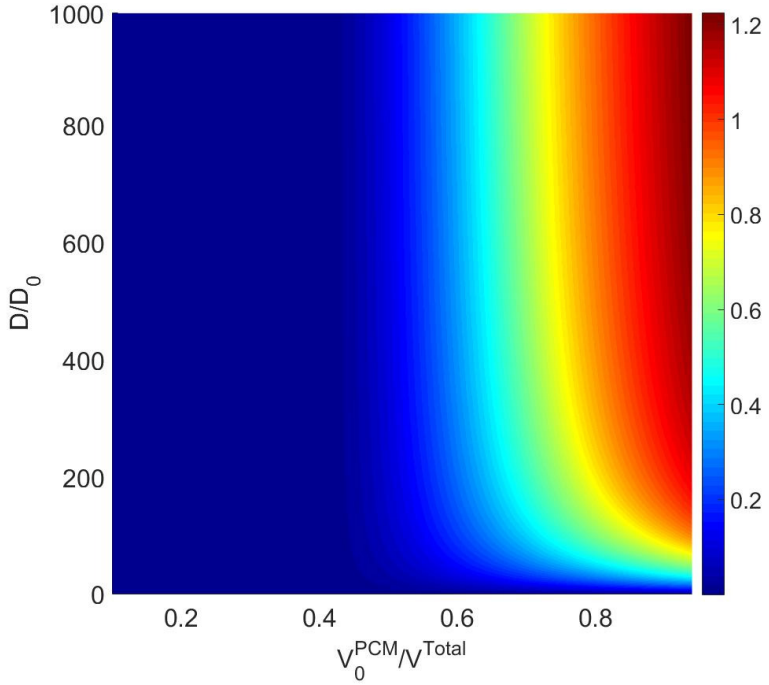

(a) Dependence of η^*_{PCM} on D and V_0^{PCM}

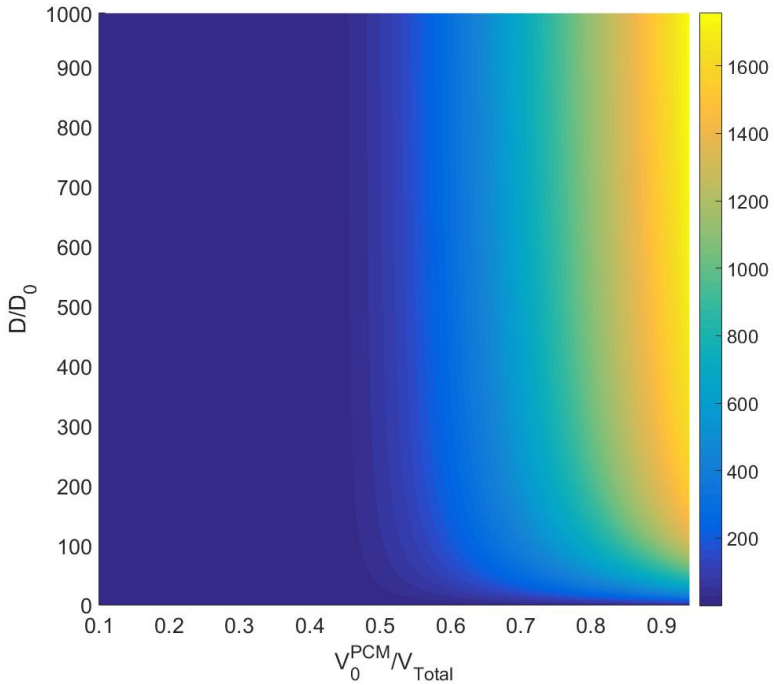

(b) Dependence of w^* on D and V_0^{PCM}

Figure 2.16: Dependence of η^*_{PCM} and w^* on D and V_0^{PCM}

2.5 Conclusion

This paper presents a combined theoretical and experimental study that aims to investigate the feasibility of using solid/liquid phase change materials (PCM) to harvest environmental thermal energy associated with small temperature differentials. The basic idea is to cyclically melt and freeze the PCM within the temperature differential, and convert a fraction of the thermal energy it absorbed during the melting process into mechanical or electrical energy.

In this work, we first develop a thermodynamic model for an idealized setting, in which the PCM is assumed to be placed in a rigid structural container. Therefore, it undergoes an isochoric melting process. In this model, we apply an experimentally validated Tait equation of state (EOS) to model the PCM in its liquid phase. Based on this model, we derive an upperbound of the thermal efficiency that can be achieved using a PCM, and compare it with both the well-known Carnot efficiency and the optimal efficiency of state-of-the-art thermoelectric generators (TEGs). Our result suggests that the thermal efficiency of PCM can be higher than that of Bi_2Te_3 TEGs when the temperature differential is less than 100°C. Next, we propose a prototypical PCM-based energy harvester that stores the PCM in an elastic rectangular container. To predict the performance of this prototype, we develop a thermomechanical model that couples the aforementioned thermodynamic model with the Kirchoff-Love plate theory. To validate the model and demonstrate the underlying idea, we fabricate the prototype using pentadecane ($C_{15}H_{32}$) as the PCM, and an electromagnetic generator (EMG) to generate electricity. To characterize its performance, we measure the

pressure of PCM and the power output of the EMG. A satisfactory agreement is obtained between the experiment and the model for the pressure of PCM after melting. Finally, we use the thermomechanical model to conduct a series of parameter studies. Overall, our result shows that the performance of a PCM-based thermal energy harvester depends sensitively on both the material properties of the PCM (e.g., the solid/liquid density ratio) and the structural design. In particular, the optimal performance of five PCMs with a melting temperature between $-10°C$ and $30°C$ are estimated and compared, which provides a preliminary guidance for future designs.

Acknowledgment

G.W., D.H. and K.G.W. acknowledge funding from the Institute for Critical Technologies and Applied Sciences (ICTAS) at Virginia Tech. K.G.W. also acknowledges a summer faculty fellowship from the US Air Force Office of Scientific Research (AFOSR). The authors thank Drs. Yi Chao and Thomas Curtin for his guidance on the design of this study, and Ning Liu for his assistance on testing the prototype system.

Bibliography

[1] A. Khaligh, O. Onar, Energy harvesting: solar, wind, and ocean energy conversion systems 2009 (2014).

[2] Z. Wan, Y. Tan, C. Yuen, Review on energy harvesting and energy management for sustainable wireless sensor networks, in: Communication Technology (ICCT), 2011 IEEE 13th International Conference on, IEEE, 2011, pp. 362–367.

[3] M. Z. Jacobson, M. A. Delucchi, Providing all global energy with wind, water, and solar power, part i: Technologies, energy resources, quantities and areas of infrastructure, and materials, Energy policy 39 (3) (2011) 1154–1169.

[4] O. Ellabban, H. Abu-Rub, F. Blaabjerg, Renewable energy resources: Current status, future prospects and their enabling technology, Renewable and Sustainable Energy Reviews 39 (2014) 748–764.

[5] E. Minazara, D. Vasic, F. Costa, Piezoelectric generator harvesting bike vibrations energy to supply portable devices, in: Proceedings of International Conference on Renewable Energies and Power Quality (ICREPQ'08), Santander, Spain, 2008, pp. 12–14.

[6] Q. Brogan, T. O'Connor, D. S. Ha, Solar and thermal energy harvesting with a wearable

jacket, in: Circuits and Systems (ISCAS), 2014 IEEE International Symposium on, IEEE, 2014, pp. 1412–1415.

[7] K. Cook-Chennault, N. Thambi, A. Sastry, Powering mems portable devices—a review of non-regenerative and regenerative power supply systems with special emphasis on piezoelectric energy harvesting systems, Smart Materials and Structures 17 (4) (2008) 043001.

[8] T. N. Woods, G. J. Rottman, J. W. Harder, G. M. Lawrence, W. E. McClintock, G. A. Kopp, C. Pankratz, Overview of the eos sorce mission, in: International Symposium on Optical Science and Technology, International Society for Optics and Photonics, 2000, pp. 192–203.

[9] F. K. Lutgens, E. J. Tarbuck, D. Tasa, Essentials of geology, Pearson new international edition, 2014.

[10] L. P. Muffler, Assessment of geothermal resources of the united states, 1978, Tech. rep., Geological Survey, Reston, VA (USA). Geologic Div. (1979).

[11] D. R. Easterling, B. Horton, P. D. Jones, T. C. Peterson, T. R. Karl, D. E. Parker, M. J. Salinger, V. Razuvayev, N. Plummer, P. Jamason, et al., Maximum and minimum temperature trends for the globe, Science 277 (5324) (1997) 364–367.

[12] D. M. Livingstone, A. F. Lotter, I. R. Walker, The decrease in summer surface water temperature with altitude in swiss alpine lakes: a comparison with air temperature lapse rates, Arctic, Antarctic, and Alpine Research (1999) 341–352.

[13] S. M. Masutani, P. K. Takahashi, Ocean thermal energy conversion, Wiley Encyclopedia of Electrical and Electronics Engineering.

[14] K. A. Finney, Ocean thermal energy conversion, Guelph Engineering Journal 1 (2008) 17–23.

[15] F. Balestra, Beyond CMOS Nanodevices 1, John Wiley & Sons, 2014.

[16] J. Chen, L. Zuo, Y. Wu, J. Klein, Modeling, experiments and optimization of an on-pipe thermoelectric generator, Energy Conversion and Management 122 (2016) 298–309.

[17] Makai Ocean Engineering, Makai connects world's largest ocean thermal plant to u.s. grid, [Online; accessed 13-April-2017] (2015).
URL https://www.makai.com/makai-news/2015_08_29_makai_connects_otec/

[18] A. Etemadi, A. Emdadi, O. AsefAfshar, Y. Emami, Electricity generation by the ocean thermal energy, Energy Procedia 12 (2011) 936–943.

[19] G. Ford, C. Niblett, L. Walker, Ocean thermal-energy conversion, IEE Proceedings A-Physical Science, Measurement and Instrumentation, Management and Education-Reviews 130 (2) (1983) 93.

[20] J. A. Jones, Y. Chao, T. I. Valdez, Phase change material thermal power generator, uS Patent 7,987,674 (Aug. 2 2011).

[21] J. A. Jones, Y. Chao, T. I. Valdez, Phase change material thermal power generator, uS Patent 8,689,556 (Apr. 8 2014).

[22] A. M. Khudhair, M. M. Farid, A review on energy conservation in building applications with thermal storage by latent heat using phase change materials, Energy conversion and management 45 (2) (2004) 263–275.

[23] W. Scaife, C. Lyons, Dielectric behaviour of freezing n-decane and n-pentadecane, The Journal of Chemical Thermodynamics 17 (7) (1985) 623–634.

[24] Jet Propulsion Lab, Nasa demonstrates novel ocean-powered underwater vehicle (2010). URL https://www.jpl.nasa.gov/news/news.php?release=2010-111

[25] A. Khaligh, P. Zeng, C. Zheng, Kinetic energy harvesting using piezoelectric and electromagnetic technologies—state of the art, IEEE Transactions on Industrial Electronics 57 (3) (2010) 850–860.

[26] J. Dymond, R. Malhotra, The tait equation: 100 years on, International journal of thermophysics 9 (6) (1988) 941–951.

[27] Y. Li, Equation of state of water and sea water, Journal of Geophysical Research 72 (10).

[28] L. Mansker, A. Criser, A. Jangkamolkulchai, K. Luks, The isothermal compressibility of n-paraffin liquids at low pressures, Chemical engineering communications 57 (1-6) (1987) 87–93.

[29] W. Cutler, R. McMickle, W. Webb, R. Schiessler, Study of the compressions of several high molecular weight hydrocarbons, The Journal of Chemical Physics 29 (4) (1958) 727–740.

[30] J.-L. Daridon, H. Carrier, B. Lagourette, Pressure dependence of the thermophysical properties of n-pentadecane and n-heptadecane, International Journal of Thermophysics 23 (3) (2002) 697–708.

[31] C. Vélez, J. M. O. de Zárate, M. Khayet, Thermal properties of n-pentadecane, n-heptadecane and n-nonadecane in the solid/liquid phase change region, International Journal of Thermal Sciences 94 (2015) 139–146.

[32] M. Milhet, J. Pauly, J. Coutinho, M. Dirand, J.-L. Daridon, Liquid–solid equilibria under high pressure of tetradecane+ pentadecane and tetradecane+ hexadecane binary systems, Fluid Phase Equilibria 235 (2) (2005) 173–181.

[33] S. D. Sharma, H. Kitano, K. Sagara, Phase change materials for low temperature solar thermal applications, Res. Rep. Fac. Eng. Mie Univ 29 (1).

[34] G. J. Snyder, Small thermoelectric generators, The Electrochemical Society Interface 17 (3) (2008) 54.

[35] S. P. Timoshenko, S. Woinowsky-Krieger, Theory of plates and shells, McGraw-hill, 1959.

[36] I. S. Sokolnikoff, R. D. Specht, et al., Mathematical theory of elasticity, Vol. 83, McGraw-Hill New York, 1956.

[37] Lexan 9034 sheet, [Online; accessed 13-April-2017] (2008).

URL http://www.usplastic.com/catalog/files/specsheets/LExan%209034%20-%20Sabic.pdf/

[38] 3/8"pt thread micro-hydro water flow generator hydroelectric charger, http://www.uxcell.com/ (2015).

[39] H.-M. Wang, J.-Y. Wu, C.-Y. Chen, T.-L. Chen, Recovery of acinetobacter radioresistens lipase by hydrophobic adsorption to n-hexadecane coated on nonwoven fabric, Biotechnology progress 19 (2) (2003) 464–468.

[40] H. Kumano, A. Saito, S. Okawa, K. Takeda, A. Okuda, Study of direct contact melting with hydrocarbon mixtures as the pcm, International journal of heat and mass transfer 48 (15) (2005) 3212–3220.

Chapter 3

A Scalable Environmental Thermal Energy Harvester Based on Solid/Liquid Phase-Change Materials

(Accepted for publication in *Applied Energy*)

G. Wang [a], D. S. Ha [b], K. G. Wang [a]

[a] Department of Aerospace and Ocean Engineering, Virginia Polytechnic Institute and State University, Blacksburg, VA 24061, United States

[b] Department of Electrical and Computer Engineering, Virginia Polytechnic Institute and State University, Blacksburg, VA 24061, United States

Under Dr. Kevin Wang's supervision, I contributed all the contents in this chapter.

Abstract

This paper presents the design and analysis of a scalable energy harvesting system that uses a solid/liquid phase change material (PCM), namely pentadecane ($C_{15}H_{32}$), to harvest environmental thermal energy associated with relatively low temperature and small temperature variation. The basic idea is to utilize the volume expansion of the PCM in the phase transition process to do work and generate electricity, which may be particularly suitable for powering sensors and small-scale devices that are designed to carry out long-term missions in an environment that undergoes regular, cyclic temperature variation in space or time. In this paper, we first present the fabrication and testing of a small-scale prototype in the form of a tube system, as well as the development of a thermo-mechanical model that couples the thermodynamics of the involved PCM and fluid materials with the elastic deformation of the structure. Using both the prototype and the model, we show that achieving high performance requires maintaining a high pressure inside the system, which complicates structural design and leads to incomplete melting of PCM. Towards mitigating this critical issue, we propose the idea of using a hydraulic accumulator to regulate the internal pressure. To examine this approach, we add a piston-type hydraulic accumulator to the prototype, and modify the thermo-mechanical model accordingly. We show that the hydraulic accumulator leads to a one-fold increase in both thermal efficiency and specific energy output. In particular, the thermal efficiency obtained by the prototype is comparable with state-of-the-art thermoelectric generators when operating between 1 and 20°C. Using the thermo-mechanical model, we also present a parametric study that shows the dependence of the system's performance

on a few key design parameters.

Keywords

renewable energy, energy harvesting, phase change materials, thermodynamics, thermo-mechanical analysis

3.1 Introduction

Renewable thermal energy is widely available in the natural environment. In many cases, the energy source is associated with relatively small temperature differential (e.g., less than 40°C). For example, it is estimated that the ocean thermocline stores 10^{17} MJ of energy associated with the vertical temperature variation [1]. In tropical and low latitude regions, the water temperature varies by $10 - 20$°C from ocean surface to hundreds of meters in depth [2]. In polar and high latitude regions, the air-water temperature difference at ocean surface can also exceed 10°C [3]. Another case in point is the diurnal temperature variation on the Earth's surface, which can exceed 20°C in high altitude and low humidity regions [4]. In this work, we use the term *environmental thermal energy* to refer collectively to these and other thermal energy resources in the natural environment that are easily accessible, abundant (in terms of total amount), renewable, yet associated with relatively low temperature (e.g., less than 50°C) and small temperature differential.

So far, harvesting of environmental thermal energy has not been extensively explored, largely due to the inherent low energy conversion efficiency. Indeed, for a temperature variation between 1 and 20°C, the theoretical limit given by the Carnot cycle — which is much higher than the efficiency of practical thermomechanical and thermoelectric processes — is only 6.5%. In this regard, the only application that has contributed to the base-load power supply in a few places of the world is the ocean thermal energy conversion (OTEC) technology, which operates by pumping deep cold water to the ocean surface to run a heat engine based on the Rankine cycle [5, 6, 7].

Nonetheless, if harvested using small-scale, portable devices, environmental thermal energy can be used to power sensors and unmanned vehicles that are designed to conduct long-term missions within the environmental temperature differential. When other energy sources (e.g., solar, wind) are unavailable or unpredictable (e.g., within the interior of the ocean), this can be a unique approach for extending the service life and range of the device.

In this work, we investigate the use of solid/liquid phase-change materials (PCM) to develop scalable and efficient environmental thermal energy harvesters. PCM describes a class of materials with high latent heat of fusion and tunable melting temperature; many of which are also nontoxic and chemically stable [8]. For example, paraffins (C_nH_{2n+2}) have a latent heat above 200 J/g, while the melting temperature (at atmospheric pressure) varies between 5.5 and 75.9°C for $14 \leq n \leq 34$ [9]. In the past few decades, PCM have been widely used in research and practice for thermal management, such as solar thermal energy storage [10, 11], building cooling and heating [12, 13] and temperature sensitive packaging [14, 15]. Recently,

a few teams have also explored the feasibility of using PCM to harvest environmental thermal energy (e.g., [16, 17, 18, 19, 20, 21, 22]). The basic idea is to select a PCM with melting temperature within the range of the specific environmental temperature variation. Therefore, as temperature changes (in space or time), the PCM cyclically undergoes solid/liquid phase transition. When it melts, the associated volume expansion can be used to do useful work (e.g., by driving a small-scale hydroelectric generator), thereby converting a fraction of the adsorbed thermal energy into electricity (Figure 3.1). For example, Jones, Chao and Valdez described this approach in two patents in 2011 and 2014 [16, 17]. Chao presented a compact PCM-based ocean thermal energy harvesting and storage system, which can continuously provide power for a float known as Sounding Oceanographic Lagrangian Observer (SOLO) for 1.5 years [18]. Ma, Wang, Wang and Yang developed a PCM (hexadecane)-based thermal engine, which is able to drive the buoyancy-driven system of an underwater glider for 29 days, completing 121 working profiles [20, 21]. These efforts have focused primarily on describing this approach and demonstrating its potential impact to specific application domains. To investigate the fundamental energy conversion mechanism, Wang, Ha and Wang developed a thermomechanical model for a box-shaped prototype that uses pentadecane ($C_{15}H_{32}$), and predicted that the theoretical upper limit of thermal efficiency is approximately 2.5% for temperature variation between 1 and 20°C, assuming a rigid structural system [22].

In this paper, we start with presenting the design of a new, scalable PCM-based energy harvester that is in the form of a tube system. Compared with existing harvesters shown in the public domain, this design allows power output to be increased or decreased simply

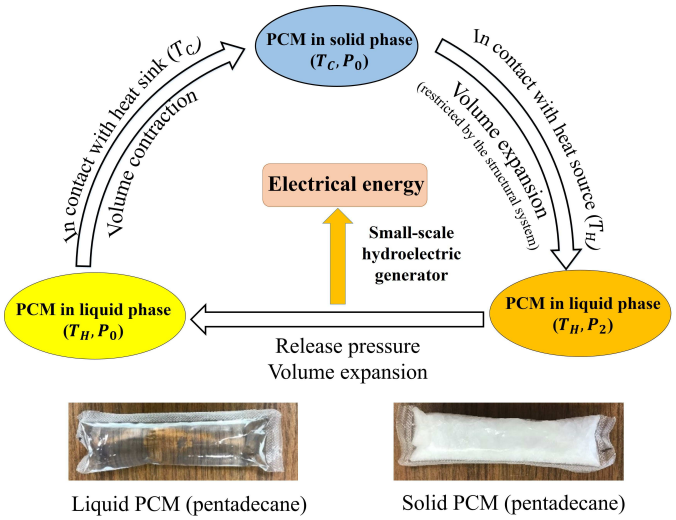

Figure 3.1: Mechanism of PCM-based energy harvesting. T_C and T_H refer to the temperature of the cold and hot thermal reservoirs, respectively. P_0 denotes the ambient pressure. P_2 ($> P_0$) represents the pressure within melted PCM.

by changing the length and/or diameter of the main tube. A prototype is fabricated and tested in a laboratory environment. In particular, to characterize the system, both the peak pressure achieved within the system and the electrical energy output are measured. Furthermore, a thermomechanical model that accounts for the thermodynamic behaviors of the fluid materials and the deformation of the structural system is developed and validated using the experimental data. Combining the fabricated prototype and the thermomechanical model, we reveal a critical issue that has not been discussed in detail, that is, achieving high thermal efficiency typically requires maintaining a very high pressure (e.g., above 100 MPa) within the device. This issue leads to a formidable challenge to structural design. It also prevents the PCM from complete melting — as pressure increases, the material's melting temperature will also increase, eventually exceed the environmental temperature range. To mitigate this issue, we investigate the use of hydraulic accumulators to regulate the peak

pressure within the device. In this regard, we add a piston type hydraulic accumulator to both the prototype device and the thermomechanical model, thereby presenting a combined experimental and theoretical analysis on the effects of the hydraulic accumulator on thermal efficiency and specific energy output. Finally, we briefly discuss the potential use of small-scale, PCM-based energy harvesters, including the sensors and devices they can power.

3.2 Design of a scalable PCM-based energy harvesting system

Figure 3.2(a) presents a schematic drawing of the designed thermal energy harvesting system. The system features the use of a cylindrical tube to house encapsulated PCM packages, which are immersed in a hydraulic fluid. It can be assembled using standard materials and components without the need of welding; and the power output can be easily scaled by varying the dimensions of the tube and the amount of the PCM. More specifically, the horizontal tube serves as the container of PCM and hydraulic fluid. The two narrower, vertical tubes are used to fill the horizontal tube with hydraulic fluid (Tube A) and to connect the horizontal tube to the DC water turbine generator (Tube B).

Let T_H and T_C denote, respectively, the temperature of the heat source and sink of an environmental thermal energy resource. The PCM should have a melting temperature T_m between T_H and T_C at ambient pressure. To harvest energy, the system is cyclically moved

between the heat source and sink. As the PCM melts in the heat source, its volume increases, and hence the cylindrical tube is pressurized. Then, the pressurized hydraulic fluid can be released to do useful work and/or generate electricity (Figure 3.2(a)). As the PCM freezes in the heat sink, its volume decreases, thus the hydraulic fluid will be pushed back to the cylindrical tube by the ambient pressure.

The performance of the system can be examined in terms of both its thermal efficiency,

$$\eta = \frac{w}{q_{in}}, \tag{3.1}$$

and the specific energy (i.e, energy output per unit volume),

$$\omega = \frac{m^P w}{V}. \tag{3.2}$$

Here, q_{in} and w denote, respectively, the energy input and the work done by unit mass of PCM within one thermodynamic cycle. m^P denotes the mass of the PCM in the system. V denotes the volume of the prototype system.

η and ω depend on various parameters associated with the structural system, the PCM material, and the hydraulic fluid. The energy harvesting cycle described above is a nonlinear, thermo-mechanical coupled process. In particular, the melting temperature of a PCM depends sensitively on pressure. Therefore, it may vary significantly during the melting — and hence pressurization — process. In the case of a relatively low T_H and a high peak pressure,

the PCM will not melt completely, which leads to the reduction of both thermal efficiency and energy output. Furthermore, specific designs must satisfy various fabrication criteria. In particular, the peak pressure achieved within the system cannot exceed the maximum allowable working pressure of the structural system.

3.3 Prototype fabrication and experiments

Figure 3.2(b) presents a specific prototype fabricated based on the design described above. The system is designed to have an internal volume of 1.8×10^{-4} m^3, and to withstand a maximum hydrostatic pressure of 24 MPa without leaking or structural failure. Therefore, the horizontal tube is assembled using four Swagelok® stainless steel (316) tubes, each having an internal diameter of 2.12 cm, a wall thickness of 0.21 cm, and a length of 10.16 cm. The vertical tubes are assembled also using Swagelok® stainless steel (316) tubes, with an internal diameter of 1.02 cm and a wall thickness of 0.12 cm. The horizontal and vertical tubes are connected using Swagelok® compression type T-fittings (SS-1610-3-16-8). The horizontal tube is closed using two compression type end-caps (SS-1610-C). To monitor the internal pressure, a pressure gauge with a range of 41.37 MPa (6,000 psi) is connected to the horizontal tube using the same T-fitting. The DC water turbine generator (F50-12V) features a maximum voltage output of 12 V and a maximum power output of 10 W. Notably, the size — and hence power output — of the prototype can be scaled easily by changing the length of the horizontal tube and the mass of PCM.

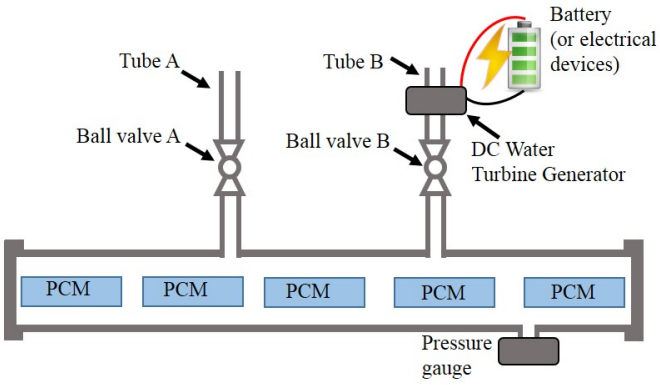

(a) A schematic drawing of the prototype

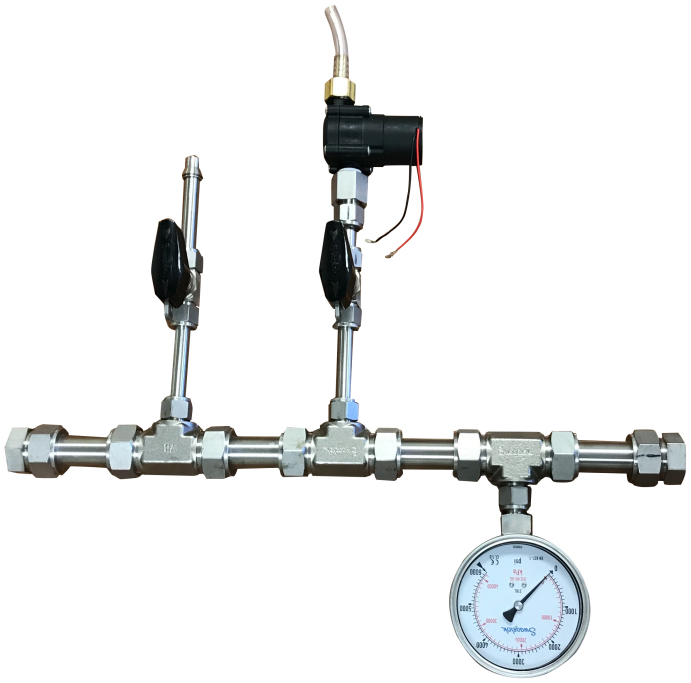

(b) A photograph of the fabricated prototype

Figure 3.2: Design and fabrication of a PCM-based thermal energy harvesting system.

The PCM used in the prototype is pentadecane ($C_{15}H_{32}$), purchased from SIGMA-ALDRICH® with a purity of 99%. It has a melting temperature of 10°C at the atmospheric pressure [23]. It has a density of 861 kg/m^3 in the solid phase, and 769 kg/m^3 in the liquid phase. Its latent heat capacity is $\Delta H_m = 205$ kJ/kg [24]. The specific heat capacity of $C_{15}H_{32}$, which depends on the temperature, can be expressed as ([23])

$$c_p(T) = \begin{cases} 1.88 \text{ kJ}/(\text{kg} \cdot \text{K}), & \text{if } T < 283.15 \text{ K}; \\ 0.00257T + 1.45 \text{ kJ}/(\text{kg} \cdot \text{K}), & \text{if } T > 283.15 \text{ K}. \end{cases} \tag{3.3}$$

The PCM is first kept in liquid phase, and degassed using a vacuum chamber and a vacuum pump (Figure 3.3(a)). Then, it is encapsulated in small packages, which are degassed and sealed using a vacuum sealer (Figure 3.3(b)). Each package contains 14 g PCM, while five packages are inserted into the horizontal tube through the left end. Degassed water is used as the hydraulic fluid in the experimental tests, for the ease of operation and cleaning.

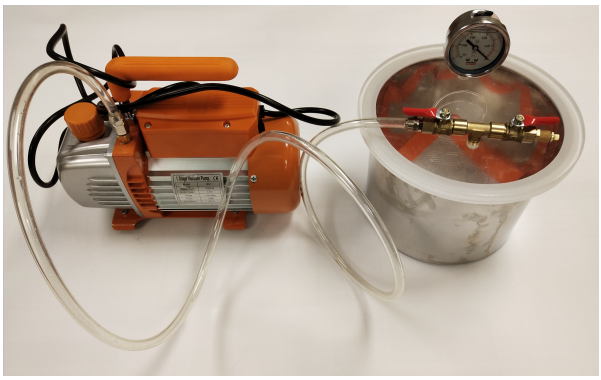

(a) Vacuum chamber and pump

(b) Vacuum sealer

Figure 3.3: Preparation of the PCM (pentadecane, $C_{15}H_{32}$) for energy harvesting

Two thermal reservoirs, representing a heat source at $T_H = 20°C$ and a heat sink at $T_C = 1°C$, are created using a water tank and a freezer, respectively. This setting can be interpreted in the context of ocean thermal energy harvesting, where the two thermal reservoirs represent, respectively, the warm water near ocean surface and the cold water at the bottom of the ocean thermocline [25].

To mimic one energy harvesting cycle, we first place the prototype in the low-temperature thermal reservoir for 6 to 8 hours, until the PCM is completely frozen. Then, we fill the system with hydraulic fluid, and close the valves on Tubes A and B. Next, we move the prototype into the high-temperature thermal reservoir, where the PCM melts and the internal pressure increases. Once the pressure stops increasing, we consider the system has reached thermal equilibrium, and record the pressure.

Through five repeated experiments, we find that the internal pressure is $P_2 = 23.6 \pm 0.35$MPa after the melting process, which takes approximately 4 hours. As shown in Table 3.1, the internal pressure increases rapidly within the first 2 hours. Then, the rate of increase drops dramatically. After 4 hours, the PCM is found to have completely melted.

Table 3.1: Time history of the measured internal pressure

Time (h)	internal pressure (MPa)	Standard deviation (5 measurements, MPa)
0	0.1	N/A
1	10.5	0.30
2	22.3	0.25
3	23.3	0.34
4	23.6	0.35
5	23.6	0.35

To measure the electrical energy output, a load resistor is connected to the DC water turbine

generator. A DIGILENT® USB oscilloscope (Analog Discovery 2) is used to measure the voltage across the resistor. The DIGILENT® WaveForms software is employed to control the measurement (e.g., specifying the data acquisition frequency, duration, and the start and termination time) and record the data.

The voltage and energy output depend sensitively on the load resistance. When the fluid flow through the generator is steady, the optimal load resistance — equal to the constant internal resistance of the generator — can be easily calculated. However, in the current experimental setting, the fluid flow through the generator is unsteady, and lasts for only a short period of time. As a result, the internal resistance of the generator is transient, and difficult to characterize. To determine the optimal load resistance that maximizes electrical energy output, we have tested six samples, including 25 Ohm, 50 Ohm, 100 Ohm, 150 Ohm, 200 Ohm, and 250 Ohm, while all other experiment parameters remain unchanged. Figure 3.4 presents the result of the measurement, which indicates that the optimal load resistance is approximately 100 Ohm, yielding a maximum energy output of 0.188 J. Further, Figure 3.5 presents the time histories of voltage and power obtained with the optimal load resistance.

Remark: The performance of the prototype is limited by the maximum allowable pressure of the structural system (24 MPa), which limits the volume fraction of PCM. We investigate the use of a hydraulic accumulator to mitigate this issue in Section 3.6.

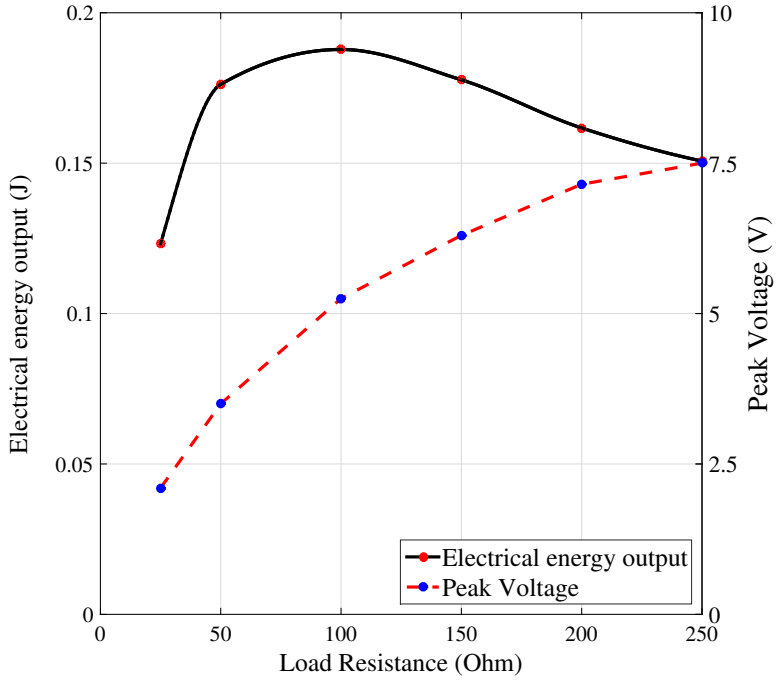

Figure 3.4: Dependence of energy output and peak voltage on load resistance

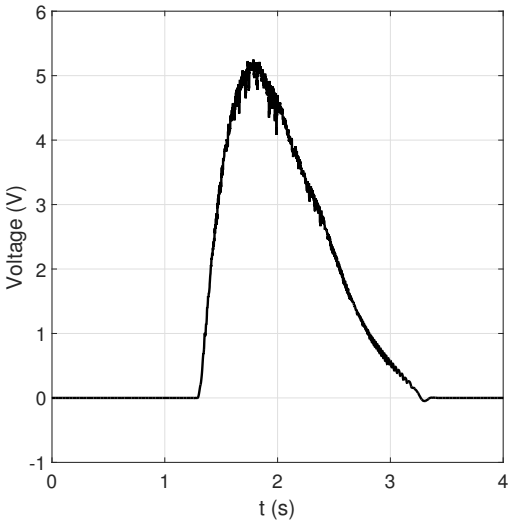

(a) Voltage with the load resistor of 100 Ohm

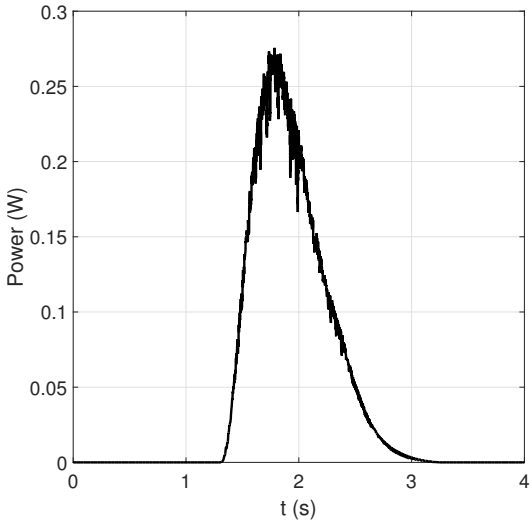

(b) Output power with the load resistor of 100 Ohm

Figure 3.5: Voltage and power with the load resistor of 100 Ohm

3.4 A thermomechanical model

We model the deformation of the cylindrical tubes under internal pressure loading using the linear elasticity theory. The solid material is assumed to be homogeneous and isotropic. The tubes are assumed to have small strain and plane stress. Therefore, the change of a tube's inner diameter under internal pressure P is given by [26]

$$\delta a = \frac{(P - P_0)a(1-\nu^2)}{E}\left(\frac{b^2 + a^2}{b^2 - a^2} + \frac{\nu}{1-\nu}\right), \tag{3.4}$$

where a and b are the internal and external diameters of the tube. E and ν are the Young's modulus and Poisson's ratio of the tube material. P_0 denotes the ambient pressure. Hence, the volume change of the prototype under pressure P is

$$\Delta V(P) = \frac{\pi}{4}\Big[L_1\big(2a_1 + \delta a_1(P)\big)\delta a_1(P) + 2L_2\big(2a_2 + \delta a_2(P)\big)\delta a_2(P)\Big], \tag{3.5}$$

where L denotes tube length. The subscript 1 denotes the horizontal tube that stores PCM, and 2 denotes the two vertical tubes (A and B) which have the same dimensions.

Tait equation of state [27, 28, 29] is used to model the thermodynamic behavior of the PCM in its liquid phase, and that of the hydraulic fluid. Specifically,

$$v_0^P(T) - v^P(P,T) = C^P(T)\log_{10}\Big(1 + \frac{P - P_0}{B^P(T)}\Big), \tag{3.6}$$

$$v_0^H(T) - v^H(P,T) = C^H(T)\log_{10}\left(1 + \frac{P - P_0}{B^H(T)}\right), \tag{3.7}$$

where the superscripts P and H refer to the PCM and the hydraulic fluid, respectively. The subscript 0 refers to the ambient pressure P_0. v denotes the specific volume. B and C are material-specific model inputs, given in [28] and [29] for pentadecane and liquid water (i.e. the hydraulic fluid used in the experiment).

The PCM has been degassed before encapsulation. However, the hydraulic fluid in the prototype still absorbs a certain amount of air. The volume ratio of air in the system is estimated to be $\alpha = 3.5\%$ at $P_0 = 101$ kPa and $T = 20°$C [30] . Its thermodynamic behavior is modeled by the ideal gas law,

$$\frac{Pv^A}{T} = const., \tag{3.8}$$

where v^A denotes the specific volume of the residual air.

We consider the scenario that the PCM can completely melt within the prototype. Figure 3.6 shows the thermodynamic cycle in this scenario. At State 1, the PCM is in the solid phase with specific volume v_1^P and pressure P_0. The path from State 1 to State 2 represents the process in which the PCM is placed in the high-temperature thermal reservoir for melting. During this process, the volume of PCM increases while the hydraulic fluid and residual air are compressed. In the meantime, the container is pressurized and deformed. This process takes up to 4 hours in our lab environment; therefore it can be considered as a quasi-static process. Enforcing static equilibrium between the fluid materials (i.e. PCM, hydraulic fluid,

and residual air) and the structural system yields

$$m^P\left[v^P(P,T) - v_1^P\right] + m^H\left[v^H(P,T) - v_1^H\right] + \left[V^A(P,T) - V_1^A\right] = \Delta V(P), \tag{3.9}$$

where m^P and m^H denote the mass of the PCM and the hydraulic fluid, respectively. v_1^P and v_1^H denote the specific volume of the PCM and hydraulic fluid, respectively. V_1^A denotes the volume of the residual air at State 1. $\Delta V(P)$ can be related to the dimensions and elastic properties of the structure through Equation (3.5). Similarly, $v^P(P,T)$, $v^H(P,T)$, $V^A(P,T)$ can be derived using their equations of state. Specifically, according to Equation (3.6),

$$v^P(P,T) = v_0^P(T) - C^P(T)\log_{10}(1 + \frac{P - P_0}{B^P(T)}). \tag{3.10}$$

The temperature range considered in this study is between 1°C and 20°C, and the maximum possible volume change of the hydraulic fluid (i.e. water) within this temperature range is less than 0.4% [31], which is much lower than that of the PCM (12%) [32]. Therefore, the thermal expansion of the hydraulic fluid can be ignored in the thermodynamic analysis, and hence

$$v_1^H = v_0^H(T_H). \tag{3.11}$$

Similarly, $v^H(P,T)$ can be expressed as

$$\begin{aligned} v^H(P,T) &= v^H(P,T_H) \\ &= v_0^H(T_H) - C^H(T_H)\log_{10}(1+\frac{P-P_0}{B^H(T_H)}) \end{aligned} \tag{3.12}$$

using Equation (3.7).

Due to the small volume fraction of the residual air (3.5%), the volume change of the residual air caused by the temperature change is expected to be less than 0.02% of of that of the PCM. Therefore, the temperature of the residual air is assumed to be invariant, fixed at T_H. Therefore,

$$V^A(P,T) = V^A(P,T_H) = \frac{V_1^A P_0}{P_2}. \tag{3.13}$$

The equilibrium pressure at State 2, denoted by P_2, can be obtained by substituting Equations (3.10), (3.11), (3.12) and (3.13) into Equation (3.9), and solving it with $T = T_H$. With the geometric and material parameters of the developed prototype (Table 3.2) and the experiment environment described before (i.e. $T_H = 20°$C and $P_0 = 101$ kPa), we obtain $P_2 = 22.7$ MPa. Notably, the predicted pressure P_2 matches reasonably well with the experimental measurement, with 3.40% difference. The values of other state variables at State 2 are shown in Table 3.3.

Next, the process from State 1 to State 2 can be determined by expressing the specific volume of the PCM, v^P, as a function of P, that is,

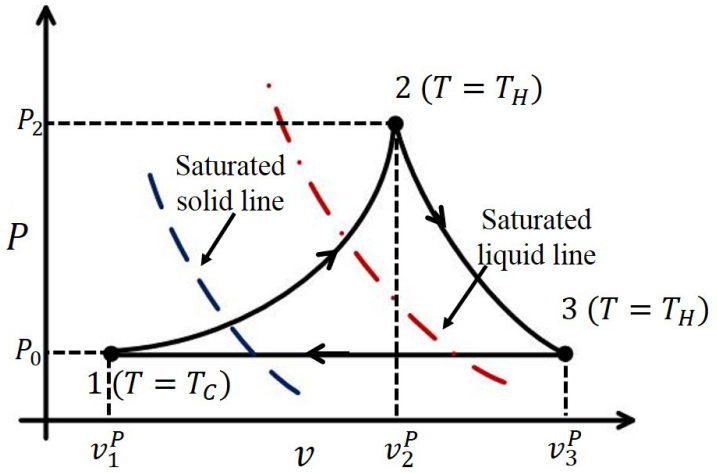

Figure 3.6: Thermodynamic cycle in the scenario that the PCM completely melts

Table 3.2: Input parameters

Parameter	Notation	Value
Mass of PCM	m^P	0.0700kg
Specific volume of PCM at State 1	v_1^P	1.16×10^{-3}m^3/kg
Mass of the hydraulic fluid	m^H	0.1091kg
Specific volume of the hydraulic fluid at State 1	v_1^H	1.00×10^{-3}m^3/kg
Volume of the residual air at State 1	V_1^A	6.9078×10^{-6} m^3
Internal diameter of the horizontal tube	a_1	2.12 cm
External diameter of the horizontal tube	b_1	2.54 cm
Length of the horizontal tube	L_1	0.52 m
Internal diameter of the vertical tubes	a_2	1.02 cm
External diameter of the vertical tubes	b_2	1.26 cm
Length of the vertical tubes	L_2	0.10 m
Temperature of the heat source	T_H	20.0°C
Temperature of the heat sink	T_C	1.0°C
Pressure at State 1	P_0	0.101 MPa

Table 3.3: Solution obtained from the thermomechanical model

Solved variable	Notation	Value
Specific volume of PCM at State 2	v_2^P	1.2793×10^{-3}m^3/kg
Specific volume of the hydraulic fluid at State 2	v_2^H	0.9899×10^{-3}m^3/kg
Volume of the residual air at State 2	V_2^A	3.0735×10^{-8}m^3
Pressure at State 2	P_2	22.7 MPa

$$v^P(P) = \frac{\Delta V(P) + m^H C^H(T_H) \log_{10}\left(1 + \frac{P-P_0}{B^H(T_H)}\right) + V_1^A\left(1 - \frac{P_0}{P}\right)}{m^P} + v_1^P. \tag{3.14}$$

In particular, the path from State 1 to 2 shown in Figure 3.6 is plotted using Equation 3.14, with maximum pressure $P_2 = 22.7$ MPa, and the parameter values in Table 3.2.

The process from State 2 to State 3 represents the idealized pressure releasing process, which is assumed to be quasi-static and isothermal. In this process, according to Equation (3.6), the specific volume of PCM is

$$v^P(P) = v_0^P(T_H) - C^P(T_H) \log_{10}\left(1 + \frac{P - P_0}{B^P(T_H)}\right) \tag{3.15}$$

At State 3, the pressure reduces to P_0. The specific volume of PCM increases to v_3^P, while the temperature remains at T_H. Finally, the path from State 3 to State 1 corresponds to the freezing of PCM in the low-temperature thermal reservoir, which is assumed to be an isobaric process.

The work done by unit mass of PCM within one thermodynamic cycle is given by

$$w = \int_{v_1^P}^{v_2^P} (P - P_0) dv + \int_{v_2^P}^{v_3^P} (P - P_0) dv. \tag{3.16}$$

Notably, the first term on the right hand side can be evaluated without performing the inte-

gration of the PCM $P-v$ diagram in the melting process. Instead, by enforcing conservation of energy,

$$w_{1-2} = \int_{v_1^P}^{v_2^P} P dv = \frac{U + W^H}{m^P}, \tag{3.17}$$

where U denotes the total strain energy of the prototype structure, given by

$$\begin{aligned} U &= \int_{V_0}^{V_0+\Delta V(P_2)} (P - P_0) dV \\ &= \int_{P_0}^{P_2} (P - P_0) \frac{dV}{dP} dP \\ &= \frac{\pi L_1}{4} \left[(P_2 - P_0) a_1 \delta a_1 + \frac{2}{3} (P_2 - P_0) \delta a_1^2 \right] \\ &+ \frac{\pi L_2}{2} \left[(P_2 - P_0) a_2 \delta a_2 + \frac{2}{3} (P_2 - P_0) \delta a_2^2 \right]. \end{aligned} \tag{3.18}$$

W^H denotes the work done by the PCM to the hydraulic fluid, given by

$$\begin{aligned} W^H &= m^H \int_{v_2^H}^{v_1^H} (P - P_0) dv^H \\ &= m^H B^H C^H \left[\frac{P_2 - P_0}{\log(10) B^H} - \log_{10}(1 + \frac{P_2 - P_0}{B^H}) \right]. \end{aligned} \tag{3.19}$$

The second term in Equation (3.16) can be evaluated as

$$\begin{aligned} w_{2-3} &= \int_{v_2^P}^{v_3^P} (P - P_0) dv \\ &= B^P C^P \left[\frac{P_2 - P_0}{\log(10) B^P} - \log_{10} \left(1 + \frac{P_2 - P_0}{B^P} \right) \right]. \end{aligned} \tag{3.20}$$

Finally, the thermal efficiency is given by

$$\eta = \frac{w}{q_{in}} = \frac{w}{\Big(\int_{T_C}^{T_H} c_p(T)dT\Big) + \Delta H_m + w}, \tag{3.21}$$

where c_p is the specific heat capacity of PCM and ΔH_m is the specific latent heat of fusion. The specific energy output is given by

$$\omega = \frac{m^P w}{V} = \frac{m^P w}{\frac{\pi L_1 b_1^2}{4} + \frac{\pi L_2 b_2^2}{2}}, \tag{3.22}$$

where V denotes the volume of the system.

Remark: Equation (3.10) and the thermodynamic cycle shown in Figure 3.6 hold if and only if the PCM completely melts, i.e. when

$$T_m(P_2) \leq T_H, \tag{3.23}$$

where $T_m(P_2)$ denotes the melting temperature of the PCM at pressure P_2. For pentadecane, the dependence of T_m on pressure is approximately linear within the range of our interest [22]. Specifically, for 0.101 MPa $< P <$ 450 MPa, we have

$$T_m = \gamma P + \beta, \tag{3.24}$$

with $\gamma = 0.2022$ K/MPa and $\beta = 283.15$ K. If the pressure P_2 obtained through Equation (3.9) (which assumes complete melting) violates Inequality (3.23), it means the PCM can not completely melt in the designed thermodynamic cycle. In this case, Equation (3.10) is no longer valid. It is straightforward to prove that incomplete melting of PCM will cause both η and ω to decrease.

3.5 Parametric study

The thermomechanical model can be used as a design tool to investigate the effect of system parameters — such as the stiffness of the structural system and the volume ratio of PCM — on the performance of specific PCM-based thermal energy harvesting systems.

Figures 3.7 and 3.8 show the dependence of η and ω on the wall thickness of the tubes and the temperature differential (ΔT), in which T_C is fixed to be 1°C and T_H is varied. The volume fraction of PCM is identical to that of the developed system, i.e. $f = 41.21\%$. In particular, the wall thickness of different sections of the prototype are varied simultaneously by the same factor, τ, within the interval of 1.0 to 4.0. In both figures, the black dash line separates the two scenarios in which the PCM melts completely — correspondingly, the right side of the dash line — or incompletely, i.e. the left side, under the designed thermodynamic cycle (Figure 3.6). In the scenario where the PCM cannot melt completely, the values of the thermal efficiency and specific energy output are calculated based on a modified thermodynamic cycle, which includes an additional isobaric expansion process.

Details of this thermodynamic cycle and the corresponding thermomechanical model are shown in Appendix A.

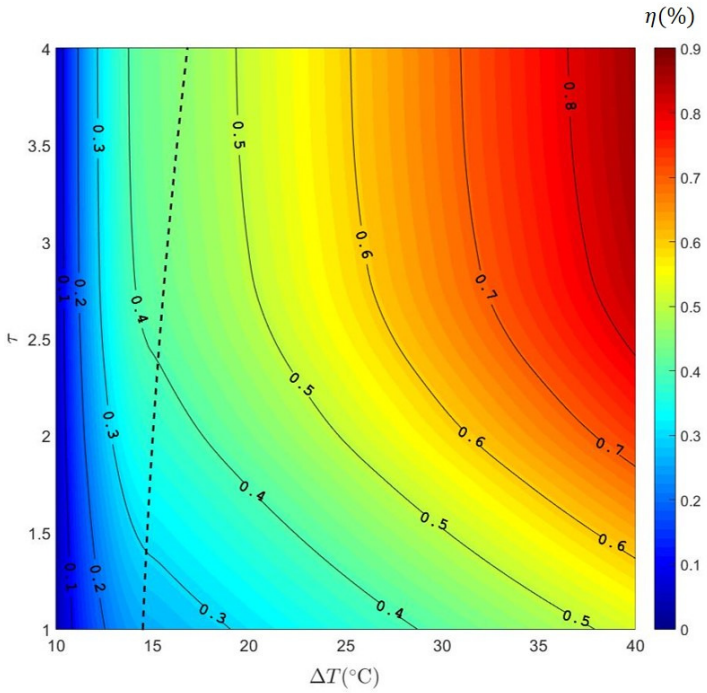

Figure 3.7: Dependence of $\eta(\%)$ on the wall thickness of tubes with $f = 41.21\%$

Figure 3.7 shows that for any given ΔT, η increases monotonically with τ. This is because as τ increases, the structural system undergoes smaller expansion, leading to higher peak pressure P_2 inside the system. The rate of increase of η (i.e. $\partial\eta/\partial\tau$) gradually drops, indicating that as the tube walls become thicker (or more generally, the structure becomes stiffer), the marginal gain of further increasing the thickness (or stiffness) becomes smaller. For example, for $\Delta T = 20°\text{C}$, $\eta = 0.49\%$ with $\tau = 3$. In comparison, with a completely rigid structure, i.e. $\tau = \infty$, η is 0.51%, that is, only 3.92% higher. Figure 3.7 also shows that for a fixed value of τ, $\partial\eta/\partial\tau$ increases as ΔT increases. This suggests that in scenarios where η is a design objective, the optimal structural stiffness depends on ΔT, and will likely be

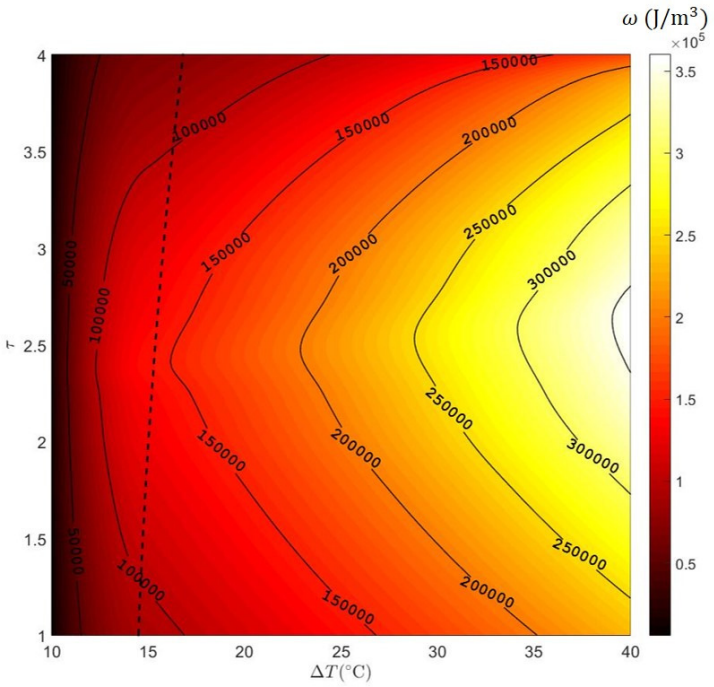

Figure 3.8: Dependence of $\omega(\mathrm{J/m^3})$ on the wall thickness of tubes with $f = 41.21\%$

larger for a higher value of ΔT.

The effect of wall thickness, τ, on the specific energy output ω is clearly different. Figure 3.8 shows that for any given ΔT, as τ increases, ω first increases, then decreases. For example, for $\Delta T = 25°\mathrm{C}$, ω starts decreasing when τ is approximately 2.5, that is, when the main tube has a thickness of 0.54 cm. When $\tau = 4$, the value of ω is smaller than that achieved with $\tau = 1$. This is because when τ becomes excessively large, its benefit in stiffening the structural system is overridden by the resulting increase of structural volume. Figure 3.8 also shows that the optimal value of τ (in terms of maximizing ω) increases with ΔT. Moreover, a comparison of Figures 3.7 and 3.8 indicates a trade-off between thermal efficiency (η) and specific energy output (ω) when designing the structural system of the energy harvester.

Figures 3.9 and 3.10 present the dependence of η and ω on the volume fraction of PCM (f) and the temperature differential (ΔT), with $\tau = 1$. Again, the two regions separated by the black dash line represent the two scenarios in which PCM melts completely and incompletely.

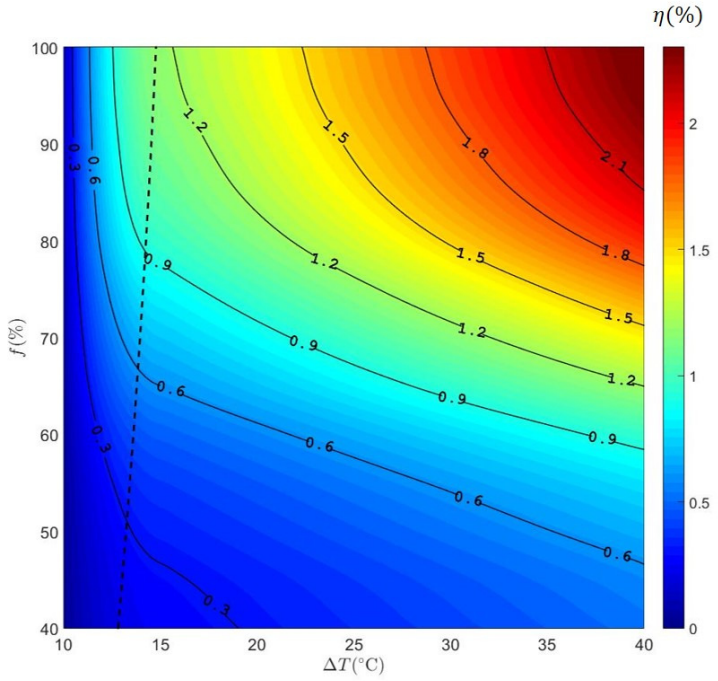

Figure 3.9: Dependence of $\eta(\%)$ on the volume fraction of PCM with $\tau = 1$

Evidently, both η and ω are monotonically increasing functions of f. This is essentially because as f increases, the peak pressure obtained at the end of the melting process, P_2, also increases. Notably, Figure 3.9 shows that for fixed ΔT, the dependence of η on f exhibits a transition from a convex function (for small f) to a concave function (for large f). The transition point at which the second derivative becomes zero is around 70%, dependent upon ΔT. This behavior is due to the fact that the work done by the PCM to the surrounding hydraulic fluid depends on two competing factors: the peak pressure P_2, and the mass of the hydraulic fluid, m^H (Equation 3.19). Specifically, as f increases, P_2 increases, whereas m^H

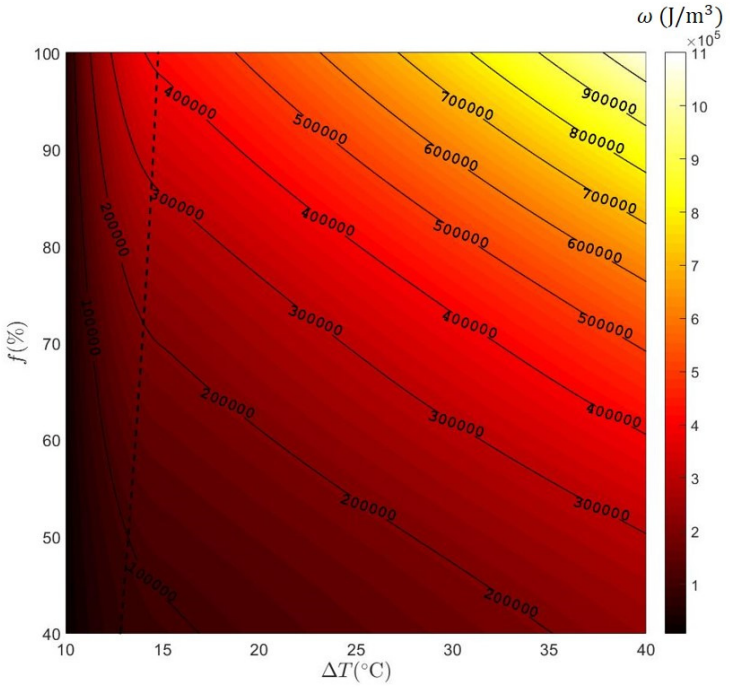

Figure 3.10: Dependence of $\omega(\mathrm{J/m^3})$ on the volume fraction of PCM with $\tau = 1$

decreases.

Remark: Alternatively, the specific energy output can be defined per unit mass, i.e.

$$\omega_m = \frac{W}{m^P + m^H + m^S}, \tag{3.25}$$

where m^P, m^H, m^S denote the mass of the PCM, the hydraulic fluid, and the structural system, respectively. We have found that ω_m exhibits the same trends with respect to the variations of τ and f as ω does.

3.6 Pressure control and performance improvement with a hydraulic accumulator

Despite the potential improvement of both thermal efficiency and specific energy output, in practice the increase of the volume fraction of PCM (f) can be limited by the resulting high pressure in the energy harvesting system (P_2). For example, the fabricated prototype described previously is filled partially with PCM, up to 41.21% of its internal volume. At this volume fraction, the peak pressure inside the prototype is measured to be 23.6 ± 0.35 MPa, which is close to the maximum allowable working pressure of the system (24 MPa). More generally, when the volume fraction of PCM approaches 100% and ΔT gets close to 40°C, the peak pressure will exceed 150 MPa, which is difficult to maintain in many engineering applications. Therefore, it is useful to investigate additional methods to improve thermal efficiency and specific energy output, without increasing the peak pressure inside the system. To this end, we consider the use of a piston type hydraulic accumulator, which can be connected to the developed prototype relatively easily. The basic idea is that a calibrated hydraulic accumulator may allow more PCM to be inserted into the system and melted completely, while maintaining a constant peak pressure. Also, the thermal energy harvested by unit mass of PCM will increase because the PCM will do work to the piston during the melting process. Figure 3.11 presents a schematic drawing of the modified design, together with a photograph of the new prototype developed based on this design.

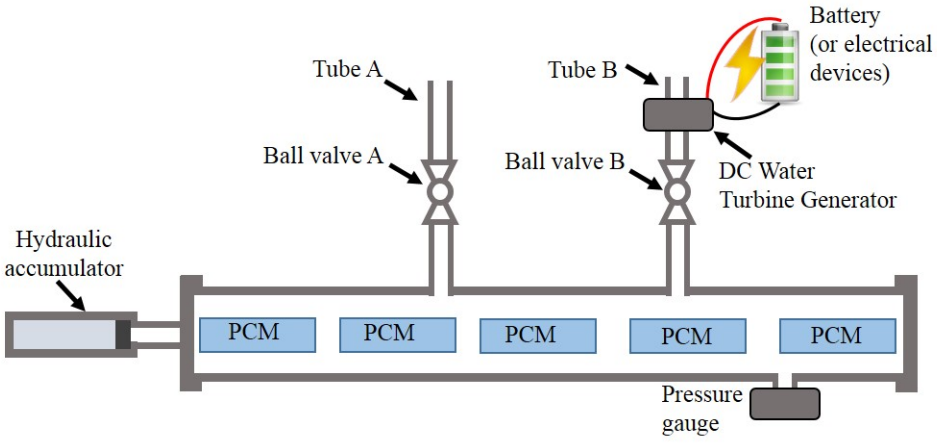

(a) A schematic drawing of the design with the hydraulic accumulator.

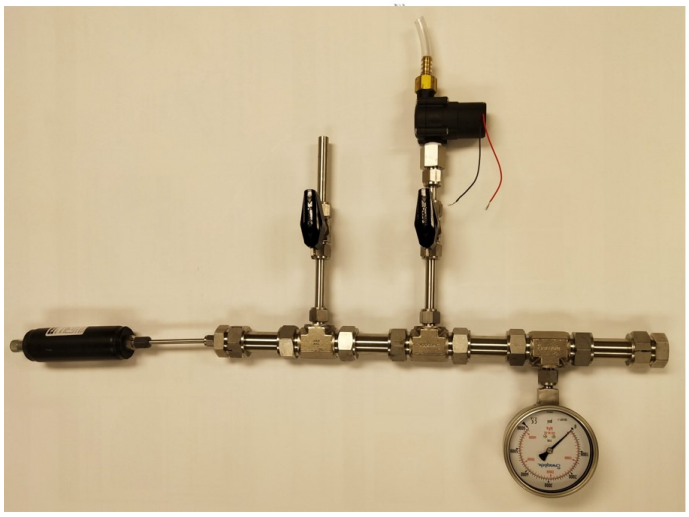

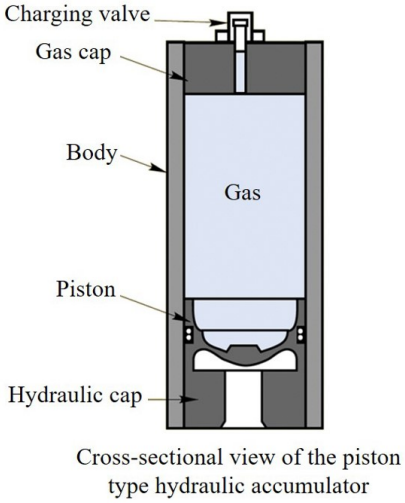

(b) Photograph of the fabricated prototype with the accumulator. The cross-sectional image (right) is adapted from the user's manual of Parker® piston type hydraulic accumulator (Model ACP04AA-002R1KTB)

Figure 3.11: Fabrication of a prototype with the hydraulic accumulator

Piston type hydraulic accumulators are usually in the form of pressure vessels, and are often installed in hydraulic systems to store energy in the form of pressurized gas and to regulate pressure (e.g., [33, 34, 35]). In most cases, the hydraulic accumulator is filled with gas (e.g., nitrogen) and pre-charged to a certain pressure, denoted here as P_a. The piston is not activated when the external pressure is below P_a. When the external pressure exceeds P_a, the piston is compressed, and hence the internal gas is pressurized. If the hydraulic accumulator is connected to a closed system — such as in the present application — the motion of the piston will also increase the internal volume of the connected system, and hence reduces its internal pressure. In the modified design shown in Figure 3.11, we use the hydraulic accumulator to regulate P_2. Specifically, for a given PCM volume fraction f (up to 100% in theory), we tune the value of P_a to ensure that P_2 is below the maximum allowable working pressure of the system, and at the same time, sufficiently low to ensure the complete melting of the PCM, that is, $T_m(P_2) < T_H$.

When P_2 and f are specified, to determine P_a, we consider the interaction between the fluid materials and the structural system. In this regard, the thermodynamic behavior of the internal gas of the hydraulic accumulator is modeled by the ideal gas law,

$$\frac{Pv^N}{T} = const., \tag{3.26}$$

where v^N denotes the specific volume of the gas. Enforcing static equilibrium between the

fluid materials (i.e. PCM, hydraulic fluid, residual air, and the internal gas of the hydraulic accumulator) and the structural system after the PCM completely melts (i.e. when the pressure reaches P_2) yields

$$m^P(v_2^P - v_1^P) + m^H(v_2^H - v_1^H) + (V_2^A - V_1^A) + (V_2^N - V_1^N) = \Delta V(P_2), \tag{3.27}$$

where V_1^N and V_2^N denote the initial and the final volume of the internal gas of the hydraulic accumulator (i.e. nitrogen).

For a fixed value of f,

$$m^P = \frac{Vf}{v_1^P}, \tag{3.28}$$

and

$$m^H = \frac{V(1-f) - V_1^A}{v_1^H}, \tag{3.29}$$

where V denotes the initial volume of the structural system.

Furthermore, when P_2 is specified, v_2^P, v_2^H, and V_2^A can be calculated using the equations of state of the PCM, the hydraulic fluid, and the residual air, i.e. Equations (3.6), (3.7) and (3.8). The volume change of the structural system, ΔV, can be obtained through the structural elasticity, i.e. Equation (3.5).

Assuming the hydraulic accumulator is pre-charged at temperature T_H, then

$$V_2^N = \frac{P_a V_1^N}{P_2}. \tag{3.30}$$

Substituting Equation (3.30) into Equation (3.27), the only remaining unknown is P_a. Solving the equation gives

$$\begin{aligned} P_a &= \frac{P_2}{V_1^N}\Big\{\Delta V(P_2) + V_1^N - V_1^A\big(\frac{P_0}{P_2} - 1\big) - \frac{Vf}{v_1^P}\big[v_0^P - C^P \log_{10}(1 + \frac{P_2 - P_0}{B^P}) - v_1^P\big] \\ &+ \frac{V(1-f) - V_1^A}{v_1^H} C^H \log_{10}(1 + \frac{P_2 - P_0}{B^H})\Big\}. \end{aligned} \tag{3.31}$$

In this work, we connect to the original prototype a Parker® piston type hydraulic accumulator (Model ACP04AA-002R1KTB) [36]. The initial volume of the internal nitrogen gas is $V_1^N = 8 \times 10^{-5}\text{m}^3$. The maximum working pressure of the hydraulic accumulator is 26 MPa. To assess the effectiveness of the hydraulic accumulator, we maintain the same peak pressure, $P_2 = 23.6$ MPa. We increase the amount of PCM from 70 g to 113 g, the latter corresponding to volume fraction $f = 66.52\%$. For this setting, the required pre-charged pressure P_a is 21 MPa, obtained through Equation (3.31).

Due to the addition of the hydraulic accumulator and the increase of the mass of PCM, the flow rate in the pressure releasing process will be different from that of the original system, which may lead to the change of the optimal resistance. Therefore, we test a series of different load resistance to determine the optimal load resistance that maximizes electrical energy output. Figure 3.12 shows the electrical energy output achieved with 7 different load resistance values between 25 Ohm and 300 Ohm, which indicates that the optimal load resistance is approximately 150 Ohm, yielding a maximum energy output of 0.259 J. The voltage and power outputs with 150 Ohm load resistance are shown in Figures 3.13(a)

and 3.13(b). Compared with the system without the hydraulic accumulator, the electrical energy increases by 37.77%. Besides, the peak pressure P_2 within the system is measured to be 22.7 ± 0.3MPa, which has a small discrepancy of 3.8% with the design value.

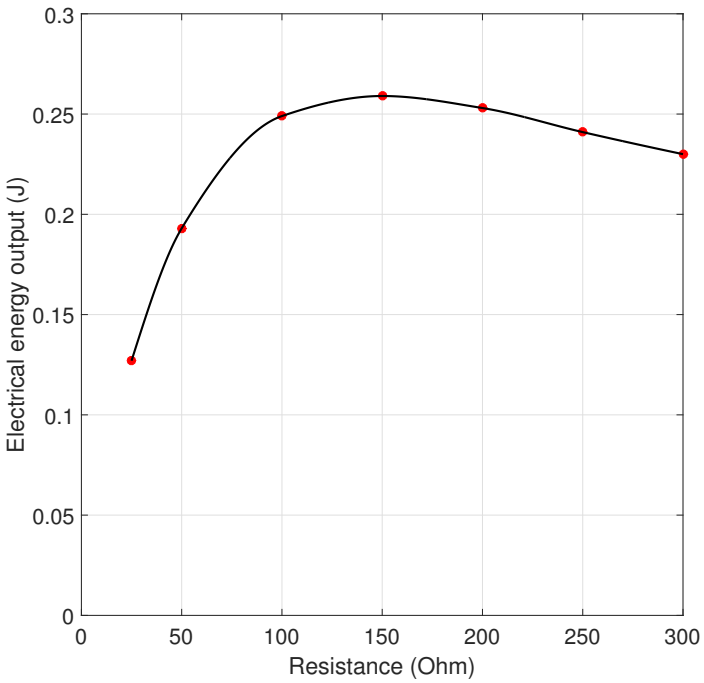

Figure 3.12: Dependence of the electrical energy output on the load resistance with the accumulator

To explain the effect of the hydraulic accumulator, Figure 3.14 compares the thermodynamic cycles underlying the original and the modified prototype. In the $P - v$ diagram, both thermodynamic cycles start at the same state, i.e. State 1, in which the PCM is in the solid phase. For the modified prototype, when the pressure increases from P_0 to P_a, the hydraulic accumulator is not activated, and the specific volume of PCM is given by Equation (3.14). Compared with the original prototype without the accumulator, f becomes greater, which leads to a higher value of m^P and a lower value of m^H. Therefore, the value of v^P with the

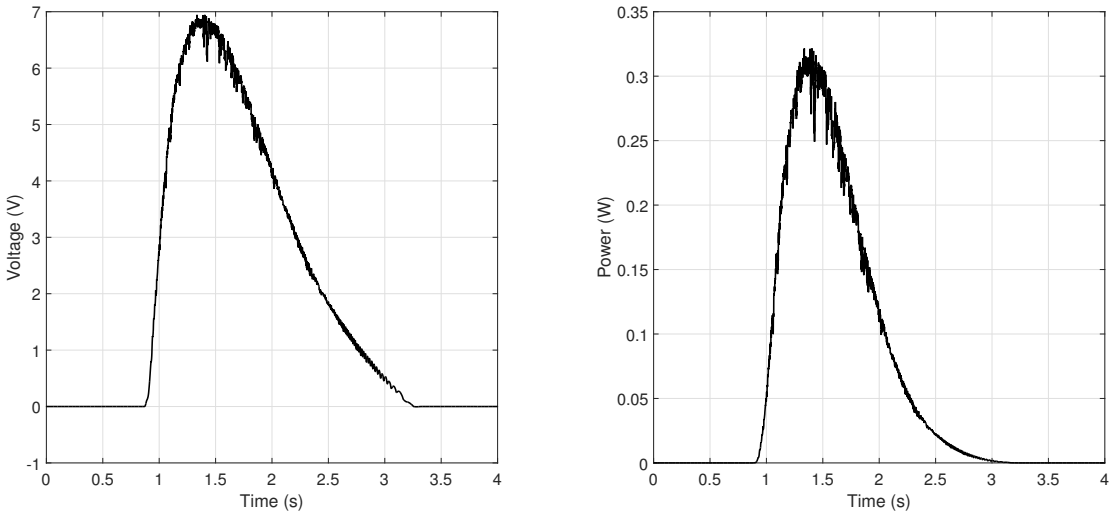

(a) Voltage output (b) Power output

Figure 3.13: Voltage and power outputs with 150 Ohm load resistance and the hydraulic accumulator

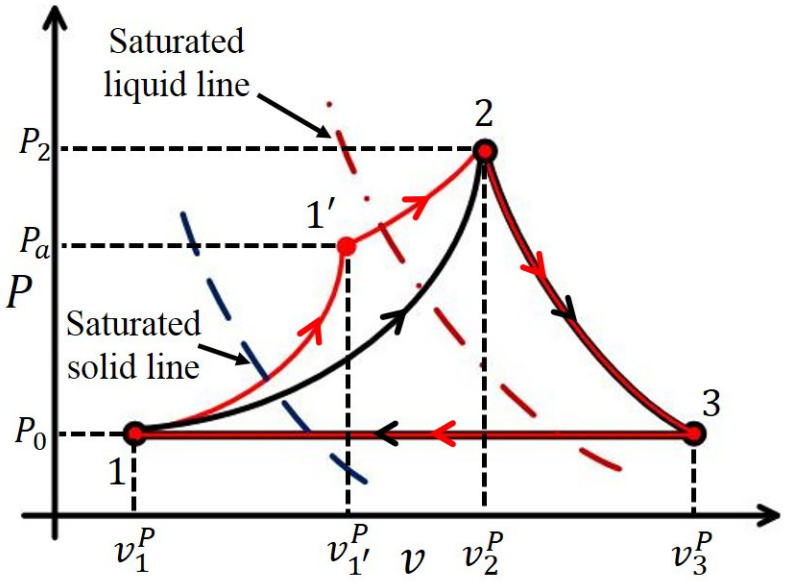

Figure 3.14: Thermodynamic cycles with and without the hydraulic accumulator, which are denoted by the red and black curves, respectively

hydraulic accumulator is always lower than that without the hydraulic accumulator when the pressure increases from P_0 to P_a. In other words, the pressure with the hydraulic accumulator is always greater than that without the hydraulic accumulator when the specific volume of PCM, v^P, increases from v_1^P to $v_{1'}^P$. In particular, the process from State 1 to State 1′ in Figure 3.14 is plotted according to Equation (3.14) for the modified prototype.

When the pressure exceeds P_a (i.e. State 1′), the hydrualic accumulator is activated, and the internal gas is compressed. From State 1′ to State 2, the specific volume of PCM is given by

$$v^P(P) = \frac{\Delta V(P) + m^H C^H \log_{10}(1 + \frac{P - P_0}{B^H}) + V_1^A(1 - \frac{P_0}{P}) + V_1^N(1 - \frac{P_a}{P})}{m^P} + v_1^P, \quad (3.32)$$

where $\Delta V(P)$ can be calculated by Equation 3.5. Due to the hydraulic accumulator, the rate of pressure increase (i.e. $\partial P/\partial v^P$) drops. The process from State 1′ to State 2 in Figure 3.14 is plotted using Equation (3.32) for the modified prototype, with $P_2 = 23.6$ MPa. It shows that in this process, the pressure achieved by the modified prototype is still higher compared to the original prototype. When the melting process completes, both thermodynamic cycles with and without the hydraulic accumulator reach the same State 2. The paths from State 2 to State 3 and from State 3 to State 1 represent, respectively, the pressure releasing process and the freezing process. In these two processes, the paths undertaken by the two prototypes with and without the hydraulic accumulator overlap with each other.

Evidently, Figure 3.14 shows that the work done by unit mass of PCM within one ther-

modynamic cycle (w) with the accumulator is greater than that without the accumulator. Therefore, the thermal efficiency (η) and the specific energy output (ω) achieved with the hydraulic accumulator are greater than those without the hydraulic accumulator.

Specifically, the work done by unit mass of PCM within one thermodynamic cycle (w) is given by Equation (3.16). For the modified prototype, the first term on the right hand side needs to be calculated as

$$w_{1-2} = \int_{v_1^P}^{v_2^P} (P - P_0) dv = \frac{U + W^H + W^N}{m^P}, \tag{3.33}$$

to account for the the work done by the PCM to the nitrogen gas in the hydraulic accumulator, i.e. W^N, which is given by

$$W^N = \int_{V_2^n}^{V_1^n} P dV^n = P_a V_1^n \log\left(\frac{P_2}{P_a}\right). \tag{3.34}$$

Then, the thermal efficiency and specific energy output can be calculated according to Equations (3.21) and (3.22), which gives

$$\eta = 0.60\%, \tag{3.35}$$

$$\omega = 2.12 \times 10^5 \mathrm{J/m^3}, \tag{3.36}$$

for the modified energy harvesting system with the hydraulic accumulator

In comparison, the values of η and ω obtained with the original prototype without the

hydraulic accumulator are 0.31% and $1.05 \times 10^5 \mathrm{J/m^3}$. Therefore, the hydraulic accumulator leads to a 94% improvement in thermal efficiency, and a 102% improvement in specific energy output.

Parenthetically, the thermal efficiency of the modified energy harvesting system with the hydraulic accumulator can be compared with that of thermoelectric generators (TEGs). TEGs have been widely used to harvest environmental thermal energy associated with a small temperature differential [37, 38, 39, 40, 41]. The thermal efficiency of TEGs can be estimated by [42]

$$\eta_{TEG} = \frac{T_H - T_C}{T_H} \frac{\sqrt{1 + Z\overline{T}} - 1}{\sqrt{1 + Z\overline{T}} + T_C/T_H}, \tag{3.37}$$

where

$$Z\overline{T} = \frac{S^2\sigma}{\lambda} \frac{T_H + T_C}{2}, \tag{3.38}$$

and S, σ and λ denote, respectively, the Seebeck coefficient, the electrical conductivity and the thermal conductivity of the thermoelectric material. For the temperature differential in our experiments ($\Delta T = 19°\mathrm{C}$ with $T_H = 20°\mathrm{C}$ and $T_C = 1°\mathrm{C}$), $Z\overline{T}$ is approximately 0.4 [43] for state-of-the-art Bi_2Te_3 type TEGs. Therefore, η_{TEG} is approximately 0.56%. In comparison, the thermal efficiency of the developed prototype is slightly higher than that of commercial TEGs. Moreover, a salient feature of the developed energy harvesting system is that it does not need to be in contact with the heat source and sink at the same, which makes it applicable in some scenarios where TEGs may not work.

It is also noteworthy that with the same temperature differential the Carnot efficiency is

$$\eta_C = 1 - \frac{T_C}{T_H} = 6.5\%, \tag{3.39}$$

which indicates that the thermal efficiency of the developed energy havesting system is still significantly lower than the theoretical upper limit. However, it is notable that, in the scenarios where the developed energy harvesting system is applicable, the energy source is often abundant and free. Therefore, a low thermal efficiency may still be acceptable.

To further investigate the performance improvement obtained with the hydraulic accumulator, a parameter study is performed. Figures 3.15 and 3.16 present the dependence of η and ω on f and ΔT. The upper limit of peak pressure P_2 within the system is set to be 24 MPa to account for the maximum allowable working pressure of the structural system. In both figures, the white dash line separates the two scenarios in which the hydraulic accumulator is activated — correspondingly, the right side of the dash line — or not, i.e. the left side. Evidently, both η and ω still increase monotonically with f for any given ΔT. The maximum possible values of η and ω obtained with the hydraulic accumulator are 2.12% and $8.43 \times 10^5 \mathrm{J/m^3}$, respectively, at $f = 100\%$ and $\Delta T = 40^\circ\mathrm{C}$. In comparison, with the same upper limit of the peak pressure, for the system without the hydraulic accumulator, the maximum possible values of η and ω are 1.18% and $4.13 \times 10^5 \mathrm{J/m^3}$, respectively. Therefore, the analysis suggests that the use of a hydraulic accumulator can increase the maximum possible values of η and ω by 80% and 104%, respectively.

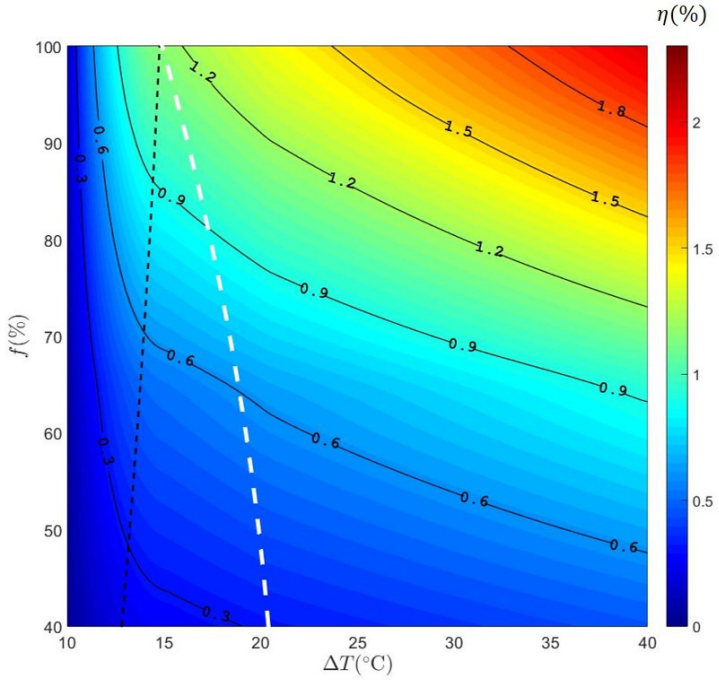

Figure 3.15: Dependence of $\eta(\%)$ on the volume fraction of PCM with the hydraulic accumulator

Remark: The efficiency of environmental thermal energy harvesting is inevitably limited by the small temperature differentials in the natural environment (e.g., spatial variation of temperature in ocean/air, and diurnal temperature change). Nevertheless, there are a wide variety of sensors and unmanned vehicles that are designed to conduct long-term missions in scenarios with direct access to environmental thermal energy. Currently, many of these devices are powered by battery, therefore have to be discarded or collected and recharged after the battery expires. For this type of devices, small-scale, portable thermal energy harvesters — such as those presented in this paper — indicate a unique approach for extending the mission range and service life. For example, Table 3.4 presents a list of sensors that can be powered by PCM-based environmental thermal energy harvesters.

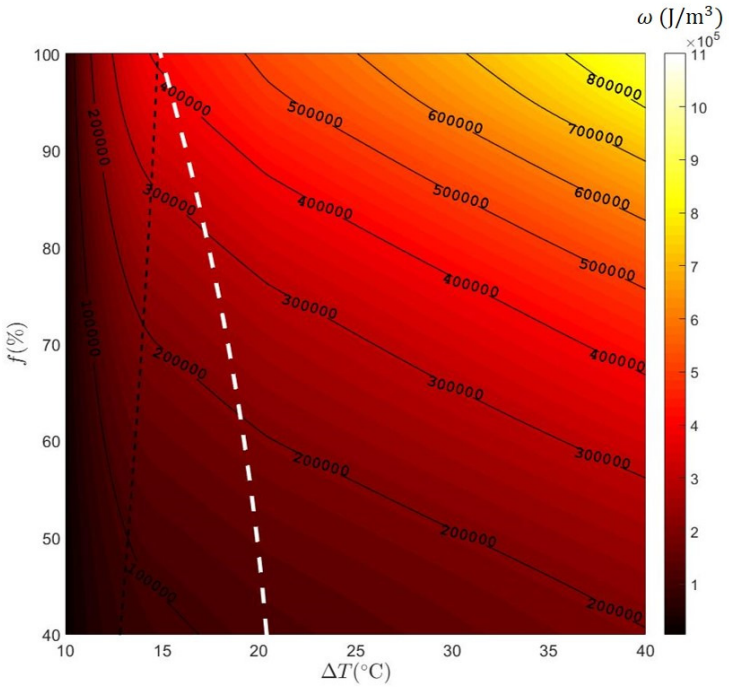

Figure 3.16: Dependence of $\omega(\mathrm{J/m^3})$ on the volume fraction of PCM with the hydraulic accumulator

Table 3.4: Potential applications of small-scale environmental thermal energy harvesters

Device	Main components	Power (W)
Dust sensor [44]	LED and light detector	$\sim 10^{-1}$
Motion sensor [45]	Pyroelectric material	$\sim 10^{-3}$
Piezoelectric resonant pressure sensor [46]	Piezoelectric material	$\sim 10^{-5}$
Capacitive ceramic pressure sensor [46]	Air-gap capacitor	$\sim 10^{-6}$
Temperature sensor [47]	Thermal diode	$\sim 10^{-7}$

3.7 Conclusion

This paper presents a combined experimental and theoretical study on harvesting environmental thermal energy using solid/liquid phase change materials (PCM). Specifically, we started with presenting the design, fabrication, and testing of a portable thermal energy harvester that utilizes pentadecane ($C_{15}H_{32}$, melting temperature: 10°C at atmospheric pressure) as PCM. To illustrate the mechanism of the device and analyze its performance, we have presented a thermo-mechanical model that couples the thermodynamic behaviors of the involved materials (PCM, hydraulic fluid, and residual air) and the elastic deformation of the structural system. The model is validated by comparing the predicted peak pressure with the experimental data, which shows a relatively small discrepancy of 3.40%. Using both the fabricated prototype and the model, we have shown that a significant issue that limits the performance of such devices is that achieving high thermal efficiency and specific energy output requires maintaining a high pressure inside the device, possibly in the range of hundreds of MPa. The high pressure not only imposes a stringent constraint for structural design, but also leads to incomplete melting of the PCM. To mitigate this issue, we have proposed the idea of using a hydraulic accumulator to regulate the internal pressure, and modified both the prototype and the thermo-mechanical model accordingly. We have shown that a calibrated hydraulic accumulator allows more PCM to be inserted into the system and melted completely. It also improves the specific energy output by allowing the PCM to do work to the (piston-type) accumulator. Specifically, for the fabricated prototype, the use of a hydraulic accumulator increases the thermal efficiency by 80%, and the specific

energy output by 104%. In particular, the thermal efficiency obtained with the hydraulic accumulator is found to be 0.60% when operating between 1 and 20°C, which is on par with state-of-the-art thermoelectric generators. The model also predicts that by further increasing the volume fraction of PCM and operating with a larger temperature difference (40°C), the thermal efficiency and the specific energy output can reach 2.12% and 8.43×10^5 J/ m^3, respectively.

At the end, we note that the performance of the current prototype is limited by the use of an off-the-shelf hydroelectric generator that is not optimized for the pulsatile flow produced by the harvester. The design and use of special hydroelectric generators is therefore a research direction that may lead to significant performance improvement in future.

Acknowledgements

G.W., D.H. and K.W. acknowledge funding from the Institute for Critical Technologies and Applied Sciences (ICTAS) at Virginia Tech. K.W. also acknowledges funding from the Office of Naval Research (ONR) under Award Number N00014-18-1-2059. The authors thank Drs. Yi Chao and Thomas Curtin for their guidance and assistance on the design of this study.

Appendix A

For the sake of completeness, we present a modified thermodynamic cycle for the scenario where the PCM cannot completely melt within the developed energy harvesting system (Section 3.4). In this scenario, Inequality (3.23) will be violated with the value of P_2 obtained from the original thermomechanical model, in which the PCM is assumed to be able to completely melt within the system.

The modified thermodynamic cycle features an additional isobaric expansion process, as shown in Figure 3.17. The melting process still starts from State 1. If the PCM cannot completely melt, the melting process stops at State 2', in which

$$T_m(P_{2'}) = T_H. \tag{3.40}$$

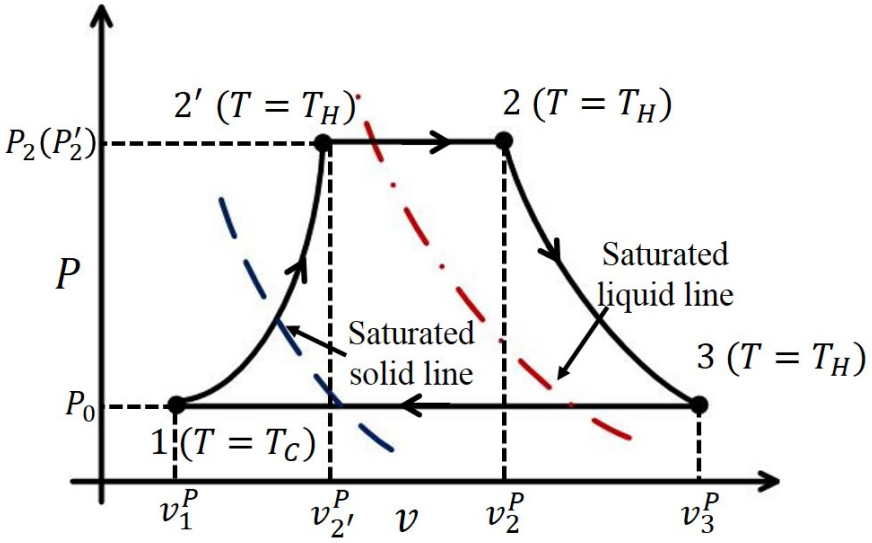

Figure 3.17: Thermodynamic cycle with an isobaric expansion process

At this point, the PCM is a mixture of solid and liquid. For pentadecane,

$$P_{2'} = \frac{T_H - \beta}{\gamma}, \tag{3.41}$$

with $\gamma = 0.2022$ K/MPa and $\beta = 283.15$ K.

The specific volume of PCM at State 2′, $v_{2'}^P$, can be calculated using Equation (3.14) with $P = P_{2'}$.

To make the melting process continue, an isobaric expansion process (State 2′ to State 2) is added, which is assumed to be isothermal (at T_H) and quasi-static. At State 2, the PCM has completely melted, and

$$P_2 = P_{2'} = \frac{T_H - \beta}{\lambda}. \tag{3.42}$$

The specific volume of PCM at State 2 (v_2^P) can be calculated using Equation (3.10) with $P = P_2$. The work done by unit mass of PCM within one thermodynamic cycle is given by

$$w = \int_{v_1^P}^{v_{2'}^P} (P - P_0)dv + \int_{v_{2'}^P}^{v_2^P} (P - P_0)dv + \int_{v_2^P}^{v_3^P} (P - P_0)dv. \tag{3.43}$$

The first term on the right hand side can be written as

$$w_{1-2'} = \int_{v_1^P}^{v_{2'}^P} (P - P_0)dv = \frac{U + W^H}{m^P}, \tag{3.44}$$

with U and W^H given by Equations (3.18) and (3.19), respectively. The second term on the right hand side of Equation (3.43) is given by

$$w_{2'-2} = \int_{v_{2'}^P}^{v_2^P} P dv = (P_2 - P_0)(v_2^P - v_{2'}^P). \tag{3.45}$$

Bibliography

[1] S. Levitus, J. I. Antonov, T. P. Boyer, O. K. Baranova, H. E. Garcia, R. A. Locarnini, A. V. Mishonov, J. Reagan, D. Seidov, E. S. Yarosh, et al., World ocean heat content and thermosteric sea level change (0–2000 m), 1955–2010, Geophysical Research Letters 39 (10).

[2] J.-P. Rebert, J.-R. Donguy, G. Eldin, K. Wyrtki, Relations between sea level, thermocline depth, heat content, and dynamic height in the tropical pacific ocean, Journal of Geophysical Research: Oceans 90 (C6) (1985) 11719–11725.

[3] A. Gorlov, Temperature differences in the ocean at low latitude and between sea and river water and air at high latitude. Electronic Encyclopedia of life support systems (EOLSS), Ocean Energy, London, UK, Electronic Encyclopedia of life support systems, Ocean Energy, London, UK, 2004.

[4] C. Körner, J. Paulsen, A world-wide study of high altitude treeline temperatures, Journal of biogeography 31 (5) (2004) 713–732.

[5] D. Klingenfeld, Special report on renewable energy sources and climate change mitigation (2011).

[6] M. Esteban, D. Leary, Current developments and future prospects of offshore wind and ocean energy, Applied Energy 90 (1) (2012) 128–136.

[7] K. Nithesh, D. Chatterjee, Numerical prediction of the performance of radial inflow turbine designed for ocean thermal energy conversion system, Applied energy 167 (2016) 1–16.

[8] A. S. Fleischer, An Introduction to Phase Change Materials, Springer International Publishing, 2015, pp. 1–5. doi:10.1007/978-3-319-20922-7_1.

[9] A. Sharma, V. V. Tyagi, C. Chen, D. Buddhi, Review on thermal energy storage with phase change materials and applications, Renewable and Sustainable energy reviews 13 (2) (2009) 318–345.

[10] Y. Lin, C. Zhu, G. Alva, G. Fang, Palmitic acid/polyvinyl butyral/expanded graphite composites as form-stable phase change materials for solar thermal energy storage, Applied Energy 228 (2018) 1801–1809.

[11] R. Hirmiz, M. Lightstone, J. Cotton, Performance enhancement of solar absorption

cooling systems using thermal energy storage with phase change materials, Applied Energy 223 (2018) 11–29.

[12] X. Kong, P. Jie, C. Yao, Y. Liu, Experimental study on thermal performance of phase change material passive and active combined using for building application in winter, Applied energy 206 (2017) 293–302.

[13] M. Alam, P. X. Zou, J. Sanjayan, S. Ramakrishnan, Energy saving performance assessment and lessons learned from the operation of an active phase change materials system in a multi-storey building in melbourne, Applied Energy 238 (2019) 1582–1595.

[14] P. N. Williams, H. A. Cousineau III, A. C. Hillman, C. P. Kramer, D. N. Legas, Package having phase change materials and method of use in transport of temperature sensitive payload, uS Patent 7,908,870 (Mar. 22 2011).

[15] E. Oró, A. De Gracia, A. Castell, M. Farid, L. Cabeza, Review on phase change materials (pcms) for cold thermal energy storage applications, Applied Energy 99 (2012) 513–533.

[16] J. A. Jones, Y. Chao, T. I. Valdez, Phase change material thermal power generator, uS Patent 7,987,674 (Aug. 2 2011).

[17] J. A. Jones, Y. Chao, T. I. Valdez, Phase change material thermal power generator, uS Patent 8,689,556 (Apr. 8 2014).

[18] Y. Chao, Autonomous underwater vehicles and sensors powered by ocean thermal energy, in: OCEANS 2016-Shanghai, IEEE, 2016, pp. 1–4.

[19] H. Kim, J.-Y. Choi, J. Park, M. Ruda, R. Prasad, Y. Chao, T. Curtin, S. Choi, Towards the optimal operation of a thermal-recharging float in the ocean, Ocean Engineering 156 (2018) 381–395.

[20] Z. Ma, Y. Wang, S. Wang, Y. Yang, Ocean thermal energy harvesting with phase change material for underwater glider, Applied Energy 178 (2016) 557–566.

[21] Y. Yang, Y. Wang, Z. Ma, S. Wang, A thermal engine for underwater glider driven by ocean thermal energy, Applied Thermal Engineering 99 (2016) 455–464.

[22] G. Wang, D. S. Ha, K. G. Wang, Harvesting environmental thermal energy using solid/liquid phase change materials, Journal of Intelligent Material Systems and Structures 29 (8) (2018) 1632–1648. doi:10.1177/1045389X17742733.

[23] C. Vélez, J. M. O. de Zárate, M. Khayet, Thermal properties of n-pentadecane, n-heptadecane and n-nonadecane in the solid/liquid phase change region, International Journal of Thermal Sciences 94 (2015) 139–146.

[24] S. D. Sharma, H. Kitano, K. Sagara, Phase change materials for low temperature solar thermal applications, Res. Rep. Fac. Eng. Mie Univ 29 (1).

[25] L. Labeyrie, J. C. Duplessy, P. Blanc, Variations in mode of formation and temperature of oceanic deep waters over the past 125,000 years, Nature 327 (6122) (1987) 477.

[26] P. Karasudhi, Foundations of solid mechanics, Vol. 3, Springer Science & Business Media, 1991.

[27] J. Dymond, R. Malhotra, The tait equation: 100 years on, International journal of thermophysics 9 (6) (1988) 941–951.

[28] W. Cutler, R. McMickle, W. Webb, R. Schiessler, Study of the compressions of several high molecular weight hydrocarbons, The Journal of Chemical Physics 29 (4) (1958) 727–740.

[29] Y.-Ð. Li, Equation of state of water and sea water, Journal of Geophysical Research 72 (10).

[30] R. Weiss, The solubility of nitrogen, oxygen and argon in water and seawater, in: Deep Sea Research and Oceanographic Abstracts, Vol. 17, Elsevier, 1970, pp. 721–735.

[31] G. S. Kell, Density, thermal expansivity, and compressibility of liquid water from 0. deg. to 150. deg.. correlations and tables for atmospheric pressure and saturation reviewed and expressed on 1968 temperature scale, Journal of Chemical and Engineering Data 20 (1) (1975) 97–105.

[32] J.-L. Daridon, H. Carrier, B. Lagourette, Pressure dependence of the thermophysical properties of n-pentadecane and n-heptadecane, International Journal of Thermophysics 23 (3) (2002) 697–708.

[33] E. C. Fitch, I. Hong, Hydraulic component design and selection, BarDyne, 1998.

[34] I. Hadjipaschalis, A. Poullikkas, V. Efthimiou, Overview of current and future energy

storage technologies for electric power applications, Renewable and sustainable energy reviews 13 (6-7) (2009) 1513–1522.

[35] T. H. Ho, K. K. Ahn, Modeling and simulation of hydrostatic transmission system with energy regeneration using hydraulic accumulator, Journal of mechanical science and technology 24 (5) (2010) 1163–1175.

[36] Parker, ACP Series Piston Accumulators (2018).
URL https://www.parker.com/literature/Accumulator%20&%20Cooler%20Division%20-%20Americas/Catalogs%20&%20Bulletins/GAD%20HY10-1630%205-2012/ACP%20Crimped%20Piston%20Accumulators.pdf

[37] E. Lawrence, G. Snyder, A study of heat sink performance in air and soil for use in a thermoelectric energy harvesting device, in: Thermoelectrics, 2002. Proceedings ICT'02. Twenty-First International Conference on, IEEE, 2002, pp. 446–449.

[38] H. A. Sodano, G. E. Simmers, R. Dereux, D. J. Inman, Recharging batteries using energy harvested from thermal gradients, Journal of Intelligent material systems and structures 18 (1) (2007) 3–10.

[39] S. Chalasani, J. M. Conrad, A survey of energy harvesting sources for embedded systems, in: Southeastcon, 2008. IEEE, IEEE, 2008, pp. 442–447.

[40] H. Hazama, Y. Masuoka, A. Suzumura, M. Matsubara, S. Tajima, R. Asahi, Cylindrical thermoelectric generator with water heating system for high solar energy conversion efficiency, Applied Energy 226 (2018) 381–388.

[41] Q. Brogan, T. O'Connor, D. S. Ha, Solar and thermal energy harvesting with a wearable jacket, in: Circuits and Systems (ISCAS), 2014 IEEE International Symposium on, IEEE, 2014, pp. 1412–1415.

[42] K. Gaurav, S. K. Pandey, Efficiency calculation of thermoelectric generator using temperature dependent material's properties, arXiv preprint arXiv:1603.01757.

[43] M. W. Rahman, K. Mahkamov, Performance analysis of multi-layer thermoelectric generators to be used in a thermoelectric generator-stirling engine hybrid system, in: ASME 2015 International Mechanical Engineering Congress and Exposition, American Society of Mechanical Engineers, 2015, pp. V06AT07A039–V06AT07A039.

[44] M. Budde, M. Busse, M. Beigl, Investigating the use of commodity dust sensors for the embedded measurement of particulate matter, in: Networked Sensing Systems (INSS), 2012 Ninth International Conference on, IEEE, 2012, pp. 1–4.

[45] P. Zappi, E. Farella, L. Benini, Tracking motion direction and distance with pyroelectric ir sensors, IEEE Sensors Journal 10 (9) (2010) 1486–1494.

[46] D. Belavic, M. Santo Zarnik, M. Mozek, S. Kocjan, M. Hrovat, J. Holc, M. Jerlah, S. Macek, Low energy consumption thick-film pressure sensors, in: Microelectronics and Packaging Conference, 2009. EMPC 2009. European, IEEE, 2009, pp. 1–6.

[47] Y.-S. Lin, D. Sylvester, D. Blaauw, An ultra low power 1v, 220nw temperature sensor for passive wireless applications, in: Custom Integrated Circuits Conference, 2008. CICC 2008. IEEE, IEEE, 2008, pp. 507–510.

Chapter 4

A Spatially Varying Robin Interface Condition for Fluid-Structure Coupled Simulations

(Submitted to *International Journal for Numerical Methods in Engineering*)

S. Cao, G. Wang, K. G. Wang

Department of Aerospace and Ocean Engineering, Virginia Polytechnic Institute and State University, Blacksburg, VA 24061, United States

Under Dr. Kevin Wang's supervision, I contributed Sections 4.1, 4.3, and 4.6 in this chapter.

Summary

We present a spatially varying Robin interface condition for solving fluid-structure interaction problems involving incompressible fluid flows and non-uniform flexible structures. Recent studies have shown that for uniform structures with constant material and geometric properties, a constant one-parameter Robin interface condition can improve the stability and accuracy of partitioned numerical solution procedures. In this work, we generalize the parameter to a spatially varying function that depends on the structure's local material and geometric properties, without varying the exact solution of the coupled fluid-structure system. We present an algorithm to implement the Robin interface condition in an embedded boundary method for coupling a projection-based incompressible viscous flow solver with a nonlinear finite element structural solver. We demonstrate the numerical effects of the spatially varying Robin interface condition using two example problems: a simplified model problem featuring a non-uniform Euler-Bernoulli beam interacting with an inviscid flow, and a generalized Turek-Hron problem featuring a non-uniform, highly flexible beam interacting with a viscous laminar flow. Both cases show that a spatially varying Robin interface condition can clearly improve numerical accuracy (by up to 2 orders of magnitude in one instance) for the same computational cost. Using the second example problem, we also demonstrate and compare two models for determining the local value of the combination function in the Robin interface condition.

Keywords

Fluid-structure interaction, Partitioned procedure, Robin interface condition, Embedded boundary method, Incompressible flow, Added mass effect

4.1 Introduction

Extensive research has been devoted to developing partitioned procedures to couple computational fluid and structural dynamics solvers for simulating fluid-structure interaction (FSI) problems [1, 2, 3, 4, 5]. A common approach is to enforce the kinematic interface condition, i.e. the continuity of velocity across the fluid-structure interface, as a Dirichlet boundary condition in the fluid solver, and to enforce the dynamic interface condition, i.e. the continuity of stress, as a Neumann boundary condition in the structural solver. This type of Dirichlet-Neumann partitioned procedures have been used to simulate a broad range of FSI problems, including problems with large structural deformation, compressible flow, shock waves, and fluid-induced instabilities and failures (e.g., [6, 7, 8, 9, 10, 11])

Nonetheless, a well-known issue of Dirichlet-Neumann partitioned procedures is that for problems involving incompressible flow and strong added mass effect (e.g., heavy fluid, thin/slender structure), the scheme becomes unstable, regardless of the spatial and temporal discretization schemes used in the fluid and structural solvers. This issue, often referred to as the numerical (or artificial) added mass effect, has been formulated using simplified

model problems [12, 13]. Specifically, Causin *et al.* [12] showed that a partitioned procedure becomes unconditionally unstable when the structure-to-fluid density ratio is below a threshold or the structure has a slender shape. Förster *et al.* [13] also investigated the stability criterion for several different temporal discretization schemes, and showed that they all become unconditionally unstable under strong added mass effect. A widely used approach to mitigate the numerical added mass effect is to perform subiterations between the fluid and structural solvers in the fashion of the Gauss-Seidel method [14, 15, 16, 17]. The drawback of this approach is obvious: it multiplies the computational cost by the number of subiterations. For example, Badia *et al.* [16] showed that to simulate a pressure wave propagating in a deformable pipe, a Dirichlet-Neumann partitioned procedure requires more than 100 subiterations per time step when the structure-to-fluid density ratio is equal to one.

Over the past decade, several research teams have investigated the use of Robin interface condition to mitigate the numerical added mass effect [18, 19, 5, 20, 21, 22, 23, 24, 25, 26, 27]. The basic idea is to substitute the kinematic interface condition by its linear combination with the dynamic interface condition. The resulting Robin-Neumann interface conditions are mathematically equivalent to the original Dirichlet-Neumann conditions, as long as the combination factor — denoted by α_f in this paper and several others — is nonzero. It has been shown that when α_f is carefully chosen, a Robin-Neumann partitioned procedure can eliminate the requirement of subiteration or reduce the number needed to achieve stability. For example, Badia *et al.* [18] proposed to design α_f based on simplified model equations (e.g., a linear piston), and have shown that for an example problem with a uniform mem-

brane, a speed-up of up to one order of magnitude can be achieved. Nobile *et al.* [19, 5, 20] and Fernandez *et al.* [21, 22] have introduced the Robin interface condition to different types of partitioned procedures and fluid/structural governing equations, and demonstrated their performance in the context of blood flow - vessel wall interaction. To solve FSI problems involving complex geometry and large deformation, Cao *et al.* [23] have developed an algorithm to enforce the Robin interface condition using an embedded boundary method. They have also shown that when choosing the value of α_f, there is a trade-off: smaller values of α_f tend to improve numerical stability, yet deteriorate the accuracy of the numerical solution. Also, Li *et al.* [24] have introduced the Robin interface condition to the overset mesh framework. Basting *et al.* [25] have implemented it in an Arbitrary Lagrangian-Eulerian (ALE) framework with a variational mesh optimization algorithm. More generally, the idea of constructing a Robin interface condition to couple different physical domains has been applied to solve other multiphysics problems, such as fluid-structure-thermal interaction [28] and multiscale fracture mechanics [29].

Notably, previous studies on the use of Robin interface condition for fluid-structure coupling have focused on uniform structures with globally constant material and geometric properties. Examples include uniform beams and thin-walled tubes with constant thickness, density and elastic moduli. Moreover, previous studies have assumed that the Robin combination factor α_f is also a constant; while at the same time, several authors have suggested that in order to mitigate the numerical added mass effect, the value of α_f must be determined based on the material and geometry of the specific problem being solved (e.g., [18, 26, 23]). In this work,

we generalize α_f to a spatially varying function, and investigate its numerical effects for FSI problems involving structures with spatially varying material properties. This study is motivated by three considerations. First, in real-world FSI problems, the structure of interest is often non-uniform, and may have complex geometry. For example, the density and the thickness of a thin-walled structure, either man-made or natural, often takes different values at different locations. Second, the previous findings mentioned above naturally suggest that if the geometric and material properties of the structure vary from one region to another, a globally constant α_f may not be optimal. It may be beneficial to generalize α_f to a variable function. Third, after generalizing α_f to a spatially varying function, the Robin-Neumann interface conditions remain mathematically equivalent to the original Dirichlet-Neumann conditions (as long as $\alpha_f \neq 0$). In other words, the generalization does not change the true solution of the coupled fluid-structure system.

More specifically, in this paper we address the following questions.

- Would a spatially varying combination function, $\alpha_f(\mathbf{X})$, outperform a constant α_f in terms of numerical accuracy and/or stability?
- If the answer to the above question is yes, how to design the function $\alpha_f(\mathbf{X})$ in order to achieve the improvement?

The remainder of this paper is organized as follows. In Section 4.2, we describe the context of this work by specifying the fluid and structural governing equations, constitutive models, and the Robin-Neumann interface conditions. Briefly speaking, we consider incompressible

laminar fluid flows interacting with thin, elastic structures. Next, in Section 4.3 we investigate the effects of spatially varying $\alpha_f(\mathbf{X})$ using a simplified model problem, in which the structure is an Euler-Bernoulli beam and the fluid domain is assumed to be fixed in time. Further, in Section 4.4, we consider a more realistic model problem, that is, a generalized Turek-Hron problem in which the flexible beam consists of multiple segments with different material properties. Using this example, we present the implementation of spatially varying $\alpha_f(\mathbf{X})$ in an embedded boundary framework, and discuss its numerical effects. In Section 4.5, we present and compare two model equations for determining the local value of the spatially varying combination function. Finally, we provide a few concluding remarks in Section 4.6.

4.2 Physical Model

4.2.1 Fluid and structural governing equations

We consider an incompressible viscous fluid flow interacting with a deformable structure, possibly with complex geometry and spatially varying material properties. The physical model couples the fluid governing equations defined in Ω_f and the structural governing equations defined in Ω_s (Figure 4.1). The fluid-structure interface, Σ, is thus defined by $\Sigma = \partial\Omega_f \cap \partial\Omega_s$. In this paper, we further assume that the fluid is Newtonian and the flow is laminar. Hence, its dynamics is governed by the following incompressible Navier-Stokes

(N-S) equations.

$$\mathscr{F}(\mathbf{U}, P) = 0 := \begin{cases} \nabla \cdot \mathbf{U} = 0 & \text{in } \Omega_f, \quad (4.1a) \\ \dfrac{\partial \mathbf{U}}{\partial t} + \mathbf{U} \cdot \nabla \mathbf{U} - \nu \Delta \mathbf{U} + \dfrac{1}{\rho_f} \nabla P = 0 & \text{in } \Omega_f, \quad (4.1b) \end{cases}$$

where t denotes time, ρ_f is the fluid density, $\mathbf{U}$ is the fluid velocity vector, P is the fluid pressure and ν the kinematic viscosity. On the outer boundary of the fluid domain, different types of boundary conditions such as no-slip wall, inlet and outlet conditions may be applied, which can be written collectively as

$$\mathscr{B}(\mathbf{U}, P) = 0 \qquad \text{on } \partial\Omega_f \setminus \Sigma. \tag{4.2}$$

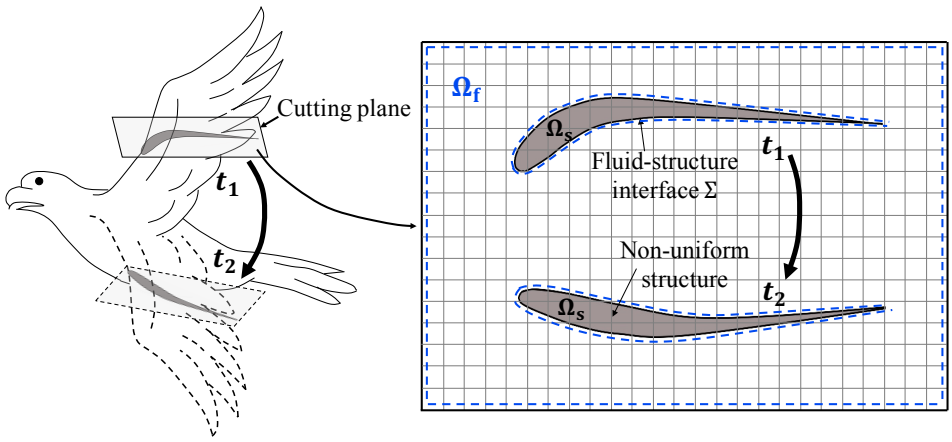

Figure 4.1: A fluid-structure interaction problem.

The structure is assumed to be elastic, and can have spatially varying material properties. To account for the possibility of large deformation, geometric nonlinearity is considered.

Therefore, the dynamic equilibrium of the structure can be formulated as

$$\mathscr{S}(\mathbf{d}(\mathbf{X},t)) = 0 := \rho_s(\mathbf{X})\frac{\partial^2 \mathbf{d}(\mathbf{X},t)}{\partial t^2} - \nabla\cdot\left(J^{-1}\mathbf{F}\mathbf{S}\mathbf{F}^T\right) - \rho_s(\mathbf{X})\,\mathbf{b}(\mathbf{X},t) = 0 \qquad \text{in}\,\Omega_s, \tag{4.3}$$

where $\mathbf{X}$ denotes the material coordinates, $\mathbf{d}$ denotes displacement, ρ_s denotes mass density, $\mathbf{S}$ is the second Piola-Kirchhoff (PK2) stress tensor, $\mathbf{F}$ is the deformation gradient, $J = \det\mathbf{F}$, and $\mathbf{b}$ denotes the body force per unit mass which is assumed to be zero here. In this work, we apply the St. Venant-Kirchhoff constitutive model, given by

$$\mathbf{S} = \lambda_s tr(\mathbf{E})\mathbf{I} + 2\mu_s\mathbf{E}, \tag{4.4}$$

where $\mathbf{I}$ is the identity matrix, and $\mathbf{E} = \frac{1}{2}(\mathbf{F}^T\mathbf{F} - \mathbf{I})$. λ_s and μ_s are the Lamé coefficients.

The fluid-structure interface is assumed to be impermeable. Thus, the fluid and structural governing equations are coupled by a kinematic interface condition, i.e. the continuity of velocity (Eq. (4.5a)), and a dynamic interface condition, i.e. the continuity of stress (Eq. (4.5b))

$$\mathbf{U} = \frac{\partial \mathbf{d}}{\partial t} \qquad \text{on}\,\Sigma, \tag{4.5a}$$

$$\sigma_f\mathbf{n} = \sigma_s\mathbf{n} \qquad \text{on}\,\Sigma, \tag{4.5b}$$

where $\mathbf{n}$ denotes the unit normal pointing towards Ω_s. σ_f denotes the fluid stress tensor, given by $\sigma_f = -P\mathbf{I} + 2\mu_f\mathbf{e}$, where $\mathbf{e}$ is the fluid strain rate tensor, and μ_f denotes the dynamic viscosity. σ_s denotes the Cauchy stress tensor of the structure, which can be related to PK2

stress by

$$\sigma_s = J^{-1}\mathbf{F}\mathbf{S}\mathbf{F}^T.$$

4.2.2 Spatially varying Robin interface condition

The Dirichlet interface condition, Eq. (4.5a), can be substituted by its linear combination with the Neumann interface condition, Eq. (4.5b), yielding a Robin interface condition. In this way, we obtain a pair of Robin-Neumann interface conditions[1], i.e.

$$\alpha_f(\mathbf{X})\frac{D\mathbf{U}}{Dt} + \sigma_f\mathbf{n} = \alpha_f(\mathbf{X})\frac{\partial^2\mathbf{d}}{\partial t^2} + \sigma_s\mathbf{n} \qquad \text{on } \Sigma, \tag{4.6a}$$

$$\sigma_f\mathbf{n} = \sigma_s\mathbf{n} \qquad \text{on } \Sigma, \tag{4.6b}$$

where $D/Dt = \partial/\partial t + \mathbf{U}\cdot\nabla$, and α_f is the linear combination parameter. As mentioned in Section 4.1, previous studies have assumed α_f to be a constant parameter. Here, we generalize it to be a spatially varying function.

Equipped with this new pair of interface conditions, the fluid and structural sub-systems can

[1]We note that in this work, as well as some previous studies (e.g., [24, 22]), the Robin condition combines the time derivative of Eq. (4.5a) with Eq. (4.5b), whereas in some other studies (e.g., [18]), the Robin condition directly combines Eq. (4.5a) with Eq. (4.5b).

be written as

$$\text{Fluid:}\begin{cases} \mathscr{F}(\mathbf{U},P)=0 & \text{in } \Omega_f & \text{(4.7a)}\\ \mathscr{B}(\mathbf{U},P)=0 & \text{on } \partial\Omega_f \setminus \Sigma & \text{(4.7b)}\\ \alpha_f(\mathbf{X})\dfrac{D\mathbf{U}}{Dt}+\sigma_f\mathbf{n}=\alpha_f(\mathbf{X})\dfrac{\partial^2\mathbf{d}}{\partial t^2}+\sigma_s\mathbf{n} & \text{on } \Sigma & \text{(4.7c)} \end{cases}$$

$$\text{Structure:}\begin{cases} \mathscr{S}(\mathbf{d})=0 & \text{in } \Omega_s & \text{(4.7d)}\\ \sigma_s\mathbf{n}=\sigma_f\mathbf{n} & \text{on } \Sigma & \text{(4.7e)} \end{cases}$$

Next, we investigate the effect of the generalized, spatially varying α_f on the stability and accuracy of partitioned solution procedures, starting with a simplified model problem.

4.3 A simple benchmark problem

4.3.1 Model setup

We consider a simplified model problem, in which a linear inviscid incompressible flow interacts with a *non-uniform* Euler-Bernoulli beam. Figure 4.2 presents a schematic drawing of the problem setup. The structure is a simply-supported Euler-Bernoulli beam, featuring lengthwise variation of density, $\rho_s(x)$ (Eq. (4.8a)). The other relevant material and geometric parameters — namely Young's modulus (E), and the width (b) and thickness (h) of the beam's cross section — are still assumed to be constant parameters. The fluid domain is a

rectangular box underneath the beam, i.e. $\Omega_f = (0, L) \times (0, H)$. Given the small deformation of the beam, we assume that Ω_f does not change in time. Also, assuming an inviscid flow with a velocity field that has zero mean (in time) and small disturbance, the middle two terms in Eq. (4.1b) can be dropped, which leads to Eq. (4.8b). The left and right boundaries are assumed to be periodic (Eq. (4.8e)), while the bottom boundary is assumed to be a wall (Eq. (4.8d)).

$$\begin{cases} EI\dfrac{\partial^4 W}{\partial x^4} + \rho_s(x) bh \dfrac{\partial^2 W}{\partial t^2} = f(x,t) & \text{in } (0,T) \times \Omega_s \quad (4.8a) \\ \rho_f \dfrac{\partial \mathbf{U}}{\partial t} + \nabla P = 0 & \text{in } (0,T) \times \Omega_f \quad (4.8b) \\ \nabla \cdot \mathbf{U} = 0 & \text{in } (0,T) \times \Omega_f \quad (4.8c) \\ \mathbf{U} \cdot \mathbf{n} = 0 & \text{on } \Gamma_B \quad (4.8d) \\ \dfrac{\partial P}{\partial \mathbf{n}}\Big|_{\Gamma_L} = \dfrac{\partial P}{\partial \mathbf{n}}\Big|_{\Gamma_R}, P\Big|_{\Gamma_L} = P\Big|_{\Gamma_R}, & \quad (4.8e) \end{cases}$$

Here, W denotes the transverse displacement of the beam. ρ_f, U, and P denote fluid density, velocity, and pressure, respectively. Γ_L, Γ_R and Γ_B denote the left, right and bottom boundaries of Ω_f, respectively. f denotes the flow-induced force on the beam.

Since the beam is simply supported on both ends, we have

$$W(0,t) = W(L,t) = 0 \qquad \text{and} \qquad \frac{\partial^2 W(0,t)}{\partial x^2} = \frac{\partial^2 W(L,t)}{\partial x^2} = 0, \qquad \forall t > 0. \tag{4.9}$$

On the fluid-structure interface (Σ), the kinematic and dynamic interface conditions are

given by

$$\mathbf{U} \cdot \mathbf{n} = \frac{\partial W}{\partial t} \qquad \text{and} \qquad f = Pb \qquad \text{on } \Sigma, \tag{4.10}$$

where $\mathbf{n}$ is the unit surface normal vector pointing towards the structure.

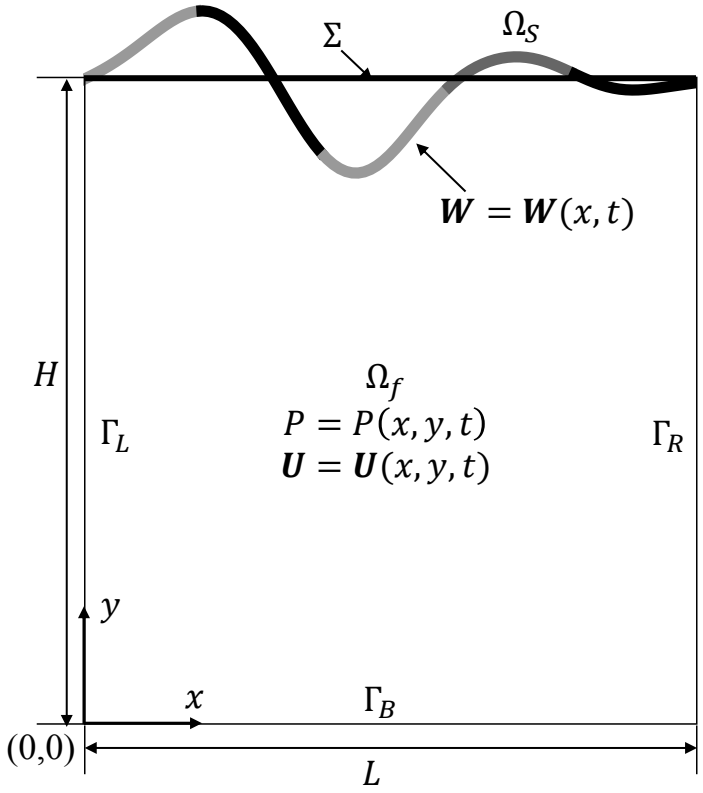

Figure 4.2: A simplified fluid-structure interaction model.

Combining Eqs. (4.8b) and (4.8c), we can eliminate the fluid velocity $\mathbf{U}$ from the system. Also, we combine the kinematic and dynamic interface conditions into a Robin interface condition, with a spatially varying combination factor $\alpha_f(x)$. After these manipulations, we obtain the following system of equations.

$$
\begin{cases}
EI\dfrac{\partial^4 W}{\partial x^4} + \rho_s(x) bh \dfrac{\partial^2 W}{\partial t^2} = f(x,t) & \text{in } (0,T)\times\Omega_s \quad (4.11a)\\
W = 0, \dfrac{\partial^2 W}{\partial x^2} = 0, & \text{at } x=0 \text{ and } x=L \quad (4.11b)\\
\nabla^2 P = 0 & \text{in } (0,T)\times\Omega_f \quad (4.11c)\\
\dfrac{\partial P}{\partial y} = 0 & \text{on } \Sigma_B \quad (4.11d)\\
\dfrac{\partial P}{\partial y}\Big|_{\Gamma_L} = \dfrac{\partial P}{\partial y}\Big|_{\Gamma_R}, P\Big|_{\Gamma_L} = P\Big|_{\Gamma_R}, & \quad (4.11e)\\
\alpha_f(x)\dfrac{\partial P}{\partial y} + Pb = -\alpha_f(x)\rho_f \dfrac{\partial^2 W}{\partial t^2} + f & \text{on } \Sigma \quad (4.11f)\\
f = Pb. & \text{on } \Sigma \quad (4.11g)
\end{cases}
$$

We consider two representative cases in which the beam's density is defined to be a smoothed step function.

- Case 1 (Figure 4.3(a)): The beam's density, $\rho_s(x)$, features two distinct values with a smooth transition in between. It is defined by

$$\rho_s(x) = \frac{\rho_{s1} + e^{\gamma x - c}\rho_{s2}}{e^{\gamma x - c} + 1}, \tag{4.12}$$

  where $\rho_{s1} = 50$ kg/m^3 and $\rho_{s2} = 4000$ kg/m^3 define the two density values, i.e. the two "steps". c and γ are two parameters that control the location and width of the transition zone. Here, $c = 100$, $\gamma = 200$ m^{-1}.

- Case 2 (Figure 4.3(b)): The beam's density, $\rho_s(x)$, features six steps. It is defined by

$$\rho_s(x) = \frac{\rho_s^{(k)} + e^{\gamma x - c^{(k)}} \rho_s^{(k+1)}}{e^{\gamma x - c^{(k)}} + 1}, \qquad \frac{(k-1)L}{5} \leq x \leq \frac{kL}{5}, \quad k = 1, 2, 3, 4, 5. \tag{4.13}$$

  In this case, $\rho_s^{(1)} = 4000\,\text{kg/m}^3$, $\rho_s^{(2)} = 2025\,\text{kg/m}^3$, $\rho_s^{(3)} = 50\,\text{kg/m}^3$, $\rho_s^{(4)} = 1366.67\,\text{kg/m}^3$, $\rho_s^{(5)} = 2683.33\ \text{kg/m}^3$, and $\rho_s^{(6)} = 4000\ \text{kg/m}^3$. Also, $c^{(1)} = 20$, $c^{(2)} = 60$, $c^{(3)} = 100$, $c^{(4)} = 140$, and $c^{(5)} = 180$, $\gamma = 200\ \text{m}^{-1}$.

In both cases, $E = 30$ GPa, $b = 0.01$ m, $h = 0.03$ m, $L = 1$ m, $H = 1$ m, and $\rho_f = 876\,\text{kg/m}^3$. The initial displacement and acceleration of the beam are set to zero. The initial value of velocity is defined by

$$v(x, 0) = v_0 \sin\big(\frac{2n\pi x}{L}\big), \tag{4.14}$$

where $v_0 = 17.28$ m/s and $n = 3$. In addition, the initial (dynamic) pressure of the fluid is set to zero.

We solve this model problem using a standard partitioned procedure. The two-dimensional Laplace equation of the fluid sub-system is solved using the five-point finite difference scheme. The structural equation is semi-discretized using a standard Galerkin finite element method, then integrated in time using the Hilbert-Hughes-Taylor α (HHT-α) method. Additional details of the numerical solution procedure are provided in Appendix A.

Remarks:

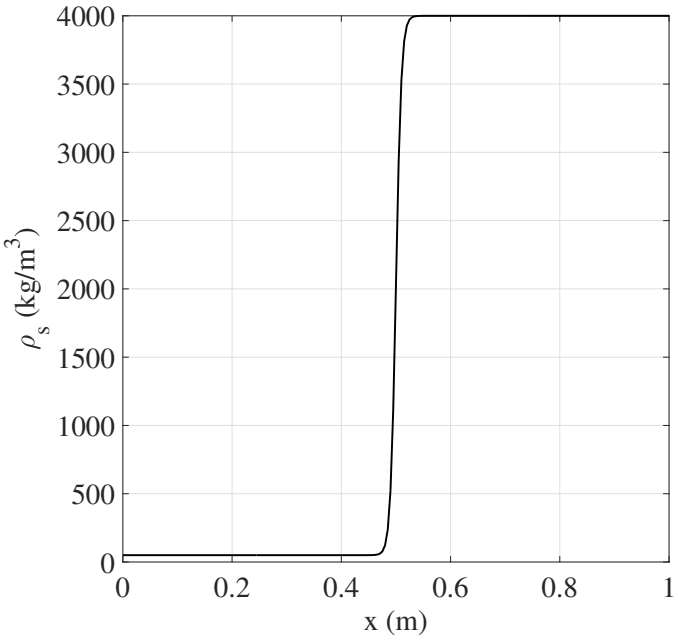

(a) Case 1

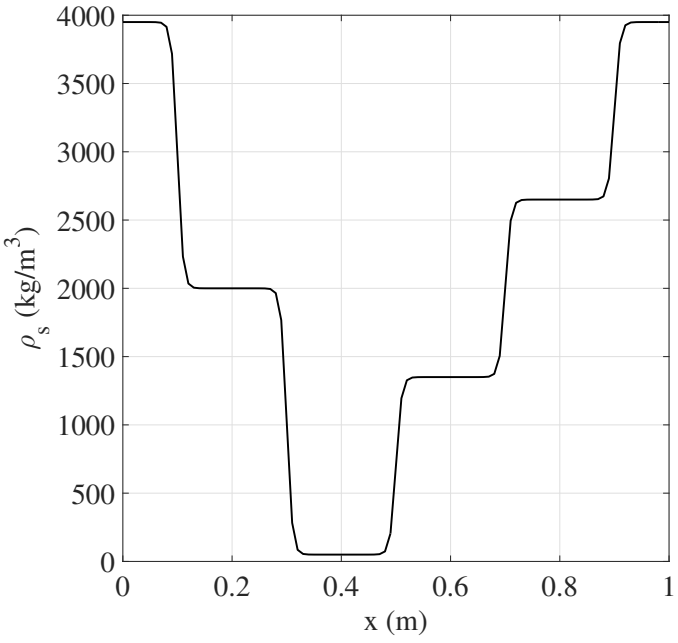

(b) Case 2

Figure 4.3: Two representative cases of non-uniform Euler-Bernoulli beam with spatially varying density.

- A simpler version of this problem, in which the beam has uniform density and α_f is a constant, has been solved both numerically and analytically (e.g., [30, 23]). Cao *et al.* [23] have derived the value of α_f that optimizes the trade-off between numerical stability and accuracy, i.e.

$$\alpha_{f,opt} = \frac{2}{\rho_f \left(\frac{1}{m_s} - \frac{1}{m_a} \right)}, \tag{4.15}$$

  where $m_s = \rho_s bh$ and $m_a = \dfrac{\rho_f b}{k \tanh(kH)}$ represent respectively the structural mass and the added mass of the fluid. The fact that $\alpha_{f,opt}$ depends on the structure's material and geometry (and how they compare with properties of the fluid flow) naturally suggests that for structures with spatially varying material properties or complex geometry, it may be advantageous to generalize α_f to a spatially varying function.

- In addition to the density of the beam, other parameters such as EI, b and h can also be generalized to spatially varying functions. We have tested some of these parameters. The results and findings obtained using a spatially varying density — to be presented in the next subsection — are found to be representative.

4.3.2 Numerical analysis: Constant α_f versus $\alpha_f(x)$

Case 1

Figures 4.4 and 4.5 show the converged numerical solution, which will be used as a reference for analyzing the effect of $\alpha_f(x)$ on accuracy. The accuracy of this reference solution has been verified by mesh convergence analysis and by comparison with the solution of a monolithic procedure, described briefly in Appendix A. Because of the spatial variation of the beam's density, the time history of mid-point deflection is not periodic (Figure 4.4), although the initial condition is a sine function. For the same reason, the magnitude of beam deflection and the fluid pressure are not symmetric with respect to the midline of the computational domain ($x = 0.5$ m).

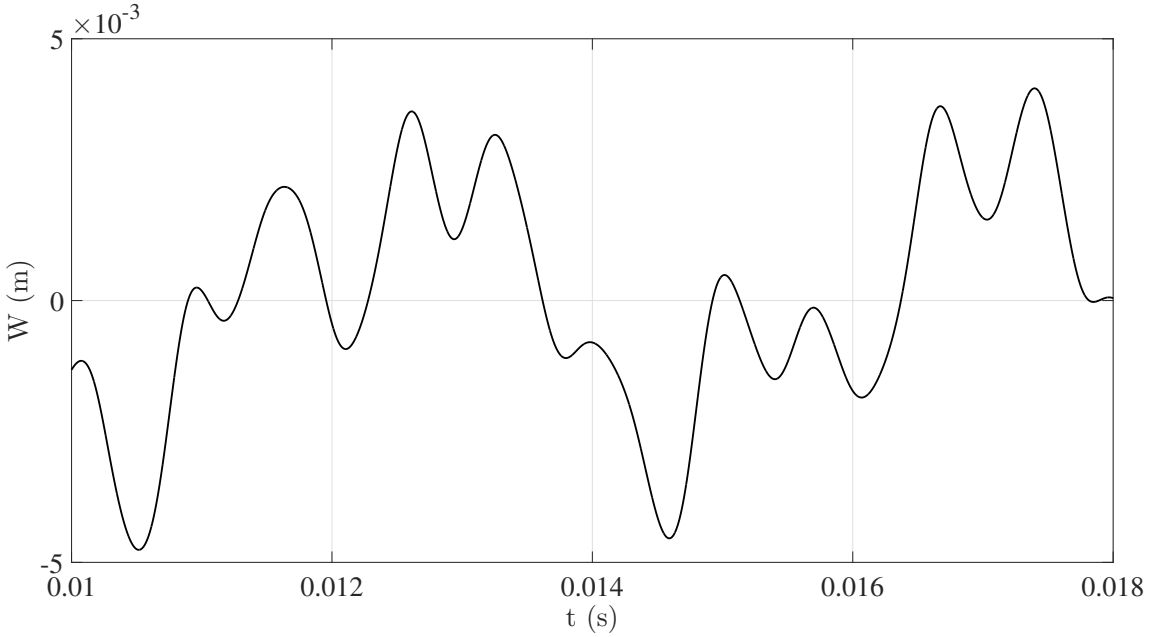

Figure 4.4: Converged solution for Case 1: Time history of beam displacement at the mid-point ($x = 0.50$ m).

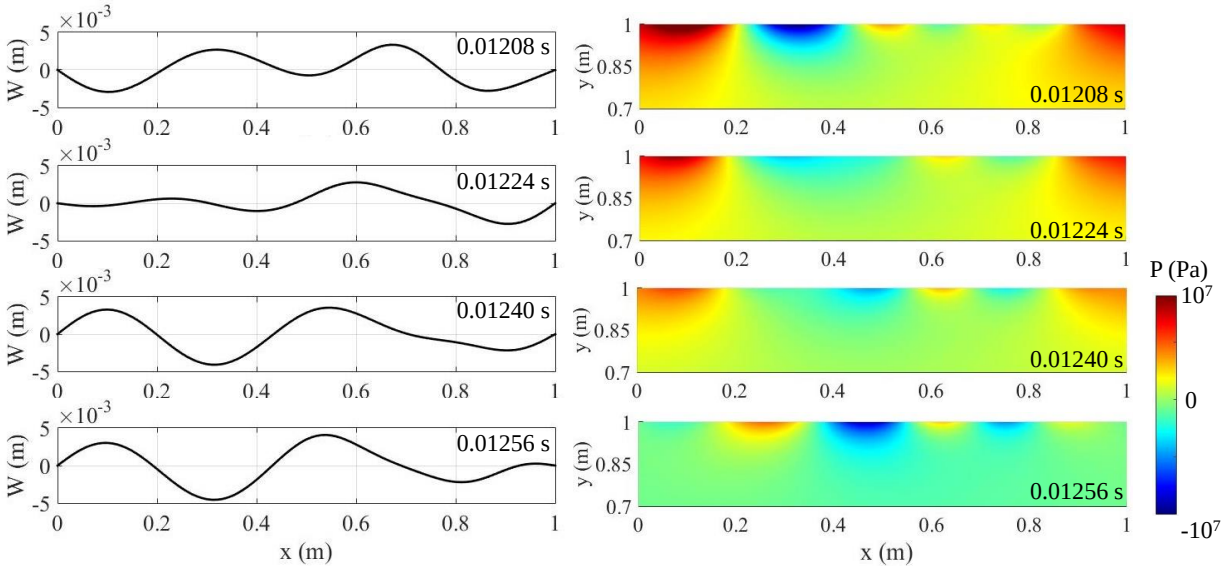

Figure 4.5: Snapshots of converged solution for Case 1. Left: Beam deflection. Right: Fluid pressure (Only the region above $y = 0.7$ m, where pressure varies significantly, is shown.)

Figure 4.6 presents the solutions obtained using the Robin-Neumann interface conditions with different constant values of α_f, in comparison with the reference solution. Both the fluid and the structural meshes have a resolution of 0.01 m. The time step size is set to be relatively large — specifically, 2×10^{-6} s — such that numerical errors can be easily observed and compared. Three different choices of α_f are presented in the figure, specifically, 3.0×10^{-5}, 4.0×10^{-5}, and 5.0×10^{-5} m^2 (for simplicity, we omit the unit m^2 for α_f in the rest of Section 4.3). Evidently, as α_f increases, the solution becomes more accurate. This is consistent with the result by Cao *et al.* [23] for a uniform beam with constant density. It is also notable that when α_f exceeds 5.0×10^{-5}, the numerical scheme becomes unconditionally unstable. For example, Figure 4.7 shows that with $\alpha_f = 5.1 \times 10^{-5}$, the solution blows up in less than 0.2 ms. Therefore, numerically we have found that for a specific pair of mesh resolution and time step size — which indicates a fixed computational cost — the most

accurate solution that can be obtained using a constant α_f is given by $\alpha_f = 5.0 \times 10^{-5}$. The observed trade-off between accuracy and stability, when selecting a constant value for α_f, is also consistent with the finding of Cao *et al.* [23].

Next, we investigate the effects of a spatially varying $\alpha_f(x)$. Given that the beam density is a (smoothed) step function, we consider a simple model for $\alpha_f(x)$ that shares the same shape. Specifically, we define

$$\alpha_f(x) = \alpha_{f0} \frac{\rho_s(x)}{\rho_{s0}}, \tag{4.16}$$

where ρ_{s0} is the minimum value of density along the beam (50 kg/m^3 in this case), and α_{f0} is a constant value estimated based on ρ_{s0}. In this case, we set $\alpha_{f0} = 5 \times 10^{-5}$.

Figure 4.8 presents the relative error of the solution obtained using the above $\alpha_f(x)$, in comparison with the most accurate solution that can be obtained using a uniform α_f, i.e. $\alpha_f = 5.0 \times 10^{-5}$. Evidently, the use of a spatially varying function $\alpha_f(x)$ leads to a reduction of numerical error in both the fluid and the structural solutions. Specifically, the maximum relative error in beam deflection decreases by 21.09%, from 0.3930 to 0.3102, while in fluid pressure it decreases by 20.09%, from 0.3300 to 0.2637.

Case 2

For reference, Figure 4.9 shows a few snapshots of the converged fluid and structural solutions, which are independent of the choice of α_f.

When a constant α_f is applied, we find again, for fixed mesh resolution and time step size,

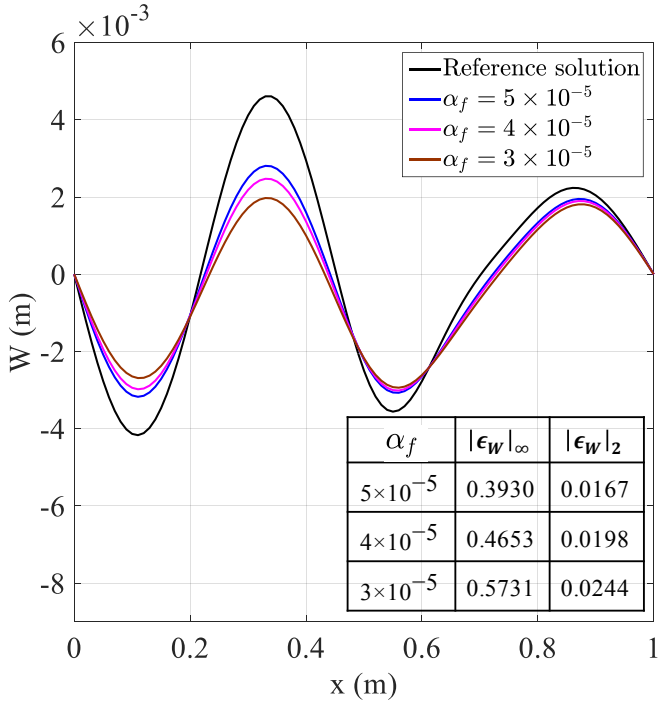

(a) Beam displacement

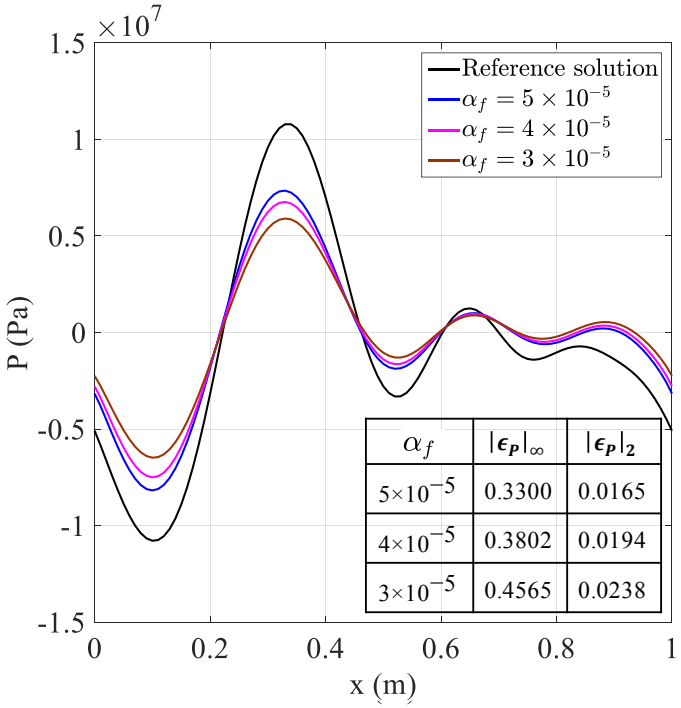

(b) Fluid pressure at the fluid-structure interface

Figure 4.6: Numerical results achieved with different values of uniform α_f at $t = 0.0015$ s, in comparison with the reference solution. ϵ_W and ϵ_P denote the relative error in beam displacement and the fluid pressure at interface, normalized using their maximum values.

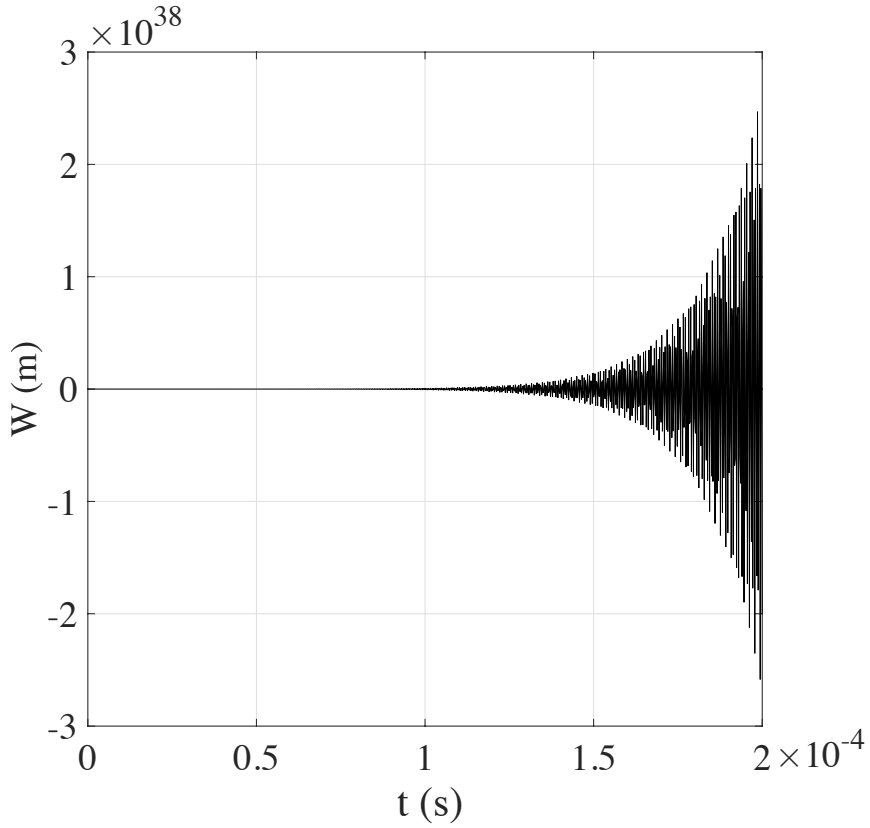

Figure 4.7: Time history of the displacement at $x = 0.50$ m with $\alpha_f = 5.1 \times 10^{-5}$.

the numerical solution becomes more accurate as the value of α_f increases, until α_f reaches a critical value, after which the solution blows up. For a 100-element structural mesh, a 100×100 fluid mesh, and a time step size of 2×10^{-6} s, this critical value is found to be 5.0×10^{-5}, same as in Case 1. This is likely because in both cases, the minimum value of the density function $\rho_s(x)$ are the same.

To investigate the effect of spatially varying $\alpha_f(x)$, we adopt the same model function introduced in Case 1, i.e. Eq. (4.16). Again, we set $\rho_{s0} = 50$ kg/m^3 and $\alpha_{f0} = 5.0 \times 10^{-5}$, based on the minimum value of the beam's density. Figure 4.10 compares the relative error in the structural and fluid solutions obtained using $\alpha_f(x)$ with the most accurate solution that can

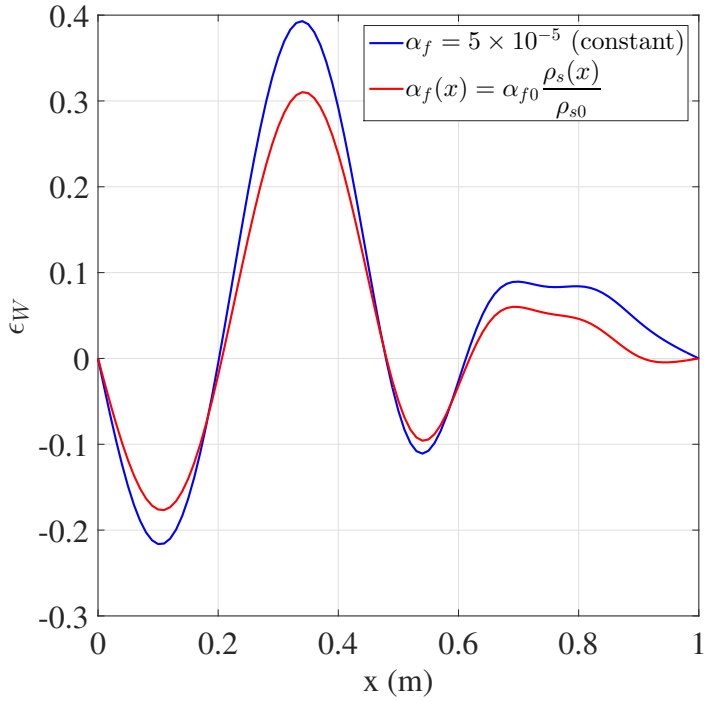

(a) Relative error in beam deflection

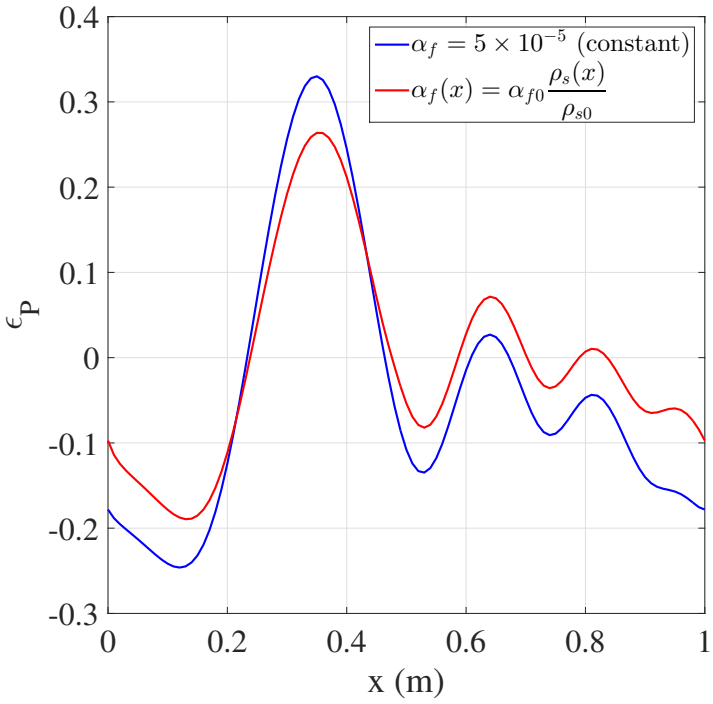

(b) Relative error in fluid pressure at the fluid-structure interface (i.e. $y = 1$ m).

Figure 4.8: Comparison of constant and a spatially varying α_f for Case 1

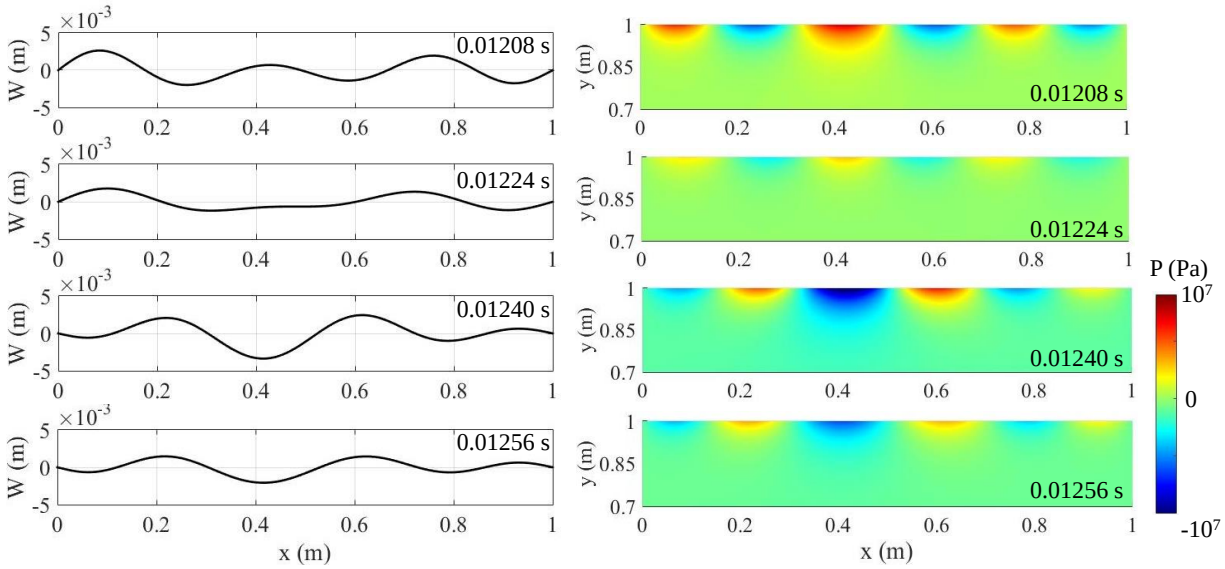

Figure 4.9: Snapshots of converged solution for Case 2. Left: Beam deflection. Right: Fluid pressure (Only the region above $y = 0.7$ m, where pressure varies significantly, is shown.)

be obtained with a constant α_f, i.e., with $\alpha_f = 5.0 \times 10^{-5}$. Comparing with Fig. 4.8 (Case 1), we find that the benefit of using a spatially varying $\alpha_f(x)$ is more significant in this case. Specifically, the maximum relatively error in beam deflection and fluid pressure is reduced by 47.44% and 42.47%, respectively. Again, we note that this error reduction is achieved by exploiting the spatial variation of the structure's material property, with virtually no increase in computational cost.

4.4 A Modified Turek-Hron Model Problem

Based on the result obtained from the simplified model problem, we now move onto solving Eqs. (4.7) and investigating the effects of spatially varying Robin interface condition in a more realistic setting.

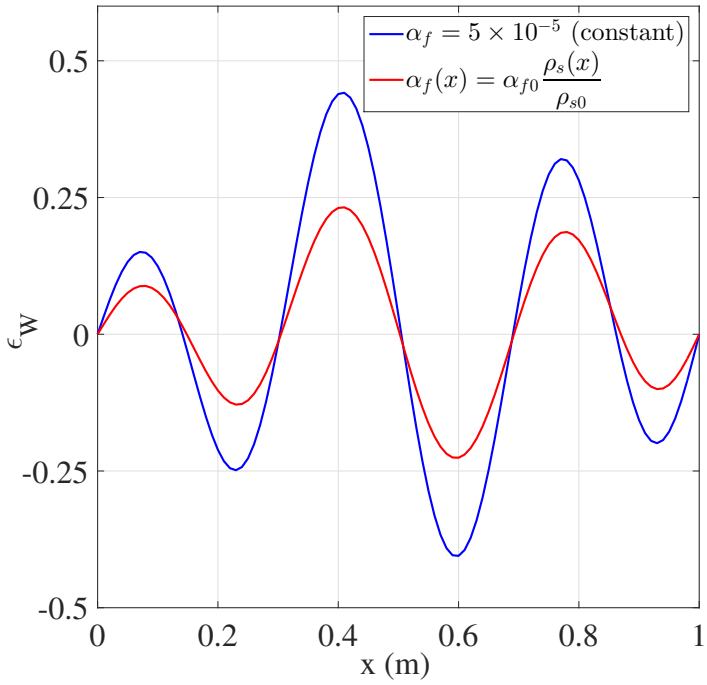

(a) Relative error in beam deflection

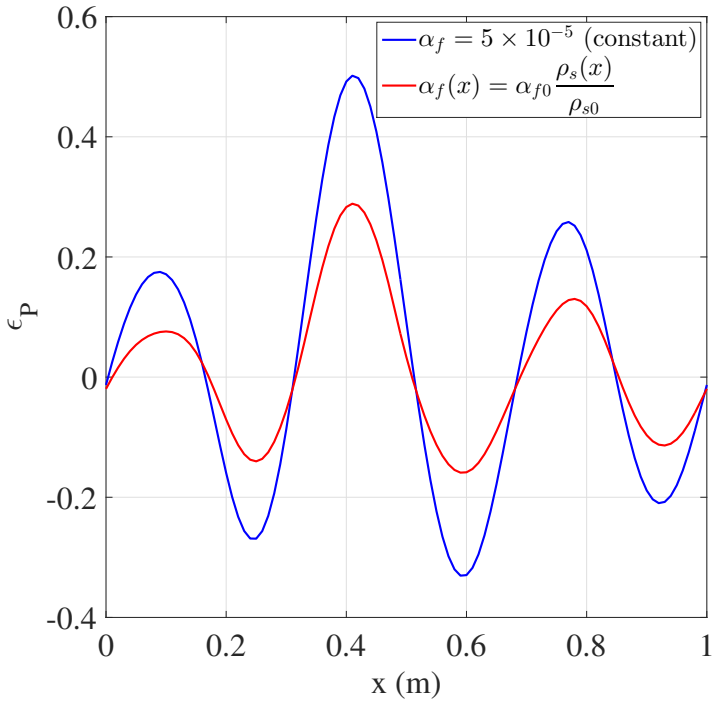

(b) Relative error in fluid pressure at the fluid-structure interface (i.e. $y = 1$ m).

Figure 4.10: Comparison of uniform and spatially varying α_f for Case 2

4.4.1 Problem description

We consider a two-dimensional laminar incompressible channel flow interacting with a non-uniform, nonlinear beam mounted on the back of a fixed cylinder. Figure 4.11 shows the geometry of the problem. It is similar to the well-known Turek-Hron benchmark problem [31], except that the attached beam considered here consists of two segments, denoted by Γ_A and Γ_B, with significantly different mass densities. Specifically, the structure-to-fluid density ratio, ρ_s/ρ_f, is 0.3 in Γ_A and 10.0 in Γ_B. This indicates that segment Γ_A is subjected to stronger added mass effect. At the inflow boundary of the fluid domain, the following velocity profile is prescribed.

$$u\left(0,y,t\right)=1.5\bar{U}\frac{y\left(H-y\right)}{\left(H/2\right)^{2}},\qquad v\left(0,y,t\right)=0, \tag{4.17}$$

where u and v denote the velocity components in the x and y directions. H is the height of the fluid domain and $\bar{U}$ is the average inflow velocity. At the channel outlet (i.e. the right boundary of the fluid domain), a "do nothing" boundary condition is applied. The no-slip boundary condition is enforced on the top and bottom walls. At the beginning of the simulation, the beam is at rest and straight as shown in the figure. Specific parameter values involved in this problem are given in Table 4.1.

	Segment Γ_A			Segment Γ_B			Fluid			
parameter	$\rho_s[kg/m^3]$	ν_s	$\mu_s[kg/ms^2]$	$\rho_s[kg/m^3]$	ν_s	$\mu_s[kg/ms^2]$	$\rho_f[kg/m^3]$	$\nu_f[m^2/s]$	$\bar{U}[m/s]$	Re
value	300	0.4	5.0×10^5	1.0×10^4	0.4	5.0×10^5	1×10^3	1×10^{-3}	1	100

Table 4.1: Parameters of the problem (ρ_s: density of the structure; ν_s: Poisson's ratio; μ_s: shear modulus; ρ_f: density of the fluid; ν_f: kinematic viscosity).

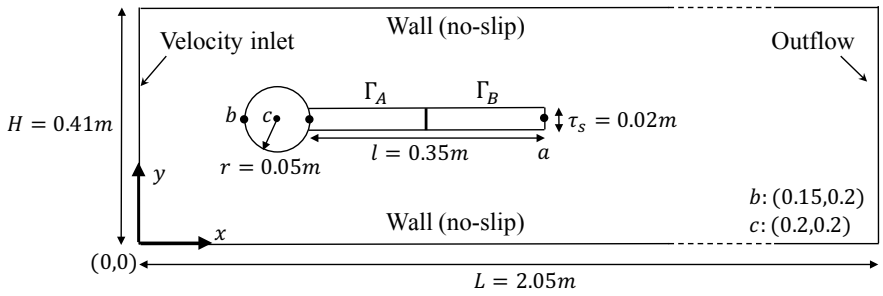

Figure 4.11: Geometry of the modified Turek-Hron benchmark problem.

4.4.2 Numerical solution approach

We employ the fluid-structure coupled computational framework recently developed by Cao *et al.* [23]. The main components of this framework include a projection-based incompressible flow solver, a finite element structural dynamics solver, and an embedded boundary method to enforce the Robin transmission condition. The computational framework has been verified using the original Turek-Hron benchmark problem with a uniform beam [31]. In this work, we extend the computational framework to enable the use of spatially varying Robin interface condition, i.e. Eq. (4.7c), and apply it to solve the modified Turek-Hron problem.

Specifically, the coupling between the fluid and structural sub-systems is based on an implicit coupling scheme which solves the two sub-systems iteratively at each time step. The following equations are solved to advance the system from time t^n to t^{n+1}.

$$\text{Fluid:}\begin{cases} \mathscr{F}(\mathbf{U}_{k+1}^{n+1}, P_{k+1}^{n+1}) = 0 & \text{in } \Omega_f \quad (4.18a) \\ \mathscr{B}(\mathbf{U}_{k+1}^{n+1}, P_{k+1}^{n+1}) = 0 & \text{on } \partial\Omega_f \setminus \Sigma \quad (4.18b) \\ \alpha_f(\mathbf{X})\dfrac{D\mathbf{U}_{k+1}^{n+1}}{Dt} + \sigma_{f,k+1}^{n+1}\mathbf{n} = \alpha_f(\mathbf{X})\left(\dfrac{\partial^2 \mathbf{d}}{\partial t^2}\right)_k^{n^\bullet} + \sigma_{s,k}^{n^\bullet}\mathbf{n} & \text{on } \Sigma \quad (4.18c) \end{cases}$$

$$\text{Structure:}\begin{cases} \mathscr{S}(\mathbf{d}_{k+1}^{n+1}) = 0 & \text{in } \Omega_s \quad (4.18d) \\ \sigma_{s,k+1}^{n+1}\mathbf{n} = \sigma_{f,k}^{n^\bullet}\mathbf{n} & \text{on } \Sigma \quad (4.18e) \end{cases}$$

where k is the index of sub-iteration. Also,

$$n^\bullet = \begin{cases} n, & \text{if } k = 0, \\ n+1, & \text{otherwise.} \end{cases}$$

At the fluid-structure interface (Σ), the latest solution information (i.e. fluid traction, structural acceleration and stress) are exchanged between the fluid and structural solvers, leading to a Gauss-Seidel type iteration.

To advance the fluid sub-system, the incompressible N-S equations are solved using a six-step, finite-difference projection method [32] on a cell-centered, collocated Cartesian grid. The spatially varying Robin interface condition, Eq. (4.18c), is enforced on the fluid-structure interface using an embedded boundary method. Specifically, we first discretize Eq. (4.18c)

in time by

$$\alpha_f(\mathbf{X})\left[\frac{\mathbf{U}_{k+1}^{n+1}-\mathbf{U}^n}{\Delta t}+(\mathbf{U}\cdot\nabla\mathbf{U})_k^{n^\bullet}\right]+\sigma_{f,k+1}^{n+1}\mathbf{n}=\alpha_f(\mathbf{X})\left(\frac{\partial^2\mathbf{d}}{\partial t^2}\right)_k^{n^\bullet}+\sigma_{s,k}^{n^\bullet}\mathbf{n}\qquad\text{on }\Sigma,\quad(4.19)$$

where the structural acceleration $\left(\partial^2\mathbf{d}/\partial t^2\right)$ is computed by the structural solver, then transferred to the fluid solver. Then, we apply an operator splitting method to split Eq. (4.19) in the same fashion as the projection method in the incompressible flow solver. This leads to

$$\begin{aligned}\mathbf{U}_{k+1}^{*,n+1} &= \mathbf{U}^n+\frac{\Delta t}{\alpha_f(\mathbf{X})}\Bigg\{-\sigma_{f,k+1}^{*,n+1}\mathbf{n}+\alpha_f(\mathbf{X})\left(\frac{\partial^2\mathbf{d}}{\partial t^2}\right)_k^{n^\bullet}\\ &+ \sigma_{s,k}^{n^\bullet}\mathbf{n}-\alpha_f(\mathbf{X})\,(\mathbf{U}\cdot\nabla\mathbf{U})_k^{n^\bullet}\Bigg\}\qquad\text{on }\Sigma,\end{aligned}\quad(4.20)$$

and

$$-\frac{\alpha_f(\mathbf{X})}{\Delta t}\left(\frac{\partial\phi}{\partial\mathbf{n}}\right)_{k+1}^{n+1}+\hat{\sigma}_{f,k+1}^{n+1}\mathbf{n}\cdot\mathbf{n}=0\qquad\text{on }\Sigma.\quad(4.21)$$

Here, $\mathbf{U}^*$ denotes the intermediate velocity, i.e. the solution of the fluid momentum equation. ϕ is an auxiliary variable in projection step. σ^* and $\hat{\sigma}$ denote the two components of the decomposed fluid stress tensor. Eq. (4.20) is enforced on the embedded interface as the boundary condition for $\mathbf{U}^*$, using a ghost-cell method [33]. Eq. (4.21) is enforced on the embedded interface as the boundary condition for Poisson's equation in projection step, using an asymmetric finite difference scheme [34, 35]. The algorithm for solving the fluid sub-system is summarized in Algorithm 1. For additional details of the projection method and the embedded Robin boundary method, we refer the reader to [23].

Algorithm 1 Algorithm for the fluid sub-system

1: Solve the momentum equation for intermediate velocity $\mathbf{U}_{k+1}^{*,n+1}$:

$$(\mathbf{I}-\eta_2\nu\mathbf{L})(\mathbf{I}-\eta_1\nu\mathbf{L})\mathbf{U}_{k+1}^{*,n+1} = (\mathbf{I}+\eta_3\nu\mathbf{L})\mathbf{U}^n - \Delta t(\mathbf{I}+\eta_4\nu\mathbf{L})\left(\mathbf{N}^{n+\frac{1}{2}} + \frac{1}{\rho_f}\mathbf{G}P^{n-\frac{1}{2}}\right) \qquad \text{in } \Omega_f, \tag{4.22}$$

$$\begin{aligned}\mathbf{U}_{k+1}^{*,n+1} &= \mathbf{U}^n + \frac{\Delta t}{\alpha_f(\mathbf{X})}\Big\{ -\sigma_{f,k+1}^{*,n+1}\mathbf{n} + \alpha_f(\mathbf{X})\left(\frac{\partial^2\mathbf{d}}{\partial t^2}\right)_k^{n^\bullet} \\ &+ \sigma_{s,k}^{n^\bullet}\mathbf{n} - \alpha_f(\mathbf{X})\left(\mathbf{U}\cdot\nabla\mathbf{U}\right)_k^{n^\bullet}\Big\} \qquad \text{on } \Sigma\end{aligned} \tag{4.23}$$

where $\mathbf{L}$ and $\mathbf{G}$ denotes the discrete Laplace operator and the discrete gradient operator, $\mathbf{I}$ is the identity operator, and $\mathbf{N}^{n+\frac{1}{2}}$ represents an approximation of the nonlinear advection term.

2: Project $\mathbf{U}_{k+1}^{*,n+1}$ onto a space that satisfies the divergence-free constraint:

$$\mathbf{L}(\phi_{k+1}^{n+1}) = \mathbf{D}\mathbf{U}_{k+1}^{*,n+1} \qquad \text{in } \Omega_f, \tag{4.24}$$

$$-\frac{\alpha_f(\mathbf{X})}{\Delta t}\left(\frac{\partial\phi}{\partial\mathbf{n}}\right)_{k+1}^{n+1} + \hat{\sigma}_{f,k+1}^{n+1}\mathbf{n}\cdot\mathbf{n} = 0 \qquad \text{on } \Sigma \tag{4.25}$$

where D denotes the discrete divergence operator.

3: Update velocity at time t^{n+1}:

$$\mathbf{U}_{k+1}^{n+1} = \mathbf{U}_{k+1}^{*,n+1} - \mathbf{G}\phi_{k+1}^{n+1}. \tag{4.26}$$

4: Solve the momentum equation again without the pressure gradient term for intermediate velocity $\widetilde{\mathbf{U}}_{k+1}^{*,n+1}$:

$$(\mathbf{I}-\eta_2\nu\mathbf{L})(\mathbf{I}-\eta_1\nu\mathbf{L})\widetilde{\mathbf{U}}_{k+1}^{*,n+1} = (\mathbf{I}+\eta_3\nu\mathbf{L})\mathbf{U}^n - \Delta t(\mathbf{I}+\eta_4\nu\mathbf{L})\mathbf{N}^{n+\frac{1}{2}} \qquad \text{in } \Omega_f, \tag{4.27}$$

$$\begin{aligned}\widetilde{\mathbf{U}}_{k+1}^{*,n+1} &= \mathbf{U}^n + \frac{\Delta t}{\alpha_f(\mathbf{X})}\{-\sigma_{f,k+1}^{*,n+1}\mathbf{n} + \alpha_f(\mathbf{X})\left(\frac{\partial^2\mathbf{d}}{\partial t^2}\right)_k^{n^\bullet} \\ &+ \sigma_{s,k}^{n^\bullet}\mathbf{n} - \alpha_f(\mathbf{X})\left(\mathbf{U}\cdot\nabla\mathbf{U}\right)_k^{n^\bullet}\} \qquad \text{on } \Sigma.\end{aligned} \tag{4.28}$$

5: Project $\widetilde{\mathbf{U}}_{k+1}^{*,n+1}$ onto a space that satisfies the divergence-free constraint:

$$\mathbf{L}(\widetilde{\phi}_{k+1}^{n+1}) = \mathbf{D}\widetilde{\mathbf{U}}_{k+1}^{*,n+1} \qquad \text{in } \Omega_f. \tag{4.29}$$

$$-\frac{\alpha_f(\mathbf{X})}{\Delta t}\left(\frac{\partial\widetilde{\phi}}{\partial\mathbf{n}}\right)_{k+1}^{n+1} + \hat{\sigma}_{f,k+1}^{n+1}\mathbf{n}\cdot\mathbf{n} = 0 \qquad \text{on } \Sigma. \tag{4.30}$$

6: Update fluid pressure at time t^{n+1}:

$$P_{k+1}^{n+\frac{1}{2}} = \frac{\rho_f}{\Delta t}(\mathbf{I}+\eta_4\nu\mathbf{L})^{-1}(\mathbf{I}-\eta_2\nu\mathbf{L})(\mathbf{I}-\eta_1\nu\mathbf{L})\widetilde{\phi}_{k+1}^{n+1} \qquad \text{in}\,\Omega_f. \tag{4.31}$$

Again, we emphasize that in Eqs. (4.20) and (4.21), α_f is a spatially varying function. Nonetheless, as long as a closed-form formulation is available, the computational overhead caused by this generalization is negligible.

For the structural sub-system, we consider a geometrically nonlinear beam in 2-D, and semi-discretize the governing equation (Eq. (4.18d)) using the continuum-based beam element [36]. Specifically, the beam is modeled as a set of adjoining quadrilateral beam elements, which relies on two assumptions: (1) the fibers are straight and inextensible; and (2) the beam is in a state of plane stress. The equation of motion for each element can be written as

$$\mathbf{M}_e\ddot{\mathbf{u}}_e^m + \mathbf{T}_e^T\mathbf{M}_e^s\dot{\mathbf{T}}_e\dot{\mathbf{u}}_e^m + \mathbf{f}^{int} = \mathbf{f}^{ext}, \tag{4.32}$$

where $\mathbf{u}_e^m$ denotes the motion of the master nodes, M_e is the mass matrix, $\mathbf{T}_e$ is the transformation matrix, $\mathbf{M}_e^s$ is the mass matrix for the quadrilaterial continuum element. $\mathbf{f}^{int}$ and $\mathbf{f}^{ext}$ denote the internal and external nodal forces, respectively. The time integration of Eq. (4.32) is done using the Newmark-β algorithm. To avoid redundancy, we refer the reader to Main [37] for additional details of the structural solver.

4.4.3 Result

Figures 4.12 and 4.13 present the converged numerical solution, specifically, the fluid vorticity, pressure and the beam 's deformation at four time instants during one period of beam vibration. It is clear that vortex shedding and vortex-induced structural vibration are the dominating features of this problem. In addition, Figure 4.14(a) presents the time history of the vertical displacement (δy) at the beam tip (i.e. point a in Figure 4.11). After the beam reaches a periodic steady state, the tip displacement varies within $\delta y \in [-0.089, 0.0915]$ m, with a period of 0.48 seconds. It is interesting to compare the solution of the current problem with that of the original Turek-Hron benchmark problem (test case FSI-2), as they only differ in the beam's density within Γ_A. Figure 4.14(b) compares the vertical displacement at the beam tip. Even though the density within Γ_A is more than one order of magnitude smaller in the current problem, the vibration frequency and amplitude only change slightly. This is because the other properties of the beam (e.g., elastic moduli, thickness) and the Reynolds number of the flow remain unchanged. And the Reynolds number is known as the key factor of the vortex shedding of the cylinder that drives the beam's vibration.

To obtain a reference solution for error analysis, a mesh convergence analysis has been conducted using Cartesian fluid meshes with resolution of 250×50, 500×100, and 1000×200. The solutions obtained using the last two meshes differ by less than 2%, in terms of the maximum vertical displacement at the beam tip. A temporal convergence analysis has also been conducted for 3.0×10^{-4} s $\leq \Delta t \leq 1.2 \times 10^{-3}$ s, using the 500×100 fluid mesh and 80 beam elements (Figure 4.15). The solutions given by $\Delta t = 6.0 \times 10^{-4}$ s and $\Delta t = 3.0 \times 10^{-4}$ s

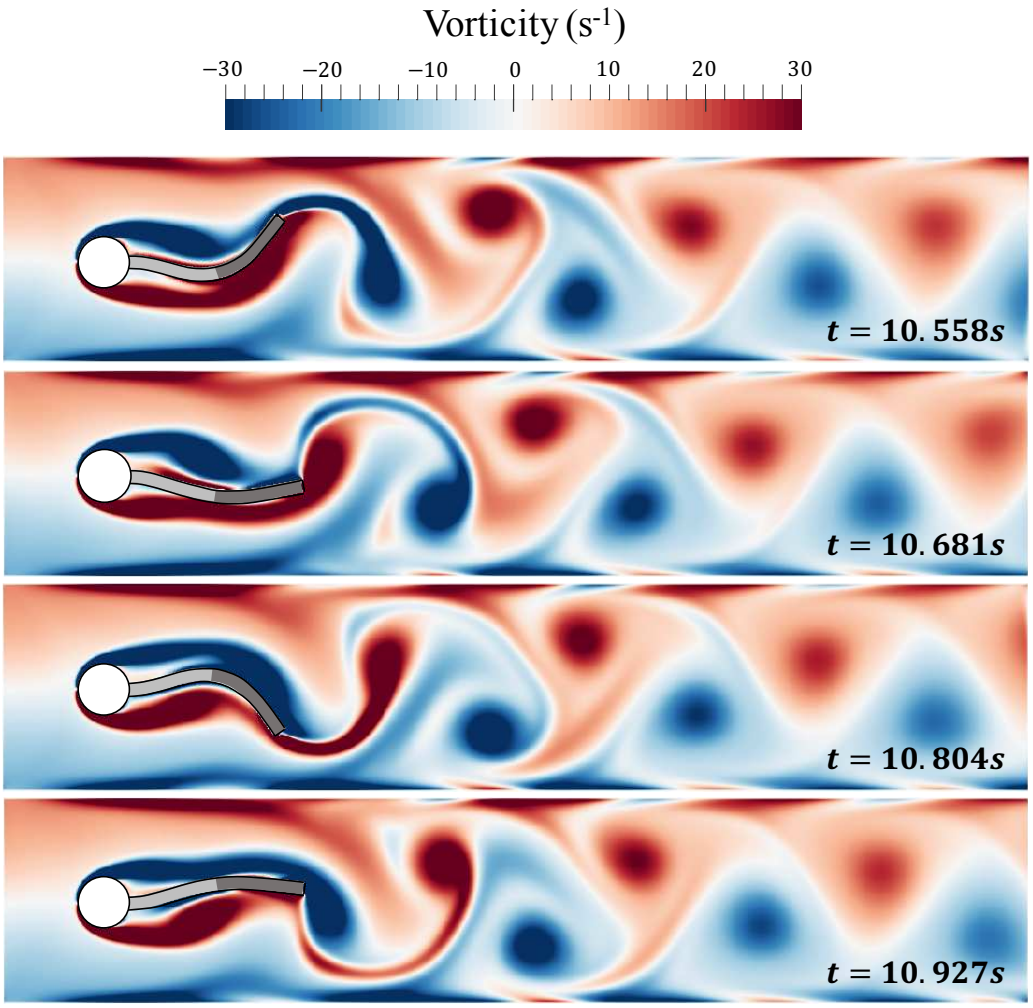

Figure 4.12: Vorticity at four time instances during one period of beam vibration.

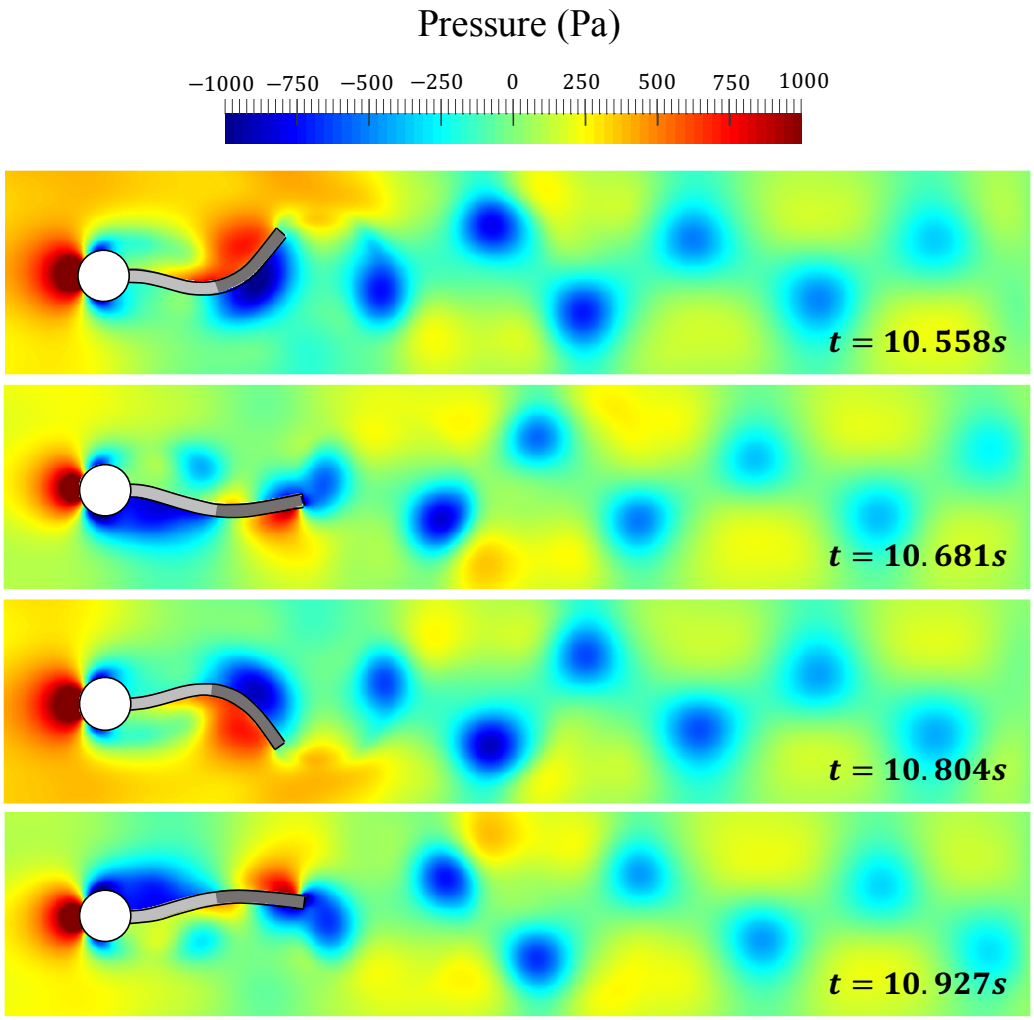

Figure 4.13: Fluid pressure at four time instances during one period of beam vibration.

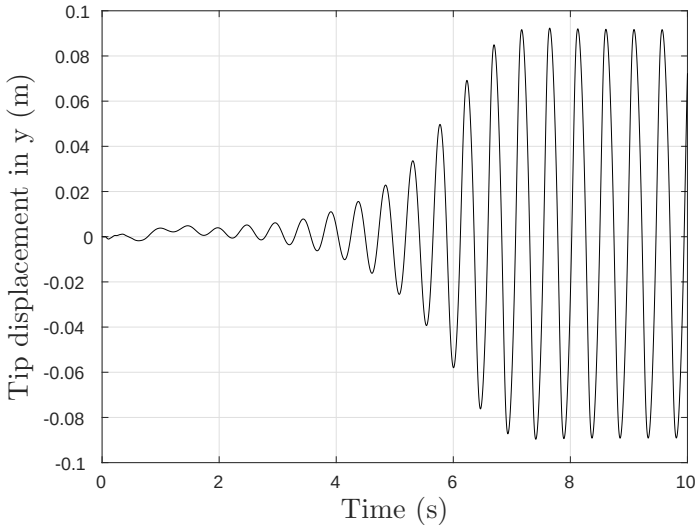

(a)

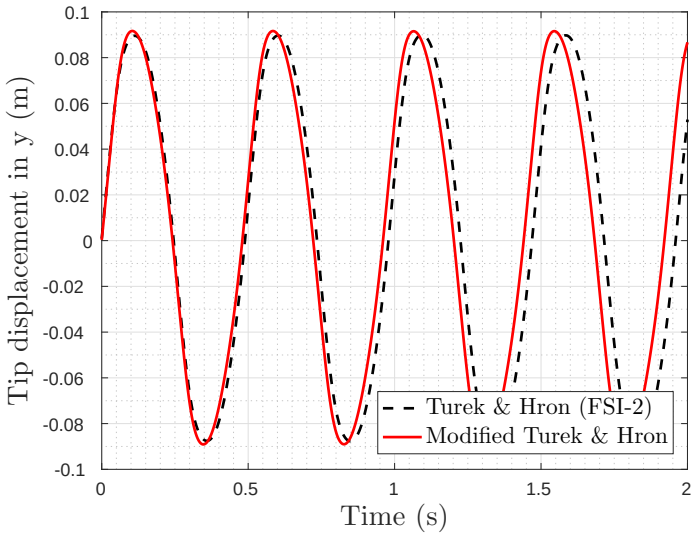

(b)

Figure 4.14: (a) Time history of beam tip displacement in y direction; (b) Comparison with the original Turek-Hron benchmark problem (test case FSI-2) [31]. In Subfigure (b), time is synchronized for the easy of comparison. The synchronized time instance 0 corresponds to 7.591 s in the original Turek-Hron problem, and 7.543 s in the modified one.

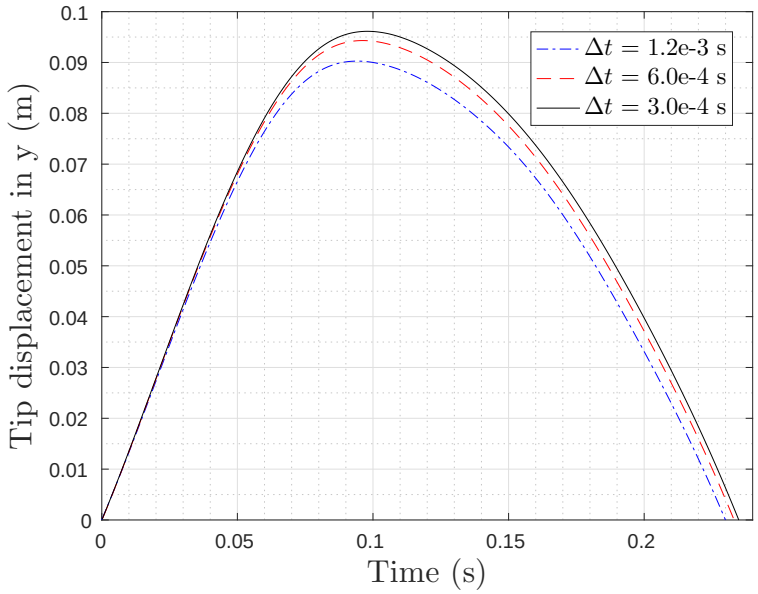

Figure 4.15: Time convergence results

differ by 2.1%, also in terms of the maximum vertical displacement at the beam tip. The results presented in Figures 4.12, 4.13, and 4.14 are computed using the 1000×200 fluid mesh, a structural mesh with 160 elements, and a time step size of 4.1×10^{-4} s. Also, six fluid-structure subiterations are performed at each time step.

4.4.4 Constant α_f versus $\alpha_f(\mathbf{X})$

We design two groups of numerical experiments. In the first group, a constant α_f is specified over the entire beam structure. In the second group, a spatially varying $\alpha_f(\mathbf{X})$ is applied. Specifically, because the beam has two segments, and the density remains constant within

each segment, we define $\alpha_f(\mathbf{X})$ to be a piecewise constant function, given by

$$\alpha_f(\mathbf{X}) = \alpha_{f,A}\mathbb{1}_{\Gamma_A} + \alpha_{f,B}\mathbb{1}_{\Gamma_B} = \begin{cases} \alpha_{f,A}, & \text{in } \Gamma_A, \\ \alpha_{f,B}, & \text{in } \Gamma_B. \end{cases} \tag{4.33}$$

All the computations are carried out using a 500×100 fluid mesh, a structural mesh with 80 elements, a time step of 8.2×10^{-4}s, and a fixed number of subiterations (3 per time step). Hence, the results from both groups are obtained with the same computational cost.

In the first group, we vary the value of α_f over a broad range, from 2.0 to 1.0×10^6 kg/m^2, and determine the threshold value for achieving numerical stability. For simplicity, we omit the unit kg/m^2 for α_f in the rest of the paper. The result shows that the solution is stable if and only if $\alpha_f \leq 4.25$. This is demonstrated by Figure 4.16 in which the fluid pressure fields obtained with $\alpha_f = 4.25$ and $\alpha_f = 4.5$ are compared. It is clear that for $\alpha_f = 4.5$ — a value slightly above the limit — the pressure field oscillates, and as time increases, both the structural and the fluid solutions blow up. Notably, the numerical instability initiates around segment Γ_A of the beam, where the structure-to-fluid density ratio is small. This indicates that if a constant α_f is used for solving FSI problems with a non-uniform structure, the largest value of α_f that can be used (to achieve better accuracy without losing stability) is likely determined by the region with strongest added mass effect.

To examine the effect of constant α_f on numerical accuracy, Figure 4.17 presents the solutions obtained with three values, $\alpha_f = 4.25$, 4.0, and 3.0, in comparison with the converged

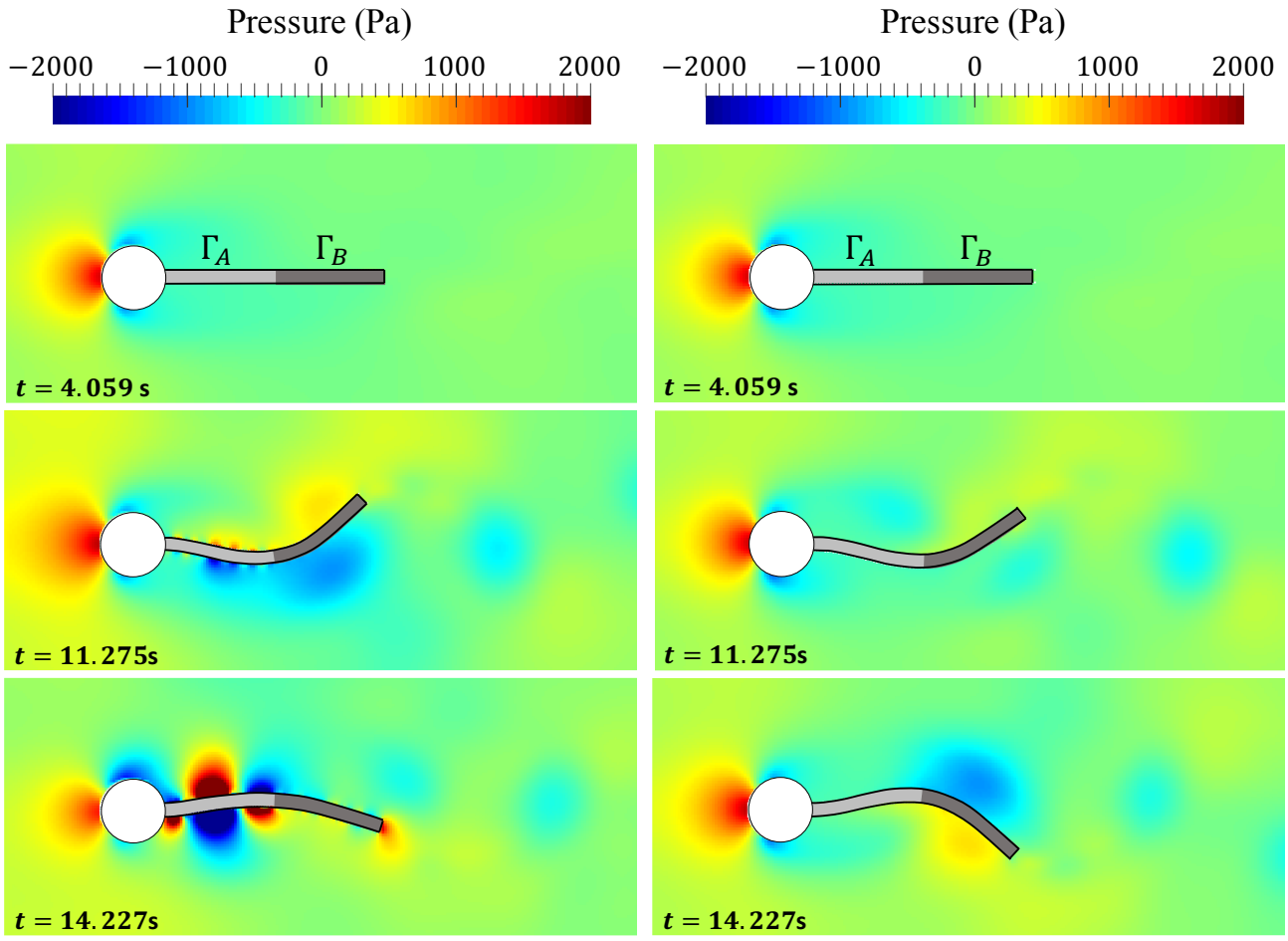

(a) $\alpha_f = 4.5$, unstable (b) $\alpha_f = 4.25$, stable

Figure 4.16: Comparison of fluid pressure obtained using two constant values of α_f across the stability limit.

reference solution. It is clear that the solution becomes less accurate as α_f is reduced. The trade-off between stability and accuracy is consistent with the finding shown by Cao *et al.* [23] for the original Turek-Hron problem. Notably, the solution obtained with $\alpha_f = 4.25$ represents the most accurate solution that can be obtained using a constant α_f for the chosen meshes, time step size, and number of subiterations (i.e. a fixed computational cost).

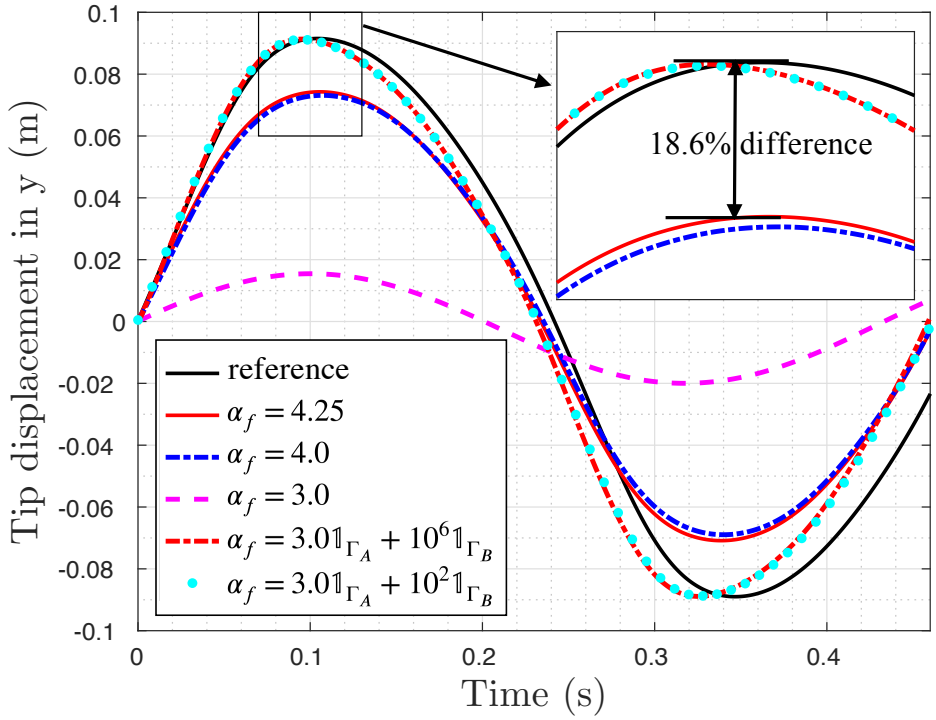

Figure 4.17: Comparison of beam tip displacement obtained with different constant values of α_f and spatially varying $\alpha_f(X)$.

In the second group of experiments, we consider the use of a piecewise constant $\alpha_f(\mathbf{X})$, with $\alpha_{f,A}$ fixed to 3.0, and $\alpha_{f,B}$ varied over a broad range, from 3.0 to 1.0×10^6. For example, Figure 4.17 shows the solutions of two trials, $\alpha_{f,B} = 100.0$ and 1.0×10^6, in comparison with the reference solution. In both cases, the predicted maximum displacement at beam

tip differs from the reference solution by less than 1%. More importantly, for both cases, the solutions are more accurate than the most accurate solution that can be obtained using a constant α_f.

Table 4.2 summarizes the relative error in maximum vertical tip displacement (ϵ_d) obtained using different constant values of α_f and spatially varying $\alpha_f(\mathbf{X})$. Comparing the trials in each group — that is, trials 1 through 4 and 5 through 8 — we find that for both constant and spatially varying α_f, numerical accuracy improves as α_f increases, until exceeding the stability limit. Comparing trial 1 with trial 7, it is evident that increasing the value of α_f in Γ_B from 3.0 to 100.0 leads to dramatic improvement in accuracy. In this case, ϵ_d decreases from 82.9% to 0.2%, by a factor of over 415. Also, comparing trial 3 with trial 7, we see that for this benchmark problem, a spatially varying α_f outperforms the optimal constant value of α_f by a factor of 93, without increasing the computational cost.

	Constant α_f				Spatially varying α_f			
Trial no.	1	2	3	4	5	6	7	8
α_f	3.0	4.0	4.25	4.5	$3.0\mathbb{1}_{\Gamma_A} + 5.0\mathbb{1}_{\Gamma_B}$	$3.0\mathbb{1}_{\Gamma_A} + 10.0\mathbb{1}_{\Gamma_B}$	$3.0\mathbb{1}_{\Gamma_A} + 10^2\mathbb{1}_{\Gamma_B}$	$3.0\mathbb{1}_{\Gamma_A} + 10^6\mathbb{1}_{\Gamma_B}$
ϵ_d	82.9%	19.7%	18.6%	N/A*	20.0%	10%	0.2%	0.2%

* unstable.

Table 4.2: Comparison of constant values of α_f with spatially varying α_f in terms of numerical error in maximum vertical tip displacement (ϵ_d).

4.5 Models for the Spatially Varying Combination Factor

4.5.1 Two models

We present two models for determining the local value of $\alpha_f(\mathbf{X})$ in the spatially varying Robin interface condition (Eq. (4.7c)). Based on the findings shown in the previous sections, we take two factors into account in the design of such models. First, the model should account for the trade-off between stability and accuracy, i.e., one would prefer to increase the value of α_f, but must avoid "falling off the cliff", that is, exceeding the stability limit. Second, a point on the structure subjected to stronger added mass effect requires a smaller value of α_f at that point to maintain stability.

Previous studies have indicated that α_f should depend on the density of the structure and — for thin-walled and slender structures — its thickness (e.g., [18, 23]). Therefore, we first build a model in which the local value of $\alpha_f(\mathbf{X})$ varies linearly with the local structural mass per unit area. Specifically, we propose

$$\text{Model 1:} \quad \alpha_f(\mathbf{X}) = \alpha_{f,0}\frac{\rho_s(\mathbf{X})h(\mathbf{X})}{\rho_{s0}h_0}, \tag{4.34}$$

where $\rho_s(\mathbf{X})$ and $h(\mathbf{X})$ denote the density of the structure and its thickness. $\rho_{s0}h_0$ is a normalization factor, defined here to be the minimum structural mass per unit area on the

structure. $\alpha_{f,0}$ is a constant that should be chosen based on $\rho_{s0}h_0$ (corresponding to the point on the structure with strongest added mass effect) in order to achieve better accuracy without losing stability.

The second model exploits the simplified model problem presented in Section 4.3, but with a uniform beam. For this problem, we have derived an optimal constant value of α_f, i.e. Eq. (4.15). Based on this finding, we propose

$$\text{Model 2:} \quad \alpha_f(\mathbf{X}) = \begin{cases} C\dfrac{M_s(\mathbf{X})M_a}{M_a - M_s(\mathbf{X})}, & \text{if } M_a > (1+\varepsilon)M_s(\mathbf{X}) \\ CM_a\varepsilon^{-1}, & \text{otherwise} \end{cases}, \tag{4.35}$$

where M_s and M_a represent the structural mass and the added mass of the fluid per unit area, respectively. C is a constant parameter that can be either estimated based on the region of the structure with strongest added mass effect, or calibrated to optimize accuracy. ε is a small numerical tolerance to avoid numeric overflow and division by zero. Equation (4.35) states that in regions where the added mass of the fluid is greater than the mass of the structure, the value of α_f reflects the ratio between these two quantities. In other regions, where the added mass effect is not significant, a large constant value of α_f is used to avoid loss of accuracy.

We define

$$M_s = \rho_s(\mathbf{X})h(\mathbf{X}) \quad \text{and} \quad M_a = \frac{\lambda\rho_f}{2\pi}, \tag{4.36}$$

where λ is the wavelength corresponding to the fundamental frequency of the structure (or

the dominant vibration frequency of the problem). Its value can be either computed through a modal analysis or estimated based on knowledge of the problem.

4.5.2 Numerical experiment

To demonstrate and compare the two models introduced above, we consider a modified Turek-Hron problem that is slightly more complex than the one introduced in Section 4.4. The flexible beam is designed to have four segments with various density values, instead of two segments as in Section 4.4. Each segment has a length of 0.0875 m. The density ρ_s is set to 300, 1,000, 2,000, and 10,000 kg/m^3 in the four segments, from left to right. Therefore, the first segment, [0, 0.0875], is the one that has the strongest added mass effect. Other parameter values involved in the problem are set to be the same as in Section 4.4, specifically, in Figure 4.11 and Table 4.1.

Figure 4.18 presents the converged solution, obtained using a 1000×200 fluid mesh, a structural mesh with 160 elements, a time step size of 2.05×10^{-4} s and 6 fluid-structure subiterations per time step. The solution is similar to the previous one in Section 4.4, with some subtle differences. For example, Figure 4.19 compares the structural displacement at three points, marked as P_1, P_2, P_3 in Figure 4.18. It shows that the two beams vibrate at slightly different frequencies, and point P_1 exhibits different modes.

Next, we perform three groups of numerical tests, using a 500×100 fluid mesh, a 80-element structural mesh, and with 3 fluid-structure subiterations per time step. The first group uses

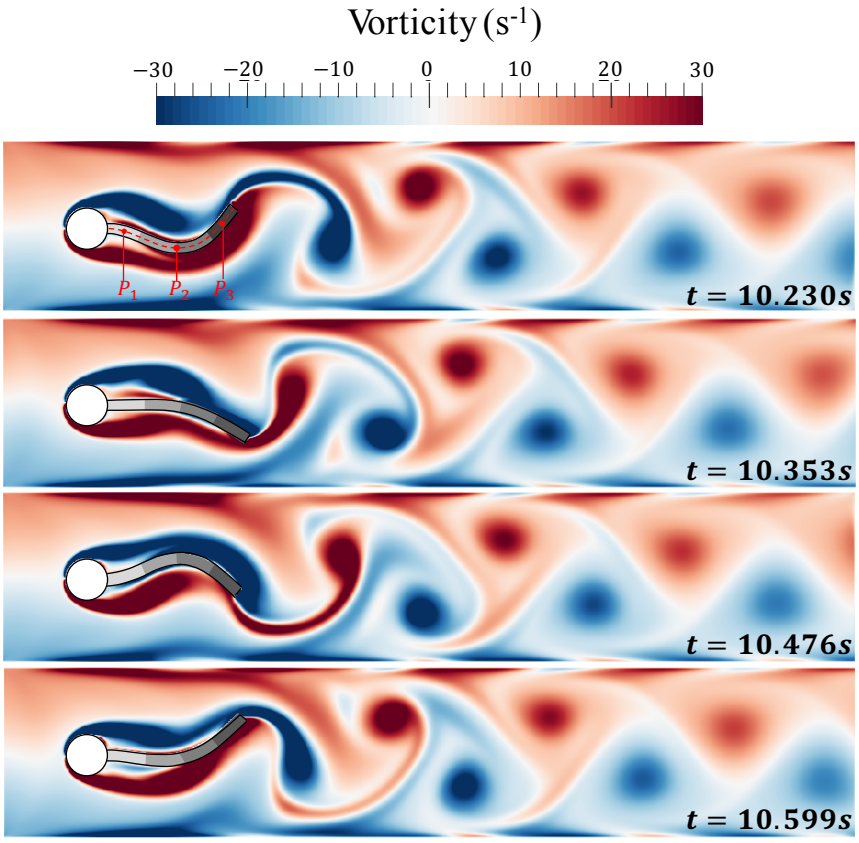

Figure 4.18: Vorticity at four time instances during one period of beam vibration.

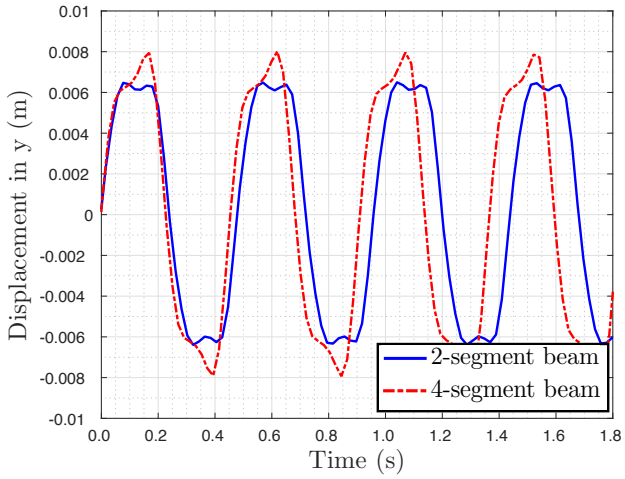

(a)

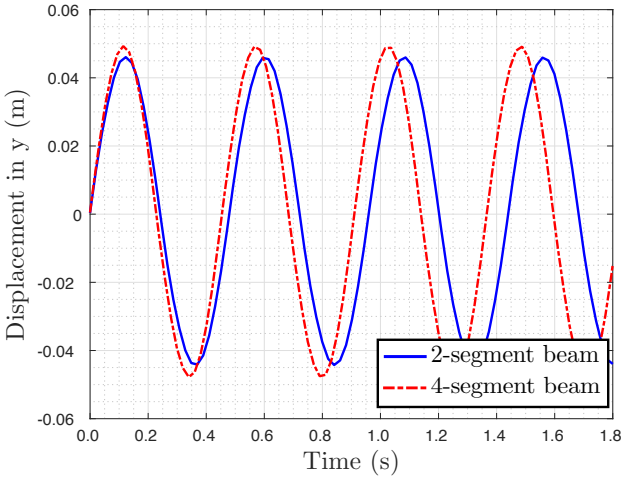

(b)

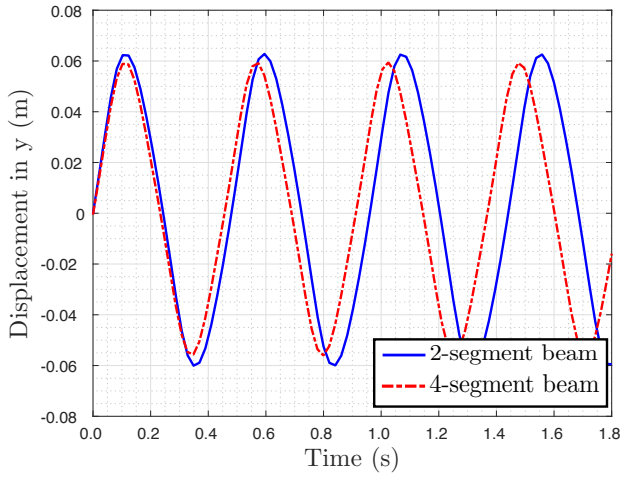

(c)

Figure 4.19: Comparison of the structural displacement in the vertical direction: (a) P_1 ($X = 0.04375$ m); (b) P_2 ($X = 0.175$ m); (c) P_3 ($X = 0.30625$ m). For each plot, time is

a constant value of α_f. We first perform a series of simulations in which the value of α_f is varied, while the time step size is set to 8.2×10^{-4} s. We found that the optimal value of α_f is 4.25, in the sense that smaller values would give less accurate solutions, while larger values would cause instability. Then, we conduct another series of simulations in which α_f is set to 4.25, while the time step size, Δt, is varied between 4.1×10^{-4} s and 1.64×10^{-3} s. The second group of tests uses a spatially varying Robin interface condition, modeled using Eq. (4.34), i.e. Model 1. We set $\alpha_{f,0}$ to ensure that along the first segment of the beam, $\alpha_f(\mathbf{X}) = 4.25$ (Figure 4.20(b)). We also vary Δt between 4.1×10^{-4} s and 1.64×10^{-3} s. The third group of tests uses a spatially varying Robin interface condition, modeled using Eq. (4.35), i.e. Model 2. Again, we ensure that along the first segment of the beam, $\alpha_f(\mathbf{X}) = 4.25$, and vary the time step size within the same interval.

In the third group of tests, we specify $\lambda = \bar{U}/f_v = D/St$, where $\bar{U}$ and f_v denote the mean inflow velocity and the frequency of vortex shedding, respectively. D is the diameter of the cylinder, and St is the Strouhal number. In other words, because in this problem the structural deformation is driven by vortex shedding, we use the frequency of vortex shedding to approximate the dominant frequency of the structure. St can be estimated based on standard measurements for flow past a fixed cylinder. For example, Williamson showed that for Reynolds number (Re) around 100, $St(Re) = 0.2175 - 5.1064/Re$ [38].

Figure 4.21 compares the vertical displacement of the beam's tip during one period of vibration. In addition, Table 4.3 presents the numerical error in the maximum vertical tip displacement. Evidently, when the time step size is fixed, both models of $\alpha_f(\mathbf{X})$ provide

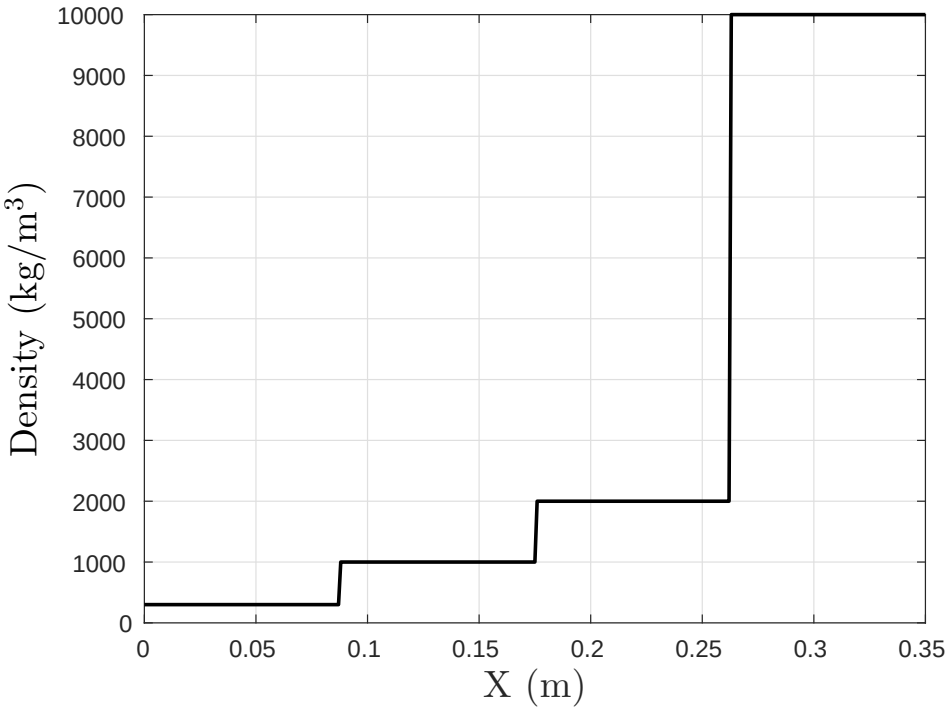

(a)

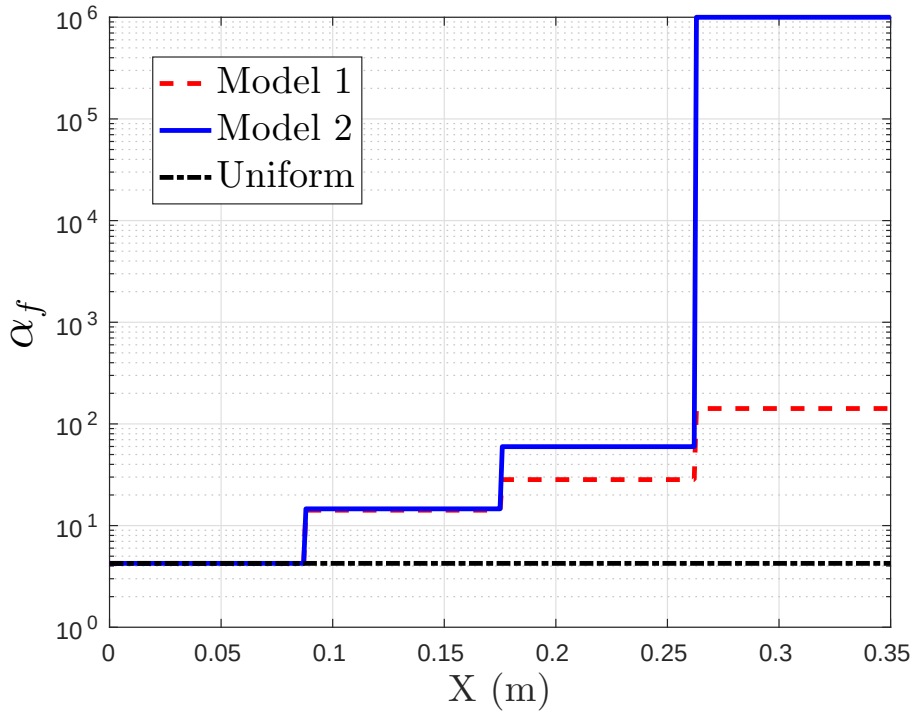

(b)

Figure 4.20: (a) Density distribution along the beam. (b) The local values of three tested α_f.

better accuracy than the optimal constant α_f. For example, in terms of maximum beam tip displacement, when $\Delta t = 8.2 \times 10^{-4}$ s, Model 1 reduces the error by a factor of 8.17 (2.4% vs. 19.6%), while Model 2 reduces the error by a factor of 7.54 (2.6% vs. 19.6%). Moreover, by varying the time step size, we can also observe the advantage of the spatially varying $\alpha_f(\mathbf{X})$. The solution obtained with either model of $\alpha_f(\mathbf{X})$ using $\Delta t = 1.23 \times 10^{-3}$ s is almost as accurate as the solution obtained with the optimal constant α_f, using $\Delta t = 4.10 \times 10^{-4}$ s.

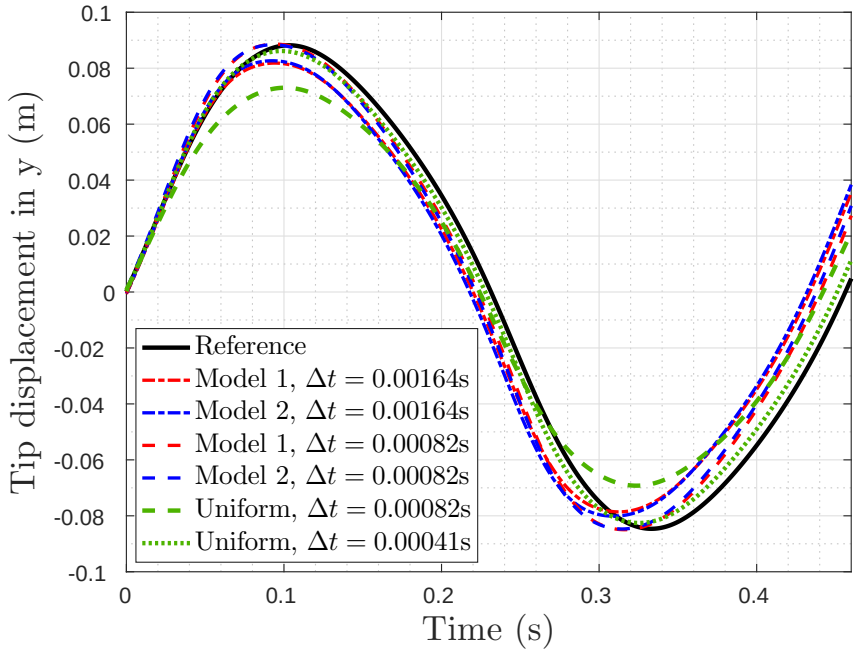

Figure 4.21: Comparison of the vertical displacement of beam tip predicted using the two modeled $\alpha_f(\mathbf{X})$ and the constant α_f. For comparison purposes, the results of one vibration cycle are presented and synchronized at the beginning of the cycle.

	Numerical error in maximum vertical tip displacement (ϵ_d)		
Time step size	Constant α_f	$\alpha_f(\mathbf{X})$ — Model 1	$\alpha_f(\mathbf{X})$ — Model 2
$\Delta t = 4.10 \times 10^{-4}$s	5.1%	1.7%	0.4%
$\Delta t = 8.20 \times 10^{-4}$s	19.6%	2.4%	2.6%
$\Delta t = 1.23 \times 10^{-3}$s	79.1%	6.2%	5.4%
$\Delta t = 1.64 \times 10^{-3}$s	96.7%	9.9%	8.9%

Table 4.3: Numerical error in the maximum vertical tip displacement obtained with the constant α_f and two modeled $\alpha_f(\mathbf{X})$.

4.6 Conclusion

We have introduced a spatially varying Robin interface condition for solving fluid-structure interaction problems involving incompressible flow, non-uniform structure, and strong added mass effect. This idea is motivated both by recent findings about applying a constant-parameter Robin interface condition for uniform structures, and by the practical need to efficiently simulate more complex structures with spatially varying material and geometric properties. To assess the spatially varying Robin interface condition, we have constructed and solved two model problems generalized from well-known benchmark problems in the literature, including a generalized Turek-Hron problem that exhibits large, fluid-induced structural deformation. For both model problems, we first find, as a baseline, the most accurate result that can be obtained using a constant Robin parameter for a fixed computational cost. Then, we show that a spatially varying Robin interface condition can clearly improve accuracy (by 93 times in one instance) with the same mesh resolution, time step size, and number of fluid-structure subiterations, i.e. the same computational cost. Moreover, we have presented the implementation of the spatially varying Robin interface condition using

an embedded boundary method to couple a projection-based incompressible flow solver with a finite element structural dynamics solver. Furthermore, we have proposed and demonstrated two closed-form formulas to determine the spatially varying function $\alpha_f(\mathbf{X})$ based on the structure's local material and geometric properties. The first one simply conforms to the spatial variation of the structure's properties, while the second one is designed by estimating the local added mass effect and exploiting a simplified model problem. In summary, this study has provided evidence that for fluid-structure interaction problems involving non-uniform structures with spatially varying material and geometric properties, it is beneficial to apply a spatially varying Robin interface condition, as compared to the constant-parameter version recently discussed in the literature. Future studies may consider exploring additional advantages of a spatially varying Robin interface condition (e.g., reducing the number of fluid-structure subiterations), developing new formulas for the spatially varying α_f, and applying the spatially varying Robin interface condition to large-scale simulations. Also, the parameter α_f in the Robin interface condition can be generalized to temporally varying or solution-adaptive functions, which may be beneficial for certain types of problems.

Acknowledgements

The authors gratefully acknowledge the support of the National Science Foundation (NSF) under awards CBET-1751487 and CBET-1706003, and the support of the Office of Naval Research (ONR) under award N00014-19-1-2102. The authors thank Dr. Alex Main for his

advice and assistance on this study.

Appendix A: Solution of a simplified model problem

We employ a partitioned procedure to separate the fluid and structural sub-systems in Eqs. (4.11), in which the fluid and the structural governing equations are solved only once per time step. Take the solution within time step t^n to t^{n+1} as an example. Given the solution at $t = t^n$ (i.e., W^n and P^n) as the initial condition, we first solve the fluid sub-system governed by a Laplace equation with a Robin boundary condition at the fluid-structure interface, i.e.

$$\begin{cases} \nabla^2 P^{n+1} = 0 & \text{in } \Omega_f, \quad (4.37a) \\ \alpha_f(x)\dfrac{\partial P^{n+1}}{\partial y} + P^{n+1}b = P^n b - \alpha_f(x)\rho_f \dfrac{\partial^2 W^n}{\partial t^2} & \text{on } \Sigma, \quad (4.37b) \\ \dfrac{\partial P^{n+1}}{\partial y}\Big|_{\Gamma_B} = 0,\ \dfrac{\partial P^{n+1}}{\partial y}\Big|_{\Gamma_L} = \dfrac{\partial P^{n+1}}{\partial y}\Big|_{\Gamma_R},\ P^{n+1}\Big|_{\Gamma_L} = P^{n+1}\Big|_{\Gamma_R}. & (4.37c) \end{cases}$$

Then, the resulting pressure load on Σ at $t = t^{n+1}$ (i.e., $P^{n+1}|_\Sigma$) is transferred to structural sub-system. Next, the structural solution is advanced from t^n to t^{n+1} by solving:

$$\begin{cases} EI\dfrac{\partial^4 W}{\partial x^4} + \rho_s bh\dfrac{\partial^2 W}{\partial t^2} = P^{n+1}|_\Sigma b \qquad \text{in } (t^n, t^{n+1}) \times \Omega_s, & (4.38a) \\ W(x, t^n) = W^n, & (4.38b) \\ \dfrac{\partial W(x,t^n)}{\partial t} = \dfrac{\partial W^n}{\partial t}, & (4.38c) \\ W\Big|_{\partial\Omega_s} = 0,\ \dfrac{\partial^2 W}{\partial x^2}\Big|_{\partial\Omega_s} = 0. & (4.38d) \end{cases}$$

More specifically, Eqs. (4.37) are solved using the conventional two-dimensional five-point finite difference scheme. Eqs. (4.38) are first semi-discretized using a standard Galerkin finite-element method. The resulting semi-discrete equation of motion can be written as

$$\mathbf{M}\ddot{W}_h + \mathbf{K}W_h = \mathbf{f}_{ext}, \tag{4.39}$$

where the subscript "h" denotes the semi-discrete solution, $\mathbf{M}$ is the mass matrix, $\mathbf{K}$ is the stiffness matrix and $\mathbf{f}_{ext}$ is the vector of external dynamic loads. Eq. (4.39) is integrated in time using the Hilber-Hughes-Taylor α (HHT-α) method, which yields a linear system for solution at $t = t^{n+1}$ (i.e., W_h^{n+1}):

$$\left[\bar{\mathbf{K}}\right] W_h^{n+1} = \left[\bar{\mathbf{F}}\right], \tag{4.40}$$

where

$$\left[\bar{\mathbf{K}}\right] = \frac{\mathbf{M}}{\beta\Delta t^2} + (1-\alpha)\mathbf{K}, \tag{4.41}$$

$$\begin{aligned}\left[\bar{\mathbf{F}}\right] &= (1-\alpha)\mathbf{f}_{ext}^{n+1} + \alpha\mathbf{f}_{ext}^{n} + \left(\frac{\mathbf{M}}{\beta\Delta t^2} - \alpha\mathbf{K}\right) W_h^n + \frac{\mathbf{M}}{\beta\Delta t}\dot{W}_h^n \\ &+ \mathbf{M}\left(\frac{1}{2\beta} - 1\right)\ddot{W}_h^n.\end{aligned} \tag{4.42}$$

Then, the acceleration and velocity of the beam at $t = t^{n+1}$ are computed by

$$\ddot{W}_h^{n+1} = \frac{1}{\beta \Delta t^2}\left[W_h^{n+1} - W_h^n - \Delta t \dot{W}_h^n\right] - \left(\frac{1}{2\beta} - 1\right)\ddot{W}_h^n, \tag{4.43}$$

$$\dot{W}_h^{n+1} = \dot{W}_h^n + \Delta t\left[(1-\gamma)\ddot{W}_h^n + \gamma \ddot{W}_h^{n+1}\right]. \tag{4.44}$$

The values of α, β and γ in the equations above are set by

$$\begin{aligned} \alpha &= 1/3, \\ \beta &= (1+\alpha)^2/4, \\ \gamma &= 1/2 + \alpha, \end{aligned}$$

which makes the scheme unconditionally stable.

Remark: We also solve the same model problem using a monolithic procedure, primarily as a way to verify the implementation of the above partitioned procedure. In the monolithic procedure, Eqs. (4.11a) and (4.11c) are discretized in space and time, yielding a system of linear equations that couples the beam displacement and fluid pressure. Specificially,

$$EI\frac{W_{i-2}^{n+1} - 4W_{i-1}^{n+1} + 6W_i^{n+1} - 4W_{i+1}^{n+1} + W_{i+2}^{n+1}}{\Delta x^4} + \rho_{s,i} bh \frac{W_i^{n+1} - 2W_i^n + W_i^{n-1}}{\Delta t^2} = P_i^{n+1} b, \tag{4.45}$$

and

$$P_{i+1,j}^{n+1} + P_{i-1,j}^{n+1} + P_{i,j+1}^{n+1} + P_{i,j-1}^{n+1} - 4P_{i,j}^{n+1} = 0. \tag{4.46}$$

Figure 4.22 compares the solutions obtained using the partitioned and monolithic procedures for Case 1. The fluid and structural meshes and the time step size are kept the same. As expected, the two numerical solutions are in close agreement.

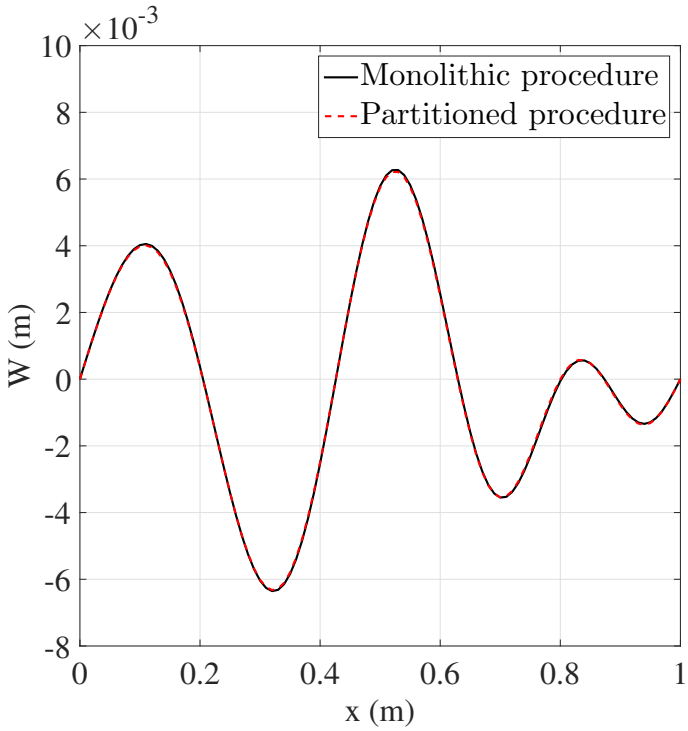

Figure 4.22: Comparison of the solutions of the partitioned and monolithic procedures for Case 1: Beam displacement at $t = 10^{-4}$ s.

Bibliography

[1] Piperno S, Farhat C, Larrouturou B. Partitioned procedures for the transient solution of coupled aroelastic problems Part I: Model problem, theory and two-dimensional application. *Computer methods in applied mechanics and engineering* 1995; 124(1-2): 79–112.

[2] Felippa CA, Park K, Farhat C. Partitioned analysis of coupled mechanical systems. *Computer methods in applied mechanics and engineering* 2001; 190(24-25): 3247–3270.

[3] Guidoboni G, Glowinski R, Cavallini N, Canic S. Stable loosely-coupled-type algorithm for fluid–structure interaction in blood flow. *Journal of Computational Physics* 2009; 228(18): 6916–6937.

[4] Farhat C, Rallu A, Wang KG, Belytschko T. Robust and provably second-order explicit–explicit and implicit–explicit staggered time-integrators for highly non-linear compressible fluid–structure interaction problems. *International Journal for Numerical Methods in Engineering* 2010; 84(1): 73–107.

[5] Nobile F, Pozzoli M, Vergara C. Time accurate partitioned algorithms for the solution of fluid–structure interaction problems in haemodynamics. *Computers & Fluids* 2013; 86: 470–482.

[6] Stein K, Benney R, Kalro V, Tezduyar TE, Leonard J, Accorsi M. Parachute fluid–structure interactions: 3-D Computation. *Computer Methods in Applied Mechanics and Engineering* 2000; 190(3-4): 373–386.

[7] Farhat C, Wang KG, Main A, et al. Dynamic implosion of underwater cylindrical shells: experiments and computations. *International Journal of Solids and Structures* 2013; 50(19): 2943–2961.

[8] Wang KG, Lea P, Farhat C. A computational framework for the simulation of high-speed multi-material fluid–structure interaction problems with dynamic fracture. *International Journal for Numerical Methods in Engineering* 2015; 104(7): 585–623.

[9] Chung H, Cao S, Philen M, Beran PS, Wang KG. CFD-CSD coupled analysis of underwater propulsion using a biomimetic fin-and-joint system. *Computers & Fluids* 2018.

[10] Cao S, Zhang Y, Liao D, Zhong P, Wang KG. Shock-Induced Damage and Dynamic Fracture in Cylindrical Bodies Submerged in Liquid. *International Journal of Solids and Structures* 2019.

[11] Liu G, Geng B, Zheng X, Xue Q, Dong H, Lauder GV. An image-guided computational approach to inversely determine in vivo material properties and model flow-structure interactions of fish fins. *Journal of Computational Physics* 2019.

[12] Causin P, Gerbeau JF, Nobile F. Added-mass effect in the design of partitioned algorithms for fluid–structure problems. *Computer methods in applied mechanics and engineering* 2005; 194(42): 4506–4527.

[13] Förster C, Wall WA, Ramm E. Artificial added mass instabilities in sequential staggered coupling of nonlinear structures and incompressible viscous flows. *Computer methods in applied mechanics and engineering* 2007; 196(7): 1278–1293.

[14] Gerbeau JF, Vidrascu M. A quasi-Newton algorithm based on a reduced model for fluid-structure interaction problems in blood flows. *ESAIM: Mathematical Modelling and Numerical Analysis* 2003; 37(4): 631–647.

[15] Deparis S, Fernández MA, Formaggia L. Acceleration of a fixed point algorithm for fluid-structure interaction using transpiration conditions. *ESAIM: Mathematical Modelling and Numerical Analysis* 2003; 37(4): 601–616.

[16] Badia S, Quaini A, Quarteroni A. Modular vs. non-modular preconditioners for fluid–structure systems with large added-mass effect. *Computer Methods in Applied Mechanics and Engineering* 2008; 197(49-50): 4216–4232.

[17] Radtke L, Larena-Avellaneda A, Debus ES, Düster A. Convergence acceleration for partitioned simulations of the fluid-structure interaction in arteries. *Computational Mechanics* 2016; 57(6): 901–920.

[18] Badia S, Nobile F, Vergara C. Fluid–structure partitioned procedures based on Robin transmission conditions. *Journal of Computational Physics* 2008; 227(14): 7027–7051.

[19] Nobile F, Vergara C. Partitioned algorithms for fluid-structure interaction problems in haemodynamics. *Milan journal of mathematics* 2012; 80(2): 443–467.

[20] Nobile F, Pozzoli M, Vergara C. Inexact accurate partitioned algorithms for fluid–structure interaction problems with finite elasticity in haemodynamics. *Journal of Computational Physics* 2014; 273: 598–617.

[21] Fernández MA, Mullaert J, Vidrascu M. Explicit Robin–Neumann schemes for the coupling of incompressible fluids with thin-walled structures. *Computer Methods in Applied Mechanics and Engineering* 2013; 267: 566–593.

[22] Fernández MA, Landajuela M, Vidrascu M. Fully decoupled time-marching schemes for incompressible fluid/thin-walled structure interaction. *Journal of Computational Physics* 2015; 297: 156–181.

[23] Cao S, Main A, Wang KG. Robin-Neumann transmission conditions for fluid-structure coupling: Embedded boundary implementation and parameter analysis. *International Journal for Numerical Methods in Engineering* 2018; 115(5): 578–603.

[24] Li L, Henshaw W, Banks J, Schwendeman D, Main A. A stable partitioned FSI algorithm for incompressible flow and deforming beams. *Journal of Computational Physics* 2016; 312: 272–306.

[25] Basting S, Quaini A, Čanić S, Glowinski R. Extended ALE Method for fluid–structure interaction problems with large structural displacements. *Journal of Computational Physics* 2017; 331: 312–336.

[26] Gerardo-Giorda L, Nobile F, Vergara C. Analysis and optimization of Robin–Robin par-

titioned procedures in fluid-structure interaction problems. *SIAM Journal on Numerical Analysis* 2010; 48(6): 2091–2116.

[27] Nie S, Cao Y, Wu Z. Numerical simulation of parafoil inflation via a Robin–Neumann transmission-based approach. *Proceedings of the Institution of Mechanical Engineers, Part G: Journal of Aerospace Engineering* 2018; 232(4): 797–810.

[28] Errera MP, Chemin S. Optimal solutions of numerical interface conditions in fluid–structure thermal analysis. *Journal of Computational Physics* 2013; 245: 431–455.

[29] Yu Y, Bargos FF, You H, Parks ML, Bittencourt ML, Karniadakis GE. A partitioned coupling framework for peridynamics and classical theory: Analysis and simulations. *Computer Methods in Applied Mechanics and Engineering* 2018; 340: 905–931.

[30] Banks JW, Henshaw WD, Schwendeman DW. An analysis of a new stable partitioned algorithm for FSI problems. Part II: Incompressible flow and structural shells. *Journal of Computational Physics* 2014; 268: 399–416.

[31] Turek S, Hron J. Proposal for numerical benchmarking of fluid-structure interaction between an elastic object and laminar incompressible flow. In: Springer. 2006 (pp. 371–385).

[32] Griffith BE, Peskin CS. On the order of accuracy of the immersed boundary method: Higher order convergence rates for sufficiently smooth problems. *Journal of Computational Physics* 2005; 208(1): 75–105.

[33] Tseng YH, Ferziger JH. A ghost-cell immersed boundary method for flow in complex geometry. *Journal of computational physics* 2003; 192(2): 593–623.

[34] Jomaa Z, Macaskill C. Numerical solution of the 2D Poisson equation on an irregular domain with Robin boundary conditions. *ANZIAM Journal* 2008; 50: 413–428.

[35] Jomaa Z, Macaskill C. The Shortley–Weller embedded finite-difference method for the 3D Poisson equation with mixed boundary conditions. *Journal of Computational Physics* 2010; 229(10): 3675–3690.

[36] Belytschko T, Liu WK, Moran B, Elkhodary K. *Nonlinear finite elements for continua and structures*. John wiley & sons . 2013.

[37] Main A. A study of fluid-structure interaction on overlapping grids with a focus on flexible beams. tech. rep., Technical Report LLNL-TR-643858, Lawrence Livermore National Laboratory; Livermore, CA (United States): 2013.

[38] Williamson CH. Oblique and parallel modes of vortex shedding in the wake of a circular cylinder at low Reynolds numbers. *Journal of Fluid Mechanics* 1989; 206: 579–627.

Chapter 5

Conclusions and Perspectives for Future Work

5.1 Summary and conclusions

This dissertation presents a combined theoretical and experimental study of PCM-based ocean thermal energy harvesting approach. The basic idea is to utilize the temperature gradient existing in the ocean thermocline to melt and freeze PCM cyclically and convert a fraction of the thermal energy absorbed in the melting process into mechanical energy or electrical energy. This study aims at demonstrating the feasibility of the proposed approach and investigating possible methods to improve the performance of specific prototypical PCM-based ocean thermal energy harvesting systems.

To assess the theoretical full potential of the PCM-based ocean thermal energy harvesting approach, a solid/liquid phase change thermodynamic model has been developed, in which the volume of PCM is assumed to be constant in the melting process (i.e, the structural system, which works as the container of PCM, is assumed to be rigid). In the model, the experimentally validated Tait EOS is used to model the thermodynamic behavior of the PCM in its liquid phase. An upperbound of thermal efficiency, which can be used a criterion to evaluate the theoretical full potential of the PCM-based approach, is derived basing on the thermodynamic model. The derived upperbound of thermal efficiency is also compared with both Carnot efficiency and that of state-of-the-art TEGs, which suggests that the PCM-based approach can give a higher thermal efficiency than Bi_2Te_3 TEGs when operating within a relatively low temperature differential (e.g., $< 100°C$).

Then a prototypical PCM-based ocean thermal energy harvesting system, which stores PCM in an elastic container, is designed, fabricated, and tested in the laboratory environment. To characterize the performance of the developed system, both the peak pressure achieved within the system and the electrical energy output are measured. To predict the performance of the developed system, a thermo-mechanical model, which couples the the aforementioned thermo-dynamic model with the Kirchoff-Love plate theory, has been developed and validated basing on the comparison with the experimental measurement. Furthermore, The validated thermo-mechanical model is used to conduct a parametric study, which shows that the performance of a PCM-based thermal energy harvesting system depends sensitively on both the structural design and properties of the PCM.

Basing on the results of the parametric study mentioned above, a new scalable and portable PCM-based ocean thermal energy harvesting system is designed, fabricated, and tested again in the laboratory environment. In this system, a cylindrical tube, which can be easily assembled with standard materials and components, is used to house the PCM. Therefore, the power output can be easily scaled by adjusting the dimensions of the tube and the amount of PCM. To analyze the performance of the system, the aforementioned thermo-mechanical model is modified to account for the change of the structural system, and validated basing on the comparison with the experimental data. However, the combined analysis of the results from both the experimental measurement and thermo-mechanical model indicates that achieving better performance, in terms of both the thermal efficiency and specific energy output, requires the structural system to be able to maintain a extremely high pressure, which is expected to be in the order of hundreds of MPa, inside the system. The structural design will be significantly constrained by the high pressure, which may also limit the applications of the PCM-based devices. To overcome this issue, the application of a hydraulic accumulator to regulate the internal pressure is proposed and investigated. Specifically, both the prototypical system and the thermo-mechanical are modified accordingly by adding a calibrated hydraulic accumulator. It is notable that, except regulating the internal pressure, the hydraulic accumulator can also improve the overall performance of the PCM-based devices. The parametric study has shown that the hydraulic accumulator leads to a one-fold increase in both the maximum possible values of thermal efficiency and specific energy output.

It is noteworthy that the fluid-structure interaction (FSI) characteristics play a crucial role

in the design of ocean-thermal-energy-powered AUVs. Therefore, as a potential method for future researches about the FSI problems related to AUVs, a spatially-varying Robin transmission condition has been developed. Specifically, a simple model problem, featuring a non-uniform Euler-Bernoulli beam interacting with an inviscid incompressible flow, is studied. The preliminary results have shown that a spatially-varying Robin transmission condition can lead to a significant improvement (up to 50% in certain cases) in accuracy, in comparison with a uniform transmission condition.

Finally, a salient feature of the PCM-based ocean thermal energy harvesting approach is that it can be easily extended and applied to provide power to other types of devices in addition to AUVs, by harvesting the thermal energy resources, which are associated with the spatial or temporal temperature difference exiting in other natural environments. For example, the air-sea temperature difference can reach around 10°C in the polar regions, from which the PCM-based approach can be adopted to extract energy. This is a very promising power source for devices deployed in polar regions, where the accessibility is significantly limited the weather conditions.

5.2 Perspectives for future work

In this dissertation, both the developed prototypical systems use an off-the-shelf hydroelectric generator to convert the mechanical energy into electrical energy, which is not optimized for the pulsatile flow driven by the pressure accumulated within the system. This is a

significant factor limiting the performance of current prototypical systems. Therefore, it is highly desirable to design and use a special nonlinear hydroelectric generator, which has a higher energy conversion efficiency under the specific pulsatile flow.

The proposed spatially varying transmission condition has only been implemented for a simplified FSI model problem and a modified Turek-Hron problem. To investigate the FSI characteristics related to the thermal-energy-powered AUVs, it is quite necessary to implement the spatially varying transmission condition in a general 3D CFD (computational fluid dynamics) — CSD (computational structural dynamics) coupled computational framework, which can be used to study the FSI characteristics of AUVs when traveling underwater.